CONTENTS

ABSTRACTS

Łukasz Czerech

Selection of Optimal Machining Strategy in the Manufacture of Elements Bounded by Curvilinear Surfaces

Increasing machining accuracy realized on CNC machine tools causes that the more frequently surfaces machined with this technique are not subject to further finishing processing and directly affects on the final quality of the product. Achieving geometric accuracy established by the constructor is the problem that modern technologists and CAD/CAM programmers have to faced with. The paper presents the influence of toolpath tolerance and machining strategy available in CAD/CAM software on the constituting process of technological surface layer for elements limited with curvilinear surfaces. The impact of the above mentioned parameters on the location and direction of geometrical deviations were also analyzed. Following article is part of research of the impact of selected technological parameters on the freeform surfaces geometric structure manufactured on CNC machines.

Artur Handke
Simpliefied Collision Detection in 4r Serial Manipulators

This paper concerns the problem of designating criteria for assessing the possibility of a collision between the elements of serial manipulators with three rotary joints allowing to flex the segments in common plane oriented by rotating the fourth connection. The issue of contactless and efficient functioning of described group of manipulators has been considered in the spatial system. Equations were derived determining the possibility of a collision between selected segments of both manipulators. Collision detection model isn't based on the information from the tactile sensors, but only on the relative position between the segments of manipulators. Based on the parameters defining the collision, the search for method of impossible collision was set on designing level, in order to minimize the time needed to examine all possible scenarios of collisions between segments. The results were included in development of methods and algorithms for planning and controlling movements of finger modules in anthropomorphic manipulator during grasping objects of indeterminate shape.

Radovan Hudák, Martin Šarik, Róbert Dadej, Jozef Živčák, Daniela Harachová
Material and Thermal Analysis of Laser Sintered Products

Thermal analysis of laser processes can be used to predict thermal stresses and consequently deformation in a completed part. Analysis of temperature is also the basic for feedback of laser processing parameters in manufacturing. The quality of laser sintered parts greatly depends on proper selection of the input processing parameters, material properties and support creation. In order to relatively big heat stress in the built part during sintering process, the thermal simulation and thermal analysis, which could help better understand and solve the issue of parts d formations is very important. Main aim of presented work is to prepare input parameters for thermal simulations by the use of RadTherm software (Thermoanalytics Inc., USA), directly during the sintering process and after the process and find out the impact of the heat stress on a final shape and size of the prototype. Subsequently, an annealing process of constructed products after DMLS could be simulated and specified.

Natália Jasminská, Tomáš Brestovič, Mária Čarnogurská
The Effect of Temperature Pyrolysis Process of Used Tires on the Quality of Output Products

Pyrolysis together with gasification and combustion create a group of so called thermic processes. Unlike the combustion it is based on thermic decomposition of organic materials without any access of oxidative media. Within the pyrolytic process, three main fractions are created: solid residue, pyrolytic gas and organic liquid product – pyrolytic oil. The presented article examines the effects of pyrolysis operational conditions (above all, temperature) on gas products, solid residues and liquid fractions.

Tadeusz Kaczorek
Singular Fractional Continuous-Time and Discrete-Time Linear Systems

New classes of singular fractional continuous-time and discrete-time linear systems are introduced. Electrical circuits are example of singular fractional continuous-time systems. Using the Caputo definition of the fractional derivative, the Weierstrass regular pencil decomposition and Laplace transformation the solution to the state equation of singular fractional linear systems is derived. It is shown that every electrical circuit is a singular fractional systems if it contains at least one mesh consisting of branches with only ideal supercondensators and voltage sources or at least one node with branches with supercoils. Using the Weierstrass regular pencil decomposition the solution to the state equation of singular fractional discrete-time linear systems is derived. The considerations are illustrated by numerical examples.

Marián Lázár, Natalia Jasminská, Marta Lengyelová
Experiment of Gasification of the Synthetically Mixed Sample of Waste in Nitrogen Atmosphere

The article presents results of gasification of the synthetically mixed sample of waste in a 30 kVA transferred DC plasma reactor with a hollow graphite electrode. The subject of the research is a sample of waste consisting of components normally found in a municipal waste. The experimental test of waste gasification with a high level of organic fraction was implemented due to the verification of previously mentioned technology application also in the area of waste disposal at the current construction design of the reactor. Gasification took place in the inert atmosphere at the average temperature of 1578 °C. The goal of the experiment was the verification of possible synthesis gas production applicable in the energetic applications and focus of the possible usage of the energetic potential of, up to now not often used, secondary energy sources such as wastes.

Zbigniew Oksiuta, Ewa Och

Corrosion Resistance of Mechanically Alloyed 14% Cr ODS Ferritic Steel

The paper presents results of the corrosion resistance of mechanically alloyed oxide dispersion strengthened 14% Cr ferritic stainless. The oxide dispersion strengthened steel was prepared by means of the powder metallurgy route that consists of mechanical alloying of a pre-alloyed argon atomized steel powder (Fe-14Cr-2W-0.3Ti) with 0.3 Y2O3 (wt%), followed by HIPping at 1150□C and annealing at 850□C for 1 h. The density of ODS ferritic steel after consolidation was about 99.0% of theoretical alloy density. The potentiodynamic corrosion tests were performed for 1h and 24 h of material exposure in a physiological saline solution. For comparison the 316 LV austenitic stainless steel was also examined. The obtained results revealed that both materials were in a passive stage, however the lower current corrosion density was measured for 316 LV steel. On the contrary, the austenitic stainless steel exhibited unstable chemical processes at the passive region. On the surface of both materials localized pitting corrosion was observed with different morphology of the cavities. A broken oxide scale with poor adhesion to the ferritic steel matrix with large number of density of localized corrosion attack was observed on the surface of the ODS steel.

Łukasz Sajewski

Positive Minimal Realization of Continuous-Discrete Linear Systems with All-Pole and All-Zero Transfer Function

The positive and minimal realization problem for continuous-discrete linear single-input and single-outputs (SISO) systems is formulated. Two special case of the continuous-discrete systems are given. Method based on the state variable diagram for finding a positive and minimal realization of a given proper transfer function is proposed. Sufficient conditions for the existence of a positive minimal realization of a given proper transfer function of all-pole and all-zero systems are established. Two procedures for computation of a positive minimal realization are proposed and illustrated by a numerical examples.

Heorhiy Sulym, Iaroslav Pasternak, Serhiy Kutsyk, Wojciech Grodzki

Doubly Periodic Sets of Thin Branched Inclusions in the Elastic Medium: Stress Concentration and Effective Properties

This paper considers the doubly periodic problem of elasticity for anisotropic solids containing regular sets of thin branched in-clusions. A coupling principle for continua of different dimension is utilized for modeling of thin inhomogeneities and the boundary element technique is adopted for numerical solution of the problem. The branches of the inclusion can interact both inside the representative volume element and at the interface of neighbor representative elements. A particular example of the elastic medium reinforced by a doubly periodic set of I-beams is considered. Stress intensity and stress concentration inside and outside thin inclusions are determined. The dependence of the effective mechanical properties of the reinforced composite material on the volume fraction of the filament and its rigidity is obtained.

Ihor Turchyn, Olga Turchyn

Transient Plane Waves in Multilayered Half-Space

Considered the dynamic problem of the theory of elasticity for multilayered half-space. Boundary surface of inhomogeneous half-space loaded with normal load, and the boundaries of separation layers are in conditions of ideal mechanical contact. The formulation involves non-classical separation of equations of motion using two functions with a particular mechanical meaning volumetric expansion and function of acceleration of the shift. In terms of these functions obtained two wave equation, written boundary conditions and the conditions of ideal mechanical contact of layers. Using the Laguerre and Fourier integral transformations was obtained the solution of the formulated problem. The results of the calculation of the stress-strain state in the half-space with a coating for a local impact loading are presented.

Grzegorz Żywica

The Dynamic Performance Analysis of the Foil Bearing Struture

Foil bearings are a variety of slide bearings in which an additional set of foils is applied between journal and bush, in order to improve the selected static and dynamic properties. Engineers and researchers from all over the world investigate bearings of this type since many years – both from numerical as well as experimental point of view. Due to the complexity of construction, the reliable simulation models are all the time being searched for. This paper discusses the important stages of elaboration of the structural supporting layer numerical model of the foil bearing as well as results of verification tests. The main goal of the conducted study was assessment of reliability of the elaborated numerical model, in scope of dynamic properties. In the near future it will be used for elaboration of the numerical model of the entire foil bearing, which will take into account also phenomena in fluid-film layer. Those models will be used together to describe bearing system in operation.

SELECTION OF OPTIMAL MACHINING STRATEGY
IN THE MANUFACTURE OF ELEMENTS BOUNDED BY CURVILINEAR SURFACES

Łukasz CZERECH*

*Department of Production Engineering, Faculty of Mechanical Engineering, Bialystok University of Technology,
ul. Wiejska 45C, 15-351 Bialystok, Poland

lukaszczerech@wp.pl

Abstract: Increasing machining accuracy realized on CNC machine tools causes that the more frequently surfaces machined with this technique are not subject to further finishing processing and directly affects on the final quality of the product. Achieving geometric accuracy established by the constructor is the problem that modern technologists and CAD/CAM programmers have to faced with. The paper presents the influence of toolpath tolerance and machining strategy available in CAD/CAM software on the constituting process of technological surface layer for elements limited with curvilinear surfaces. The impact of the above mentioned parameters on the location and direction of geometrical deviations were also analyzed. Following article is part of research of the impact of selected technological parameters on the freeform surfaces geometric structure manufactured on CNC machines.

Keywords: Toolpath Tolerance, Machining Strategy, Geometric Deviations, CAD, CAM

1. INTRODUCTION

Most of the objects used in industry consist of simple geometries such as plains, cylinders, tapers, spheres, torus or their mutual combinations. Nowadays industry forces us to use more complex shapes and this in turn determines us to use freeform surfaces. The largest share of these elements can be seen in the aerospace, optic, plastic, automotive or biomedical industry. The most recognizable objects in industries mentioned above are the turbine blades for jet engines, aircraft fuselages, car body parts, ship propellers, asymmetric lenses, housings of household appliances, etc. To produce this kind of elements sometimes it is necessary to perform specialized tools (press tools, molds, punching dies, etc.) that should be characterized by high manufacturing precision in order to use them to produce parts of high quality and repeatability.

Measurement of geometrical deviations of freeform surfaces can be achieved in two ways: direct and indirect comparison with the reference models (Saviol et al., 2007). The first one is based on a comparison of the resulting object with the real one. Indirect comparison relies on the measurement of machined surface done by such machinery and equipment such as: coordinate measuring machines with contact or noncontact heads, radars or laser interferometers, fotogrameters, optical systems based on projection and reflection of measuring fringes, profilometers (measurements with a resolution of nanometres), confocal microscopes, atomic forces microscopes, X-ray tomographs and ultrasonic measurements. As a result, we get the digital equivalent of the analyzed element, carrying the deviations arising during the manufacturing process, and then comparing the resulting cloud of control points with the nominal virtual geometric model.

The geometric accuracy of manufactured parts limited by curvilinear surfaces is a very important issue. Machine components, which curvilinear surfaces cooperate with each other and so must

be in the 7, 8 accuracy class, are more common. What is more, from some of these parts also high technological quality of the surface layer to reduce the costs associated with additional technological operations is required. Machining of these objects is achieved primarily through numerically controlled machine tools, and their geometric accuracy is closely related to parameters such as: technical condition of machines (machine error) (Czerech and Kaczyński, 2013), condition and type of the machining tool, machining technology parameters (Czerech et al., 2012), or the machining strategy used to create technology programs in CAM software. We can influence through using various optimization algorithms on the last of the above-mentioned parameters (Makhanov, 2007). With their help it is possible to control adaptive interface of tool paths, which can adapt to the topography of the machined surface. However, these are complex operations requiring high skills and specialized knowledge from the person that creating a technological program.

Preparing technological programs in the CAM environment involves choosing a appropriate machining strategy from the available software library and describing its technological parameters. Thanks to that the tool trajectory is stretched on the machined surfaces of the geometric model prepared in the CAD environment. Approximating algorithms used in generating toolpaths in the CAM software, are adjusted to different types of machining strategy and choosing the wrong type of path can adversely affect on the quality of the final product (Lazoglu et al., 2009). Additionally, not properly selected and defined strategy can contribute to increase of geometric deviations and can enlarge the costs, both directly related to the time of machining and indirect, resulting from wear of the machine's working parts or cutting tools.

Toolpath is a trajectory, on which machining tool is moving. The accuracy of path is controlled by two parameters defined by the technologist / CAM programmer. The first one determines approximating algorithm of the machining strategy and it is called the longitudinal approximation. It creates a series of line segments

along path and it is described by value of path tolerance. The second component of the tool trajectory accuracy is a transverse approximation, which is defined during defining the step of toolpath (the distance between the tools' pass). Parameters mentioned above determine the geometric accuracy of manufactured objects. Undervaluation the toolpath tolerance resulting in growth in number of segments thus the technological program capacity increasing and imposes high power of computing machine controller, which working at a high feed rate is forced to process large amounts of data in a very short time. Reducing the path step also increases the volume of the NC program and significantly affect the manufacturing time by increasing the number of tool passes.

In case when the machined surface must, for aesthetic or functional reasons, be subjected to additional technological operations, such as polishing (e.g. forming surfaces in molds for plastics processing), the person performing this treatment is forced to reduce these inequalities left over from previous operations. Their shape and size is defined precisely by the value of the toolpath tolerance and its step. Polishing the surface is very time consuming activity and affects negatively the geometric accuracy of produced parts. So optimally selected and defined machining strategy enables to minimize the costs associated with additional technological operations.

The process of generating tool paths for freeform surfaces is a subject of discussion for many researchers. Optimization of the distribution paths is the element that minimize the geometric deviations of freeform surface machined on numerically controlled machining centers. This process can be based on the using specialized algorithms, which control the distribution of the toolpath on approximated surface. One can distinguish here two leading solutions. Adjusting direction of the tool trajectory (Lazoglu et al., 2009) and the density of the path relatively to the local geometry of curvilinear surface (Agrawal et al., 2006; Choi and Banerjee, 2007; Lee, 2003; Vijayaraghavan et al., 2009). This allows to stabilize the level of irregularities caused by machining and to minimize forces acting during the cut. Moreover, this solution leads to the minimization of machining time (Feng and Su, 2000).

Choi and Banerjee in their work propose the implementation of the algorithms optimizing the tolerance and path step relatively local conditions which results from surface topography. They use isoparametric curves for longitudinal approximation instead of line segments, thus they gain higher accuracy of toolpath. For transverse approximation three cases of shape of inequalities arising from tool pass to identify crucial areas can be distinguished. The first case is a quasi-triangular geometry, which is described by flat base (defined by the local flatness of surface) and two sides (described by the radius of ball endmill), geometries with convex and concave base curvature are the next two cases. Algorithm proposed by Choi and Banerjee uses the two dependences mentioned above and adapts to the actual curvature of the freeform surface.

Using neural networks is not the only solution used for optimization of the trajectory tool distribution on approximated surface. Ding et al. in their paperwork (Ding et al., 2003) propose optimizing algorithm based on projecting additional tool transitions in places that require reduction of cut layer, and then combined them with the base path.

One of the biggest difficulties in process of preparing technological programs in CAM environment is to estimate which one of available strategies will be optimal (will introduce the least noise). Nowadays the production engineer have at disposal two toolpaths, which geometry is close to: parallel lines (Fig. 1a), gradually propagating outlines described by external surface boundaries (Fig. 1b), propagating along or across to ones of surface creating (Fig.1c), stretched between arbitrarily defined curves (Fig.1d) or described by morphic spiral (Fig.1e), or circular (Fig.1f), and then projected on machined surface. Choosing wrong strategy can significantly contribute to the reduction of geometric accuracy of manufactured objects (Schutzer et al., 2006; Zhang et al., 2012).
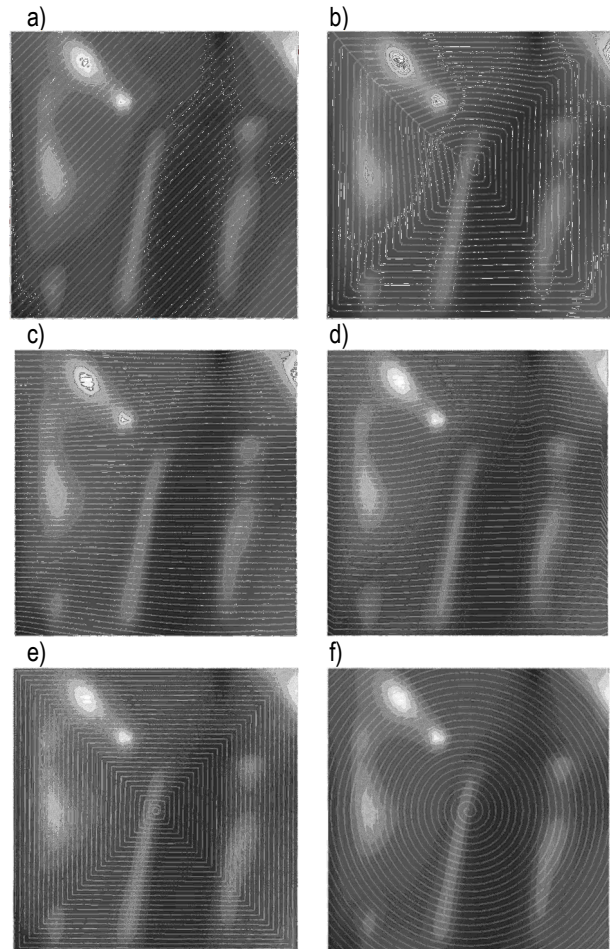
Fig. 1. Example types of machining strategies: a) parallel, b) scallop, c) flowline, d) blend, e) morphic, f) spiral

2. METHODOLOGY AND TEST STAND

The research was designed to study the estimation of geometric deviations values determined by the values of toolpath tolerance and the modeled surface topography. This process has proceeded according to the following algorithm:
1. building geometric model of the manufactured part in CAD module in MasterCAM X5 environment;
2. choosing optimal machining strategies available in CAM module library in software mentioned above;
3. describing machining strategy by defining machining technological parameters;
4. toolpath conversion to vector geometry;
5. division resulting path segments in two equal parts;
6. establishing check points at the ends of the resulting segments;

7. projecting duplicates of points on the approximate lobe of the freeform surface;
8. saving cloud of points of the path and points projected on a surface to the text file;
9. data import into a spreadsheet and inspection software;
10. analyzing the impact of toolpath tolerance on the value and the location of geometrical deviations.

To perform the study a PC computer was used, equipped with MasterCAM X5 application used for creating and editing surface and solid geometrical models and creating technological programs for numerically controlled machine tools. Furthermore, application Geomagic Qualify was used for creating distribution maps of geometric deviations which enables to compare the cloud of points with the geometrical model. Spreadsheet Excel was used as an additional tool in analyze the numerical data.
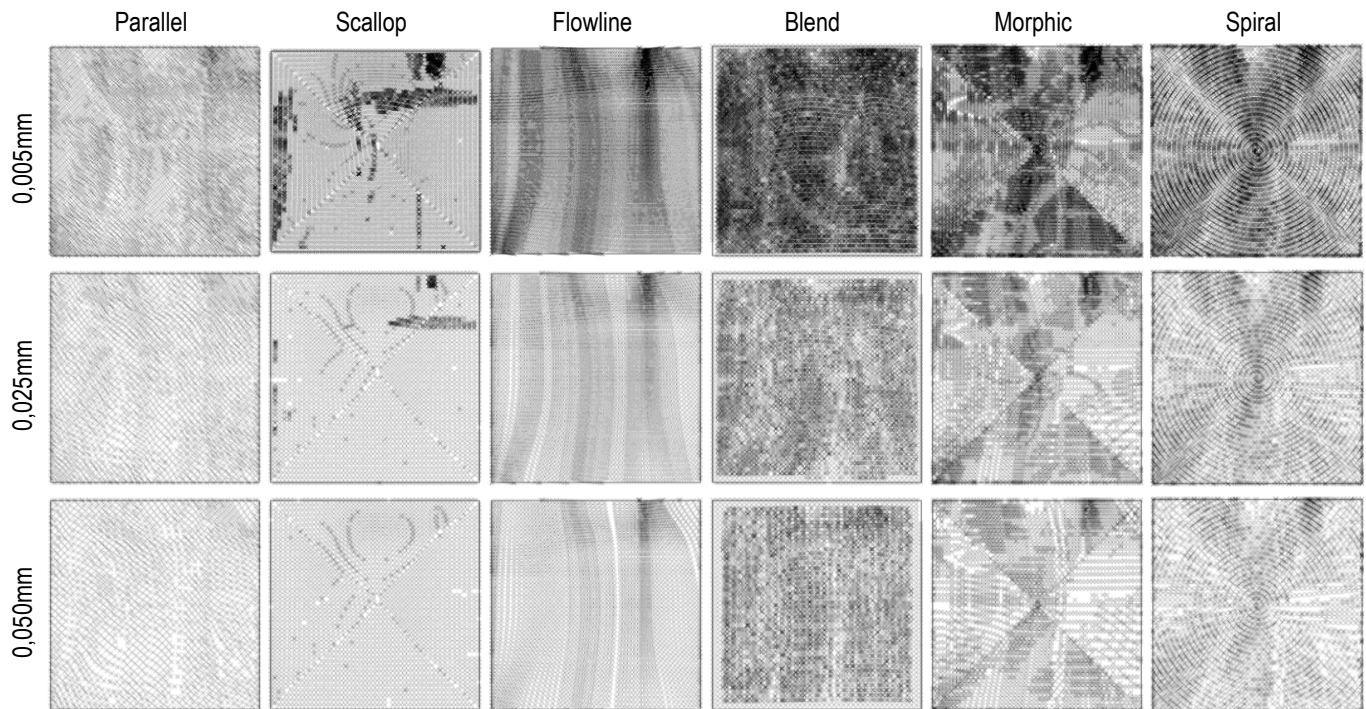

Fig. 2. Distributions of end and mid points of analyzed toolpaths segments for selected tolerance values

3. RESEARCH PROCESS

Following the algorithm mentioned above, lobe of curvilinear surface was prepared as a first. It was modeled in Design module of MasterCAM software by stretching Coons surface on splines that create the web. After carefully analyzing the topography of created geometry, six types of machining strategies were distinguished, which trajectory of the tool had been spread optimally on the machined surface.

The next step was to describe technological parameters of each strategy with unification with parameters such as: path tolerance, transverse step or tool type. After finishing all actions mentioned above, converting the tool trajectory to geometry consisting of line segments that result from the surface approximation had begin. For the study, to accurately depict the impact of tool path tolerance values on the process of constituting deviations, all segments of the path were divided into two parts. As a result, additional points were obtained, giving much greater ability to identify errors of technological programs, that arise during the development phase of machining strategies and help to increase the geometric deviations of machined surfaces.

So prepared geometrical path was a base for creating the control points at the ends of all segments (Fig. 2). Then duplicate of those points were cast on the approximated surface using a toolpath. Thanks to this operation coordinates of nominal points (collective with the surface) and real points (at the ends of path segments) were obtained.

Data, prepared in this way, were exported to a spreadsheet, which undertook further processing and analysis of results.

4. TEST RESULT ANALYZE

Statistic analysis of results obtained in the examination process has allowed to visualize statistic parameters changes determined by the type of strategy and the tolerance values of the path.

In case when the CNC technologist / programmer prepares the technological program used for machining the element limited with curvilinear surfaces, he is able to control the amount of generated segments that create the toolpath by oscillating the tolerance value and, as it turns out, the type of machining strategy (Tab. 1). Unfortunately he is limited with design assumption which define the quality of the machined surface and shape deviation values. This imposes the maximal path tolerance value, while the conversion power of the CNC machine tool driver determines the lower limit of the range. Since working at high feed rate the machine tool cannot cope with such large amounts of data to be processed, and hence will not be able to pass information to the servo drives at the right pace.

By analyzing the values that illustrate the medium values of the geometric deviations (Tab. 1) can be stated, that the largest value are generated by blend path, which is approximating the

surface between two arbitrarily defined curves. Most preferably the flowline path falls here, approximating the surface after its forming. In analyzing the maximal positive and negative deviation values, flowline path is the most advantageous path as well. Unfortunately, it appears that blend, morphic and spiral strategies have very similar characteristics and generate a much larger deviation than a path tolerance value assumed in describing the strategy. It can significantly complicate the process of preparing programs controlling the machine operation. In addition, these paths tend to increase the maximal values of deviations, while reducing the tolerance of the path.

Tab. 1. Geometric deviation statistical parameters summary

	0,005	0,010	0,015	0,020	0,025	0,030	0,035	0,040	0,045	0,050
MEDIAN										
FLOWLINE	0,000	0,000	0,000	0,000	0,000	0,000	0,000	0,000	0,000	0,000
PARALLEL	0,001	0,001	0,002	0,002	0,003	0,004	0,004	0,004	0,005	0,005
SPIRAL	0,001	0,001	0,002	0,002	0,003	0,004	0,004	0,005	0,005	0,006
MORPHIC	0,001	0,001	0,002	0,003	0,003	0,004	0,004	0,005	0,005	0,006
SCALLOP	0,001	0,003	0,004	0,004	0,005	0,005	0,006	0,007	0,007	0,008
BLEND	0,001	0,002	0,003	0,004	0,005	0,007	0,008	0,009	0,010	0,011
MAXIMUM POSITIVE										
FLOWLINE	0,005	0,012	0,013	0,024	0,027	0,027	0,027	0,036	0,027	0,036
SCALLOP	0,017	0,035	0,051	0,053	0,054	0,054	0,054	0,055	0,055	0,055
PARALLEL	0,152	0,152	0,152	0,153	0,154	0,153	0,155	0,154	0,155	0,155
MORPHIC	0,838	0,658	0,345	0,179	0,053	0,105	0,105	0,062	0,049	0,049
SPIRAL	0,838	0,658	0,345	0,179	0,053	0,105	0,105	0,062	0,049	0,049
BLEND	0,844	0,662	0,346	0,179	0,081	0,105	0,105	0,083	0,084	0,109
MAXIMUM NEGATIVE										
FLOWLINE	-0,017	-0,017	-0,017	-0,017	-0,017	-0,017	-0,017	-0,017	-0,017	-0,017
SCALLOP	-0,036	-0,040	-0,045	-0,045	-0,046	-0,046	-0,046	-0,046	-0,046	-0,046
PARALLEL	-0,098	-0,100	-0,100	-0,103	-0,104	-0,105	-0,105	-0,105	-0,105	-0,105
MORPHIC	-0,405	-0,411	-0,382	-0,384	-0,270	-0,388	-0,204	-0,108	-0,108	-0,108
SPIRAL	-0,405	-0,411	-0,382	-0,384	-0,270	-0,388	-0,204	-0,108	-0,108	-0,108
BLEND	-0,411	-0,418	-0,387	-0,389	-0,326	-0,393	-0,323	-0,328	-0,328	-0,328
NUMBER OF POINTS										
BLEND	15346	11690	9900	8658	6635	7022	6628	6348	6065	5767
FLOWLINE	6341	4460	3550	3003	2838	2703	2666	2585	2571	2573
MORPHIC	9959	7158	5917	5048	4608	4244	3934	3720	3539	3336
PARALLEL	6783	4996	4164	3642	3341	3103	2812	2647	2545	2405
SCALLOP	11317	7834	6551	5665	5258	4832	4554	4293	4065	3758
SPIRAL	8773	6322	5081	4591	4217	3847	3632	3221	3221	3089
BLEND	15346	11690	9900	8658	6635	7022	6628	6348	6065	5767

Furthermore, an analysis of the distribution of geometric deviations in terms of the percentage of points in each interval values of deviations (Fig. 3) has been made. In this case it is also clearly seen that the flowline path best reproduces approximated surface, because even with path tolerance equaled 0.05mm all deviations in measuring points are within the limits of 0.02mm, what is determined by a small value of standard deviation. Analogously to this can be estimated, that using for creating the part of blend path would be a less favorable solution, because its nominal distribution is almost flat and illustrate occurrence of such deviation values, which are significantly bigger than implied tolerance. Path created by scallop strategy also performs poorly. Morphic, spiral and parallel strategies generate identical deviation distributions, what characterize their trajectories, which quality is far much poorer than flowline path's.
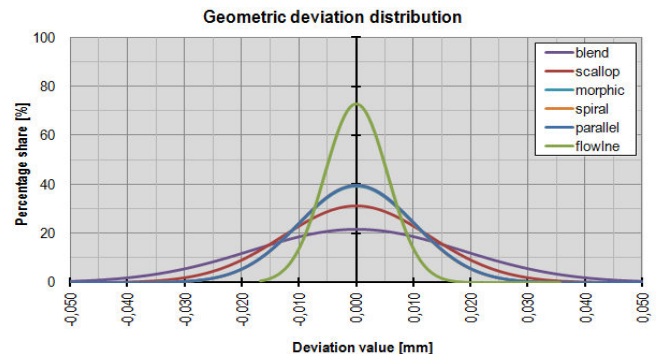
Fig. 3. Geometric deviation distribution for 0.05mm toolpath tolerance.

Brining great part of information about the process of creating geometric deviations and allowing to estimate the influence of curvilinear surfaces topography is to compare the cloud of given points with the nominal model (Fig. 4). Surface topography correlation with value and intensity of deviation occurrence is ideally illustrated here. As can be seen on their distribution maps, the biggest positive values of deviations are located in areas of cavity on analyzed surface (the material forming the surplus is not fully collected). However on bulges and their immediate vicinity deviations with the biggest negative values are located (working tool will cut through machined surface).

Analyzing all charts it can be concluded, that the path created by flowline strategy is characterized by high liquidity of approximating algorithm and generates minimal amounts or values of geometric errors. Other machining strategies are far less favorable and their usage in process of creating technological programs can contribute to significant reduction of accuracy and the manufactured object can be recognize by quality control as a fault.
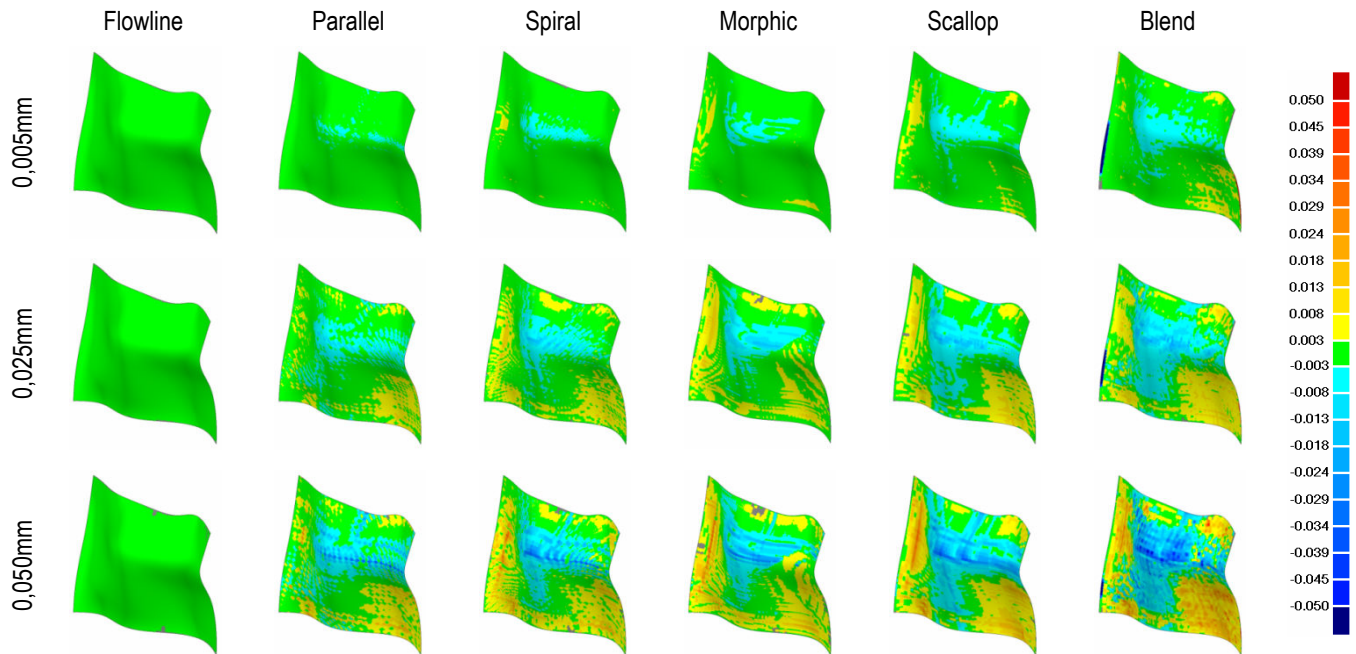

Fig. 4. Geometric deviation distribution maps for selected toolpath tolerances values

5. CONCLUSIONS

After conducting thorough research and statistical analysis the impact of toolpaths tolerance on forming geometrical deviations, the following conclusions are constituting:

a) method proposed in this paper is a fine tool that enables to estimate which machining strategy brings the smallest geometrical errors to technological programs controlling the machine tool;

b) this method also enables to estimate that influence has a path tolerance value on deviation creating process and technological program volume;

c) choosing the optimal machining strategy can increase the accuracy of manufactured parts, which is identical to the reduction of production costs;

d) mismatched machining strategy may increase the intensity of local sweeps and not completely removing the material stock, which can lead to difficulty in matching the two cooperating components;

e) undervaluation toolpath tolerance can increase geometrical deviations of produced objects, which can cause difficulties for the engineers and CNC programmers prepare NC programs.

Based on these research it will be possible to move to the next stage which will develop a method of error correction on level of creating technological programs and verifying the impact of technological parameters such as: cutting speed, feed rate of the blade or the diameter of the tool on the technological process of constituting the surface layer.

REFERENCES

1. **Agrawal R., Pratihar D., Choudhury A.** (2006), Optimization of CNC isoscallop free form surface machining using a genetic algorithm, *Machine Tools & Manufacture*, 46, 811–819.
2. **Choi Y., Banerjee A.** (2007), Tool path generation and tolerance analysis for free-form surfaces, *Machine Tools & Manufacture*, 47, 689–696.
3. **Czerech Ł., Kaczyński R.** (2013), Influence of CNC machine tool technical condition on the geometrical accuracy of freeform surfaces, *Solid State Phenomena, Mechatronic systems and materials V*, 315-320.
4. **Czerech Ł., Kaczyński R., Werner A.** (2012), Wpływ wybranych parametrów technologicznych na dokładność geometryczną powierzchni NURBS wykonywanych na frezarskich centrach obróbkowych, *Mechanik*, Vol. 1, Warszawa, 14.
5. **Ding S., M. Mannan, Poo A., Yang D., Han Z.** (2003), Adaptive isoplanar generation for machining of free-form surfaces, *Computer-Aided Design*, 35, 141-153.
6. **Feng H., Su N.** (2000), Integrated tool path and feed rate optimization for the finishing machining of 3D plane surfaces, *Machine Tools & Manufacture*, 40, 1557–1572.
7. **Lazoglu I., Manav C., Murtezaoglu Y.** (2009), Toolpath optimization for freeform surface machining. *Manufacturing Technology*, 58, 101–104.

8. **Lee E.** (2003), Contour offset approach to spiral toolpath generation with constant scallop height. *Computers -Aided Design*, 35, 511-518.
9. **Makhanov S.** (2007), Optimization and correction of the tool path of the five-axis milling machine Part 1, Spatial optimization, *Mathematics and Computers in Simulation*, 75, 210–230.
10. **Saviol E., De Chiffre L., Schmitt R.** (2007), Metrology of freeform shaped parts, *Manufacturing Technology*, 56, 810–835.
11. **Schutzer K., Helleno A., Castellari, Pereira S.** (2006), The influence of the manufacturing strategy on the production of molds and dies, *Materials Processing Technology*, 179, 172–177.
12. **Vijayaraghavan A., Hoover A., Hartnett J., Dornfeld D.** (2009), Improving endmilling surface finish by workpiece rotation and adaptive toolpath spacing, *Machine Tools And Manufacture*, 49, 89–98.
13. **Zhang X., Xie J., Xie H., Li L.** (2012), Experimental investigation on various tool path strategies influencing surface quality and form accuracy of CNC milled complex freeform surface, *Advanced Manufacturing Technologies*, 59, Issue 5-8, 647-654.

SIMPLIFIED COLLISION DETECTION IN 4R SERIAL MANIPULATORS

Artur HANDKE[*]

[*]Division of Machine Theory and Mechatronic Systems, Faculty of Mechanical Engineering, Wroclaw University of Technology,
ul. Łukasiewicza7/9 50-150 Wrocław, Poland

artur.handke@pwr.wroc.pl

Abstract: This paper concerns the problem of designating criteria for assessing the possibility of a collision between the elements of serial manipulators with three rotary joints allowing to flex the segments in common plane oriented by rotating the fourth connection. The issue of contactless and efficient functioning of described group of manipulators has been considered in the spatial system. Equations were derived determining the possibility of a collision between selected segments of both manipulators. Collision detection model isn't based on the information from the tactile sensors, but only on the relative position between the segments of manipulators. Based on the parameters defining the collision, the search for method of impossible collision was set on designing level, in order to minimize the time needed to examine all possible scenarios of collisions between segments. The results were included in development of methods and algorithms for planning and controlling movements of finger modules in anthropomorphic manipulator during grasping objects of indeterminate shape.

Keywords: Serial Manipulator, Collision Detection, Movement Planning

1. INTRODUCTION

The problem of collision detection is an important aspect of the efficient execution of object manipulation process by group of serial manipulators. Collision is a particularly common situation in many operating spatial manipulators. An examined group of manipulators concerns fingers modules of an anthropomorphic hand type manipulator Hand-K3 (Handke and Twaróg, 2010) with adjustable orientation of the planes, in which three revolute joints operate. Since the collision detection cannot be based on tactile sensory, thus the simplest method to detect collision between moving segments' of discussed manipulators is to constantly determine the distance between them, based on their position in reference to the common system of coordinates. However, to minimize the time necessary to verify the established system of the collision criteria, the rationality of such solutions should be taken into account, due to energy consumption.

2. TYPES OF COLLISIONS BETWEEN FINGER MODULES OF ANTHROPOMORPHIC MANIPULATOR IN SPATIAL SYSTEM

In order to determine the parameters that clearly define the occurrence of a collision in the group of cooperating manipulators, two main criteria for collision detection were established. Discussed in this anthropomorphic manipulator Hand-K3 four combinations of subgroups consisting of three finger modules were set. It is related to the established algorithm for planning the movements of finger modules (Handke and Twaróg, 2012), in order to fully grasp the objects of indefinite shape, without the use of vision systems, as well as information from the tactile sensor network (De Luca, 2006). The collision in spatial system occurs in three directions, and due to the distinctive construction of the manipula-

tor, it mainly occurs in a two-dimensional plane in which the movable segments revolute. This is only a simplification in order to separate the three-dimensional space from a plane containing the two directions of a collision in combination with the third direction, normal to this plane.
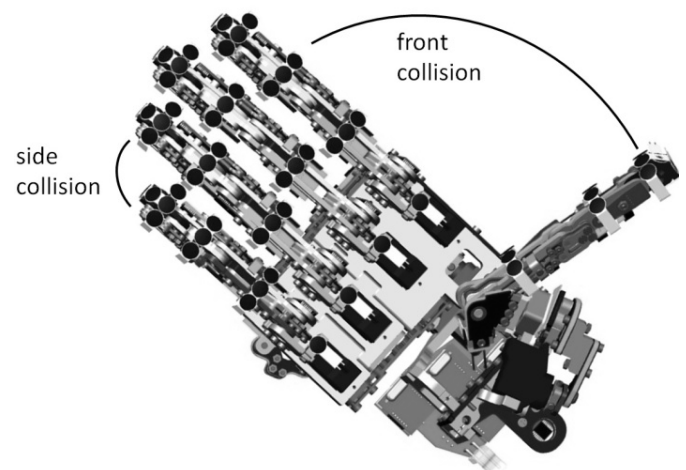

Fig. 1. Types of possible collisions
in Hand-K3 anthropomorphic manipulator

The five-fingered manipulator of this type can have distinguished four pairs of fingers working in opposition to the thumb module to form four main planes in which front collision occurs (Fig. 1). Due to the possibility of variable orientation of the main planes of rotational finger modules in a limited range, it is necessary to define also a collision occurring between adjacent finger modules. Therefore, six pairs were separated among finger modules working initially in approximately parallel planes, to determine side collision.

3. PARAMETERIZATION OF FRONT AND SIDE COLLISIONS

Analysis of the possibility of a collision was conducted by calculating the distance between the geometrical center of the selected segment of finger module (Fig. 2), and the plane that defines the type of collision. Analytical approach to this problem is often implemented by many authors (Bosscher, 2011). Because of the structural complexity of each segment, dimensions of the most distant surfaces of the *m.i* system of *m*-segment in *i*-finger module were assumed.
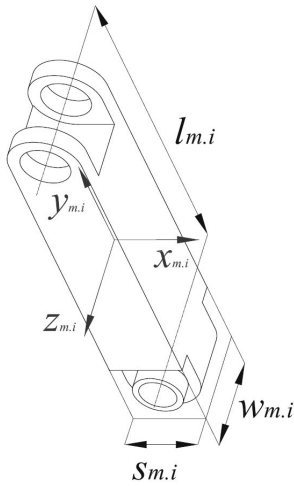

Fig. 2. Finger unit's segment basic dimensions

According to the proposed move control algorithm (Handke and Twaróg, 2012), collisions in finger modules are considered in a group of three among all five. Fig.3 shows a selected group containing one finger j, set in opposition to the others.
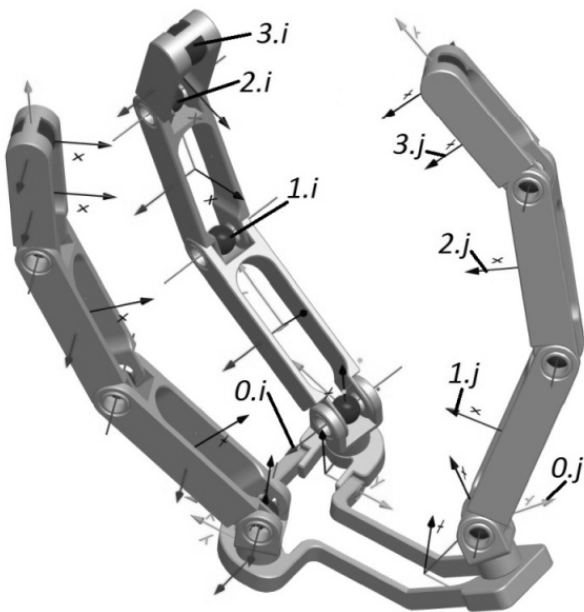

Fig. 3. Arrangement of the coordinates systems
of the selected group of 3 finger modules

In order to create the parameters necessary to unambiguously identify a specific distance between the point and the plane,

a general transformation matrix (1) between systems of *i* and *j* finger, was created, similar to the existing work (Spencer, 2008).\

$$^{m.i}A_{n.j}(t) = {}^{0.j}A_{n.j}(t)\,{}^{0.i}A_{0.j}\,{}^{m.i}A_{0.i}(t) \tag{1}$$

The transformation matrix between rotating joints that orients the main planes, in which all further segments flex, is conditionally fixed, according to the settings of rotations of *0.j* and *0.i*. The re-derivation of this matrix is necessary when the configuration of the main planes of joints *1.i(j) ÷ 3.i(j)* is changed.

$$f_k(A) = B \times A \times \begin{bmatrix} 0 & 0 & 0 & 1 \end{bmatrix}^T \tag{2}$$

where: k – a specified coordinate of the Cartesian system

$$k \begin{cases} x \Rightarrow B = \begin{bmatrix} 1 & 0 & 0 & 0 \end{bmatrix} \\ y \Rightarrow B = \begin{bmatrix} 0 & 1 & 0 & 0 \end{bmatrix} \\ z \Rightarrow B = \begin{bmatrix} 0 & 0 & 1 & 0 \end{bmatrix} \end{cases} \tag{3}$$

To determine the f_k distance searched in direction of the given system, relative to which it is established, the general form of the distance between the two systems of selected segments of finger modules was formed (2). Because f_k distance is a scalar variable, depending on the selected direction, vector B takes adequate form (3).

3.1. Front collision

The situation in which a collision between segments in the frontal plane of given segment is possible, may occur only for four pairs of opposing fingers. However, the situation in which two finger modules move in parallel planes occurs rarely in anthropomorphic manipulators with variable orientation of main planes. At this point, the situation with no front collision was omitted, due to the dimensional settings of the fingers.
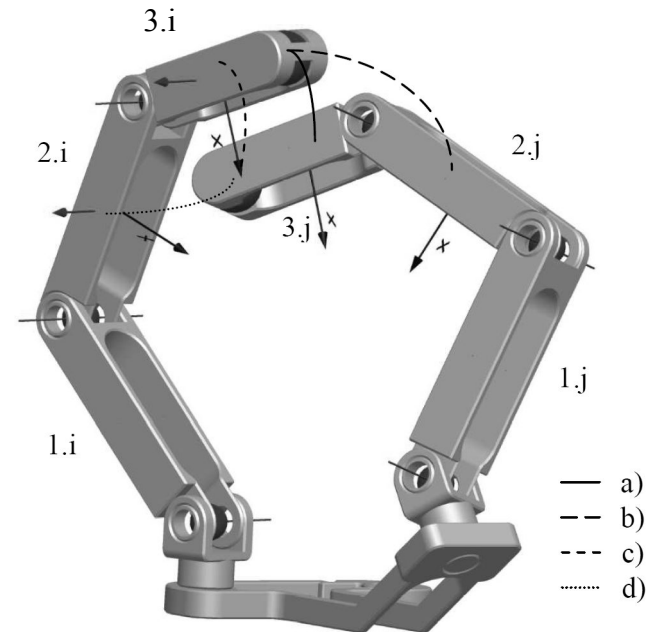

Fig. 4. Multiple front collision between opposite finger module's:
a) front collision of *3.i* segment relative to *3.j* segment - 2nd
condition, b) front collision of *3.i* segment relative to *2.j* segment -
1st condition,c) front collision of *3.j* segment relative to *3.i* segment
- 1st condition,d) front collision of *3.j* segment relative
to *2.i* segment - 1st condition

Two components of the f_k parameter: x and y are taken into consideration, therefore two conditions were created, evaluating the occurrence of a front collision. The first condition requires a reference of f_x distance between m-segment of i-finger relative to the n-segment of j-finger, to the width of the front section of the two segments (4).

$$p_x = \left| f_x \left({}^{n.i}A_{n.j} \right) \right| - \left(s_{m.i} + s_{n.j} \right) \tag{4}$$

The second condition concerns the additional length of the front section of the segment, which measured distance f_y is relative to.

$$p_y = \left| f_y \left({}^{n.i}A_{n.j} \right) \right| - \left(s_{m.i} + \frac{l_{n.j} + s_{n.j}}{2} \right) \tag{5}$$

For both equations establishing necessary conditions for the existence of front collision, the orientation of z-axis of $m.i$ system relative to segment $n.j$ is not important. Occurrence of a collision can be confirmed when the parameter p_x or p_y assumes a value less than 0.

3.2. Side collision

The last condition for determining the occurrence of a collision between the considered segments is the positive value of the parameter p_z according to the equasion (6). In this case only the widths of the two segments are taken into consideration.

$$p_z = \left| f_z \left({}^{n.i}A_{n.j} \right) \right| - \left(w_{m.i} + w_{n.j} \right) \tag{6}$$

During the motion control and planning of the segments, it was necessary to determine the motion priority in the selected pair of finger modules. The motion priority condition became critical for the adjacent finger modules. In a situation where a front collision has not yet occurred, and a side collision has been registered, it is possible to continue operation of both modules. Therefore it is obvious, to deny the priority of motion to the finger module, relative to which the possibility of side collision occurrence has been registered.
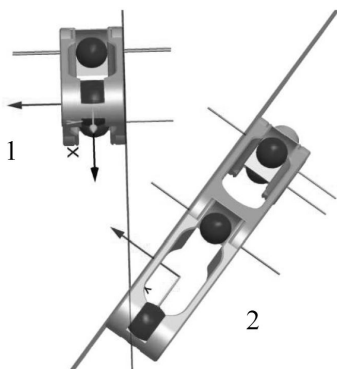

Fig. 5. Unilateral side collision between finger modules

The discussed situation can be seen in figure 5, in which the finger module 1 does not cause a collision with the finger module 2, according to the value of the parameter f_z, while the f_z value recalculated for the finger 2 relative to finger 1 this time implicates side collision.

Finally it is possible to determine the last condition allowing the movement in one direction through the use of Heaviside function in equasion (7), where parameter p_a is a resultant of p_z and a product of p_x and p_y parameters.

$$a \in (x, y, z) \Rightarrow v_a = H(p_a) \frac{\partial p_a}{\partial t} \tag{7}$$

These collision detection methods allow on a motion planning stage, to assess the possibility of a collision in the following calculation step and in time decide to withdraw the selected finger module if neccessary.

4. ELIMINATION OF IMPOSSIBLE COLLISIONS

The process of verification of possible collisions between two selected 4R serial manipulators of established structure, in this case finger modules in Hand-K3 anthropomorhic manipulator, depends on the number of possible collisions. To minimize the time necessary to inspect the possible collisions in any combination, it was crucial to determine the method of exclusion of impossible collision scenerios within searchable combinations. The maximum number of steps needed to verify collision between the three segments of the i-finger and 3 modules of j-finger is 9, and because the dependency is bilateral, 18 calculations were required for one pair of figer modules. Therefore, an initial verification was performed at the design stage. Similarly to the procedure while using virtual reality (Zaeh MF 2004). The first condition for the absence of the collision possibility, concerns parallel orientation of the main planes, in which all 3 segments of each finger module operate. For adjacent finger modules, the comparison of the main planes orientation angle values is sufficient, while the considered pair of modules contains the opposite finger module, it is possible to evaluate their parallelism through comparison of the three values of the f_z parameter (Equation 8). Points O, K, and L must be located on a common plane and be included to the segment orientating the main working plane of finger module, relative to which these values are determined.

$$f_z \left({}^{0.i}A_{0.j} \right) = f_z \left({}^{K.i}A_{0.j} \right) = f_z \left({}^{L.i}A_{0.j} \right) \tag{8}$$

However, the existence of a collision is still possible for finger modules that have parallel main working planes, when the distance between those planes meet the condition in equation 9.

$$\left| f_z \left({}^{0.i}A_{0.j} \right) \right| < \frac{s_{1.i} + s_{1.j}}{2} \tag{9}$$

Another condition that eliminates the possibility of a collision, was created in graphical form. The goal of this method is to artbitraly exclude some pairs of mobile segments from the assemblage of possible collisions. Due to the excessive complexity of many variable derivatives calculations required to find the extreme distance between given combination of the segments, the analytical approach was excluded. For this purpose, the knowledge of the workspace, determined by the motion range of segments was used. In the process of collision diagnosis, it is crucial to consider the motion range of joints orienting the main planes of verified modules. Created for this purpose the areas (Fig. 6) represent set of trajectory points of the rotation axis of each segment in the entire motion range of connections orienting the main

planes of finger modules. These are the longest trajectories available for each module relative to the angle limits of their rotation.
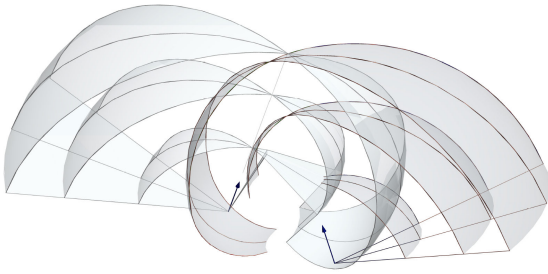

Fig. 6. Workspaces of selected modules of opposing fingers in anthropomorphic manipulator

Because the graphical representation of the workspace in spatial system is not sufficiently clear, an established plane was introduced, on which sets of the trajectories were projected (Fig. 7). This allowed for a simple verification of the possibility of a given pair of segments of collision between each other. In situation where an $t_{n.j}$ trajectory concerning n-segment of j-finger, intersects with the $a_{m.i}$ workspace of m-segment in i-finger, a pair of these segments remains in the assemblage of possible collision combinations.
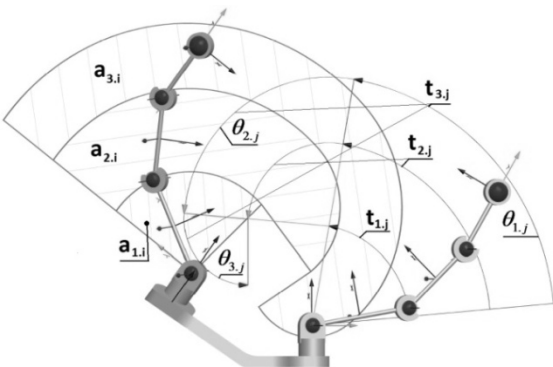
Fig. 7. View of range of finger modules for selected orientation angles of the main working planes

Using the introduced projection plane of the workspaces - $a_1 \div a_3$ and the maximal trajectories $t_1 \div t_2$ of all segments in given pair of finger modules, a graphical representation of possible collision assemblage have been acquired (Fig. 8).
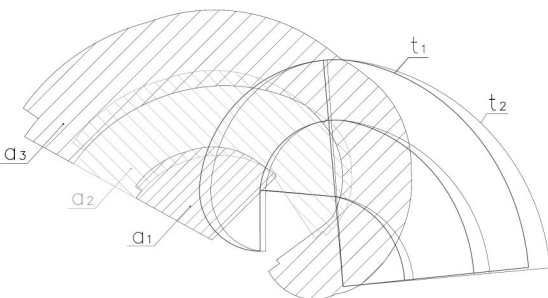
Fig. 8. The total working area ($a_1 \div a_3$)of i-finger module segments relative to maximal trajectory ($t_1 \div t_2$) of j-finger module segments

Based on this established graphical representation, the number of calculations performed during the search for potential collisions between segments of the manipulator can be limited through the exclusion of impossible combinations at the design stage. Thus it is possible to minimize the calculation time, needed for the control modules to estimate the trajectory before the further manipulation stages.

5. CONCLUSIONS

Presented in this paper methods for assessing the occurrence of collisions between moving segments of anthropomorphic manipulator's finger modules, allowed to increase the effectiveness of movement planning of individual revolute joints by the motion control system. Introducing separate and independent drive control and movement planning computational modules in each finger module based on these methods, allowed to accelerate the operation of the finger modules in the anthropomorphic manipulator, in particular reducing the number of calculations performed at every step of the movement planning. The simplification of established conditions for the collision assessment between moving segments ensured no further increase of drive control units load in the anthropomorphic manipulator.

REFERENCES

1. **Bosscher P., Hedman D.**(2011), Real-time collision avoidance algorithm for robotic manipulators, Industrial Robot: An International Journal, Vol. 38, No. 2, 186-197
2. **De Luca A., Albu-Schaffer A., Haddadin S., Hirzinger G.**(2006),Collision Detection and Safe Reaction with the DLR-III Lightweight Manipulator Arm, Proceedings of the 2006 IEEE/RSJ International Conference on Intelligent Robots and Systems,Beijing
3. **Handke A., Twaróg W.** (2010),Correlation of sensory parameters' mathematical models with the kinematic structure of a HAND-K3 human hand type manipulator, *Acta Mechanica et Automatica*,Vol. 4 No. 3.
4. **Handke A., Twaróg W.** (2012), *Method for Plannig the Finger's Movement in the Anthropomorphic Manipulator Hand-K3m Using a Tactile Sensors Network, with the Aim of Optimal Grasping*, Mechanism and Machine Science, Vol. 8, 309 - 315.
5. **Spencer A., Pryor M., Kapoor C., Tesar D.**(2008), Collision Avoidance Techniques for Tele-Operated and Autonomous Manipulators in Overlapping Workspaces, IEEE International Conference on Robotics and Automation ,Pasadena.
6. **Zaeh M.F., Egermeier H., Petzold B., Spitzweg M.** (2004), Dexterous Object Manipulation in a Physics Based Virtual Environment, Proceedings of Mechatronics & Robotics 2004, Aachen, 1340-1344.

MATERIAL AND THERMAL ANALYSIS OF LASER SINTERTED PRODUCTS

Radovan HUDÁK*, Martin ŠARIK*, Róbert DADEJ*, Jozef ŽIVČÁK*, Daniela HARACHOVÁ**

*Faculty of Mechanical Engineering, Department of Biomedical Engineering and Measurement, Technical University of Košice,
Letná 9, 042 00 Košice, Slovakia
**Faculty of Mechanical Engineering, Department of Machine Design, Transport and Logistic, Technical University of Košice,
Letná 9, 042 00 Košice,   Slovakia

radovan.hudak@tuke.sk, martin.sarik@tuke.sk, robert.dadej@tuke.sk, jozef.zivcak@tuke.sk, daniela.harachova@tuke.sk

Abstract: Thermal analysis of laser processes can be used to predict thermal stresses and consequently deformation in a completed part. Analysis of temperature is also the basic for feedback of laser processing parameters in manufacturing. The quality of laser sintered parts greatly depends on proper selection of the input processing parameters, material properties and support creation. In order to relatively big heat stress in the built part during sintering process, the thermal simulation and thermal analysis, which could help better understand and solve the issue of parts deformations is very important. Main aim of presented work is to prepare input parameters for thermal simulations by the use of RadTherm software (Thermoanalytics Inc., USA), directly during the sintering process and after the process and find out the impact of the heat stress on a final shape and size of the prototype. Subsequently, an annealing process of constructed products after DMLS could be simulated and specified.

Key words: Material Analysis, Direct Metal Laser Sintering, Thermal Analysis, Deformations, Thermal Analyzing Software,
Metrotomography

1. INTRODUCTION

Laser sintering or selective laser sintering (SLS) is an additive manufacturing technique that uses a high power laser to fuse small particles Fig. 1, of plastic, metal (DMLS), ceramic, or glass powders into a mass that has a desired three-dimensional shape (http://www.substech.com/dokuwiki/doku.php?id=sinteringofmetals). It is kind of thermal treatment of a loose metal powder or compact at temperature below melting point of the main constituent, for purpose of increasing its strength by bonding together of the particles. Laser selectively fuses powdered material by scanning cross-sections generated from a three dimensional (3D) digital model of the part designed by computer-aided design (CAD) on the surface of powder bed. After each cross-section is scanned, the powder bed is lowered by one layer thickness, than a new layer of material is applied on top, and the process is repeated until the part is completed (http://www.substech.com/dokuwiki/doku.php?id=sinteringofmetals).

Laser sintering is complicated because of its fast laser scan rates and material transformations in a very short timeframe. The temperature field was found to be inhomogeneous by many previous researchers (Wang et al., 2002; Kruth et al., 2003; Simchi, 2006; Kolossov et al., 2004; Zhang et al., 2010). Thermal distortion of the fabricated part is one of the main issues in selective laser melting SLM (Contuzzi et al., 2011). Meanwhile, the temperature evolution history in laser sintering has significant effects on the quality of the final parts, such as density, dimensions, mechanical properties, microstructure, etc. for metals, large thermal gradients increase residual stresses and deformation, and may even lead to crack formation in the fabricated part (Zeng et al., 2012). A case study of main characteristics of LS temperature distribution and effects of process parameters to temperature was summarized by Zeng, Pal and Stucker (Zeng et al., 2012).

The goal of this study was to analyze the intraosseal dental implants in aspect of material and surface properties and prepare the methodology of thermal analysis of product during and after manufacturing process by DMLS technology.

2. MATERIAL AND METHODS

Material analysis was realized by the use of electron microscope analysis, EDX analysis, and measurement of hardness. EDX analysis (Energy-Dispersive X-Ray) is analysis of chemical composition of surface layer of the tested part. Observation was performed by microscope JEOL JSM-7000F, with analyzer INCAx - sight from Oxford Instruments and microscope JEOL JSM-35CF, with analyzer LINK AN 10/85S. For the measurement of microhardness was used light microscope with microhardness device Hanemann, applicated load was 50 g. Microhardness was measured on samples which were polished and fine burned, due to the detection of grain boundaries. The five values on eight samples were measured on each sample, and average value was calculated. Samples were sorted form Ti1 to Ti8. Material of samples was titanium alloy intended to use in biomedical applications. Testing models were fabricated using Ti64 material from EOS Company (EOS GmbH, Germany). EOS Titanium alloy Ti64 is a pre-alloyed Ti6AlV4 alloy in a fine powder form. Parts built from EOS Ti64 fulfil the requirements of ASTM F1472 regarding maximum concentration of impurities. Physical and mechanical properties of EOS Ti64 are – density: 4430 kg/m3, thermal conductivity: $\lambda = 6.6$ W/mK, melting temperature: $T = 1670\degree C$, tensile strength: $R_m = 1150 \pm 60$ MPa. Inert atmosphere was represented by argon (Ar) gas atmosphere as environment in process chamber during the sintering process. Thermal conductivity of argon: $\lambda = 0,016$ W/mK.

Typical sintering furnace has three zones, first is preheating zone – for remove lubricant and other organic material, second is sintering zone – where the diffusion occurs and last is cooling zone – where the sintered parts cooled down. The EOSINT M 280 (EOS GmbH Germany) was used for DMLS process. The system is equipped with a solid state 200 watts laser which provides high quality radiation and stable performance. Process chamber consists of three systems, shown on Fig. 1, building system 21 dm3, dispenser system 26 dm3 and a collector system 13 dm3. Building system contains building platform with these parameters: wide (W) x high (H): 250 x 250 mm, thickness: thk = 22 mm, material – 1.1730 tools steel, surface: mechanical machined. General technical parameters of EOSINT M 280 are minimum recommended layer thickness: 30µm, value of volume in time is about: 3 mm3/s, minimum wall thickness: 0.3 – 0.4 mm and surface roughness: Ra = 0.36 – 0.48.
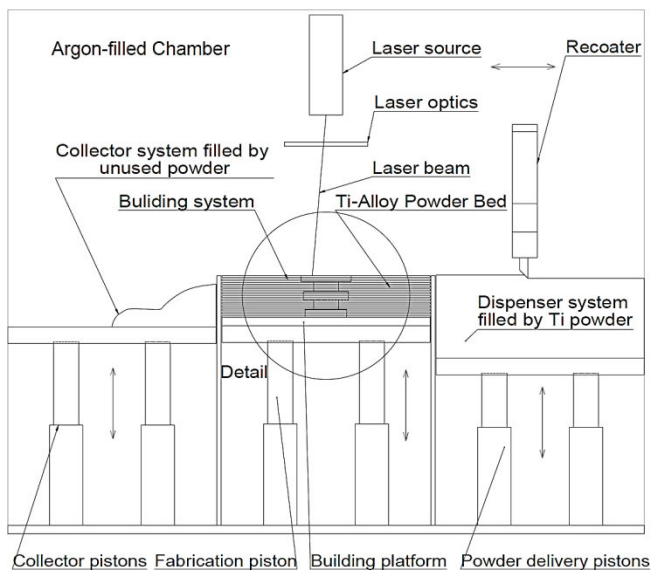
**Fig. 1.** Scheme of DMLS process on machine EOSINT M 280 detail of building platform is shown below
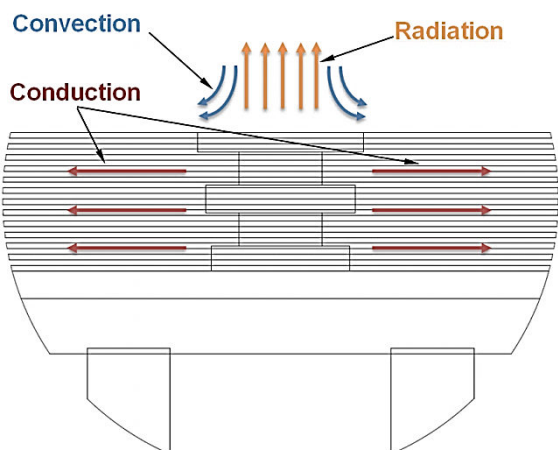
Fig. 2. Detail of building platform with three modes of heat transfer shown by different colors

Metrotomographic machine Metrotom 1500 (Carl Zeiss, Germany) was used for the purposes of visual and quantitative expressions of deformations of pre-prepared samples with these technical parameters – the maximum size of measured compo-

nents (x, y, z): 300 x 300 x 300 mm, maximum weight of parts: 50 kg, power source: 225 kV / 225 W, resolution detector: 1024 x 1024 points and safety: steel housing with lead cladding meets the standards of DIN 54113 needed for full protection operator.

The testing model created for purposes of thermal analysis was designed in 3D CAD software SolidWorks (Dassault Systèmes SolidWorks Corporation USA, CANADA). Testing model and dimension changes after DMLS process caused by heat stress are shown on Fig. 3.
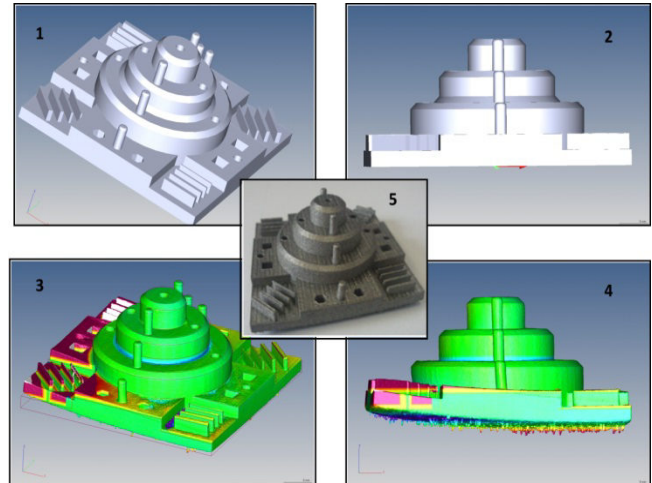
Fig. 3. Base 3D model (3.1, 3.2), base 3D model (3.3, 3.4) in comparison with built, after scanning in Metrotom 1500 (visualization of defor-mation)

The heat stresses and thermal changes are affecting dimensions and shapes of fabricated parts, what requires an adequate heat treatment (Kulesza et al., 2012; Praslicka et al., 2013). As each part is different and many parameters can be changed, it is important to predict and simulate heat processes (stresses) before the DMLS process of 3D printing. For modeling and simulation of heat conduction and fabricated parts finite element deformation analysis during and post – DMLS processes several software applications can be used.

SINDA/FLUINT (Network Analysis Inc., USA) is tool for design of thermal distribution and fluid flow analysis in complex systems. Another application is FloEFD (FlowSim Pty Ltd., Australia), which is analytic tool with strong connection on main MCAD systems.

The RadTherm (Thermoanalytics Inc., USA) is thermal analyzing software based on finite element method analysis, which was implemented in to the simulation algorithms. RadTherm solves the energy balance equation simultaneously for convection, conduction, and radiation. All temperature and heat load data are input as constants or as functions of time at user discretion. RadTherm utilizes the time-averaging Crank-Nicholson implicit finite difference scheme to discretize the governing equations (http://www.thermoanalytics.com/products/radtherm).

After importing the 3D geometry in appropriate thermal analysis software was very important to set the boundary conditions.

Classical Fourier heat transfer equations are the most common for describing the temperature distribution. Based on the Fourier equation, various models have been developed by combing latent heat, material thermal property nonlinearity, laser heat source distribution and interaction between a laser beam and powder bed (http://www.thermoanalytics.com/products/radtherm, Jiangui et al., 2008; Jiang et al., 2002l Baojun and Fazhong, 2002).

Heat transfer is that section of engineering science that studies the energy transport between material bodies due to a temperature difference (Lienhard IV and Lienhard V, 2012; Lewis et al., 2004; Vozda et al., 2012). During the sintering process and cooling phase of sintered parts are thermal conduction and thermal convection very important modes for data collection and evaluation of heat effects. So there is need to define main equations for next work.

Tab. 1. Input and output parameters for thermal simulation in RadTherm

Input Parameters	Output Parameters
Density – ρ [kg/m^3]	Temperature of each element – T_E [˚C]
Specific heat – c_p [J/kgK]	
Thickness of part – th_P [mm]	Temperature range of each element – $T_{Emax} - T_{Emin}$ [˚C]
Thickness of powder layer – th_L [mm]	
Thermal conduction – λ [W/mK]	Maximum reached temperature – T_{max} [˚C]
Convective heat transfer coefficient – h_C [W/m^{2}K]	
Temperature of medium (Ar) – T_{Ar} [˚C]	Minimum reached temperature – T_{min} [˚C]
Volume of medium (Ar) – V_{Ar} [m^3]	
Temperature of preheating – T_P [˚C]	Plot of temperature vs. time – T/t [˚C/s]
Time of preheating – t_P [s]	
Sintering temperature – T_S [˚C]	The course of temperatures in time – [s]
Time of sintering – t_S [s]	
Cooling temperature - T_C [˚C]	Velocity of heating in time – T_{VH}/t [˚C/s]
Time of cooling – t_C [s]	
Heat capacity – C [J/m^{3}K]	Velocity of cooling in time – T_{VC}/t [˚C/s]
Number of layers – n_L	

Thermal Convection consists of two forms, either forced (artificial) and helpful or natural and free form. Next formula presents the convection heat transfer through a surface area at specific temperatures:

$$q = h_c A dT \tag{1}$$

where: q – is transferred heat per unit of time [W], A – is surface area of heat transfer [m2], hc – is convective heat transfer coefficient [W/m2K] or [W/m2˚C], dT – is difference of temperature among surface and volume of fluid [K] or [˚C].

Thermal Conduction is the transfer of heat between substances that are directly in contact to each other. The conduction mode of heat transport occurs either because of an exchange of energy from one molecule to another, without the actual motion of the molecules, or because of the motion of the free electrons if they are present. Equation to calculate the necessary heat to increase the temperature of body only if between temperatures will not be phase change.

$$Q = cm(t - t_0) \tag{2}$$

where: Q – is heat [J], c – is specific heat capacity [Jkg^{-1}K^{-1}], m – is weight [kg], $(t - t_0)$ – reduction of a new temperature from the initial temperature [K].

In (3) is calculation of heat conduction between two ends of metal stick where temperatures are T_1 and T_2.

$$\Delta Q = \frac{\lambda S (T_2 - T_1)}{L} \Delta t \tag{3}$$

where: λ – is specific heat conductivity [Wm^{-1}K^{-1}], t – is time [s], S – is cross-section of stick [mm2] and L – is length of stick [mm].

In publication (Baojun and Fazhong, 2002) was steady state heat conduction in one dimension described by the equation for a plane wall, shown in equation (4):

$$kA \frac{d^2T}{dx^2} = 0 \tag{4}$$

where k – is the thermal conductivity and a is the cross-sectional area perpendicular to the direction of heat flow. The problem is complete with following description of the boundary conditions: At $x = 0, T = T_1$, and at $x = L, T = T_2$,
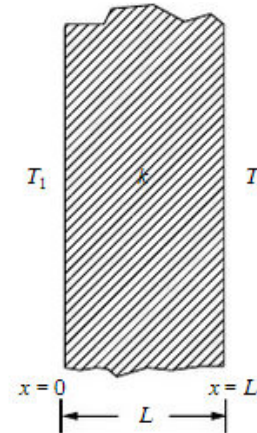

Fig. 4. Heat conduction through a homogenous wall

The exact solution to equation (4) is:

$$kAT = C_1 x + C_2 \tag{5}$$

On applying the appropriate boundary conditions to equation (5) we obtain:

$$C_2 = kAT_1 \tag{6}$$

$$C_1 = -\frac{kA(T_1 - T_2)}{L} \tag{7}$$

Therefore, substituting constants C1 and C2 into equation (5) results in:

$$T = -\frac{(T_1 - T_2)}{L} x + T_1 \tag{8}$$

The above equation indicates that the temperature distribution within the wall is linear. The heat flow, Q can be written as:

$$Q = -kA \frac{dT}{dx} = -\frac{kA}{L}(T_2 - T_1) \tag{9}$$

Above presented equations are the bases for a next complex heat and heat stress analysis of DMLS processes and post-processes and post-fabrication using simulation software's.

3. RESULTS

Material analysis was in this case realized with reason of; obtain the values of material composition, visualization of the surfaces, evaluation of microstructure, fracture surfaces and microhardness of samples. The surfaces of the samples were observed and documented with light microscopy and also scanning electron microscopy. Results from observing are shown in Fig. 5.
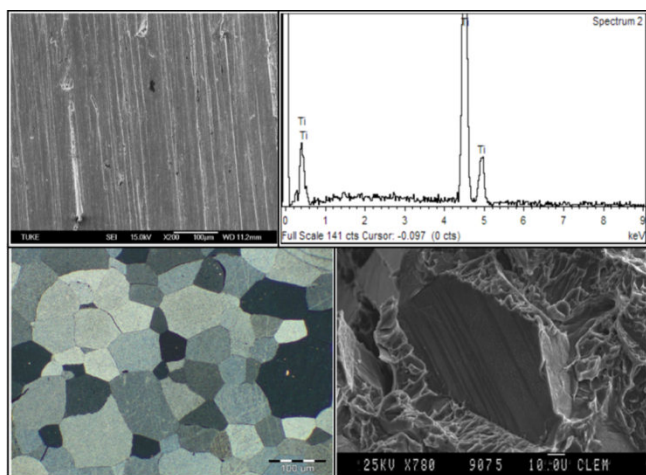
Fig. 5. Observation of the surface and EDX material analysis of Ti1
(up left and right), Microstructure of Ti1 (down left)
and Evaluation of surfaces fractures (down right)

Tab. 2. Result from microhardness (MH) measurement [HV0.05]

Sample	Average value of microhardness	Standard deviation of microhardness
Ti1	242.5	15.36229
Ti2	256.2	16.16663
Ti3	248.9	29.56078
Ti4	254.9	18.72538
Ti5	283.2	19.00947
Ti6	307	8.94427
Ti7	301.2	9.92773
Ti8	314.4	37.51053

On the prepared samples was performed observation and EDX analysis of the surface, observation of microstructure and fracture surfaces of the samples and measurement of microhardness. EDX analysis of the surface samples shows that samples of Ti1, Ti2, Ti3 and Ti4 consist of pure titanium. Any trace levels of contaminants is not possible, respectively is problematic to determine by EDX analysis.

EDX analysis of polished sections of samples Ti5, Ti6, Ti7 and Ti8 confirmed, that they contains from pure titanium. By EDX analysis of dull sections was found that in addition to titanium is in analysis the relatively high content of aluminum (Al), oxygen (O_2) and carbon (C). It can be assumed that at least part of the carbon and oxygen comes from pollution of samples, despite the fact that all samples were cleaned before observing in methanol and in ultrasonic cleaner. Despite the mixed results, which concerns the content of individual elements is necessary this EDX analysis perceive rather only as a qualitative and semi-qualitative than quantitative. Thus, the measured differences in contents of individual element, it is impossible to talk about the different surfaces of samples Ti5, Ti6, Ti7 and Ti8. From the findings show, that all samples are made of pure titanium, the surface of four of them (samples Ti5, Ti6, Ti7 and Ti8) is partially corundum blast.

The observation of the microstructure of the samples shows, that the structure of the sample Ti1, Ti2, Ti3 and Ti4 is quite heterogeneous and consists of polyhedral grains of size 20 to 150 microns. The structure of the samples Ti5, Ti6, Ti7 and Ti8 is relatively homogeneous and consists of polyhedral grains in size from 5 to 15 microns. In case of problematic preparation of

matallographic sections from titanium, not all documented microstructures were in sufficient quality. Grain size (GS) was not statistically recorded but only roughly compared.

On the samples was measured microhardness HV 0, 05. While for the samples Ti1, Ti2, Ti3 and Ti4 were average measured values in the range of 240 – 260 HV units, the samples Ti5, Ti6, Ti7 and Ti 8 were average measured values in the range of 295 – 315 HV units. The maximum standard deviation of microhardness measurement was 37.51053 HV. The results of microhardness measurements may have been more decisively influenced by different grain size, and thus area of impress considering the size of grain.

On Fig. 6. is possible to observe the first results of thermal simulation preformed with use of RadTherm software. It shows the simulation of stress relieving process after sintering process.
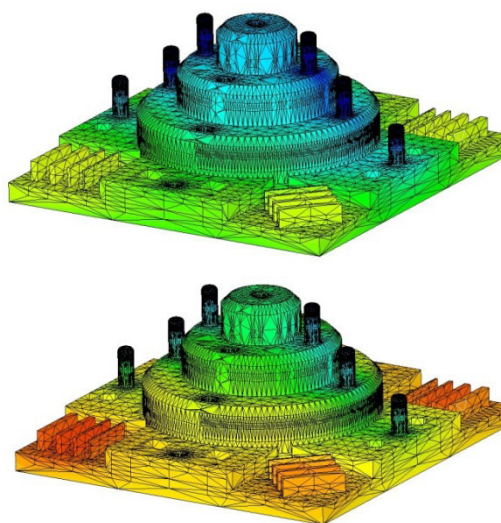
Fig. 6. The test sample during the stress relieving process simulation, the upper and lower sample with a gradual transition of heat from the edges to the center (core)

4. CONCLUSIONS

Presented paper shows results of two studies, analysis of the intraosseal dental implants from material and surface properties point of view and preparation of the methodology for thermal analysis of product during and after manufacturing process using DMLS technology.

Regarding to use of titanium alloys for biomedical applications, was prepared the material analysis, where were described and measured values of grain size and microhardness.

EDX analysis was performed for analyzing of comercially available implants, which are made from pure titanium (cp Ti) (Sidun and Dąbrowski, 2009).

In process of preparation is next study where will be analyzed outputs from DMLS technology (EOSINT M280, EOS Germany), but in the first case it will be necessary to perform analysis and simulation of heat processes and subsequently analyisis of dimensional circuits for detection of differences in term of residual heat stresses.

Attention was also taken to preparation of input parameters for heat and heat stress analysis. These input parameters must be prepared before the each research. It is only first phase

of planned studies. It defines the main issues and describes the technical aspects of DMLS and technology process of manufacturing the prototypes. In next research should be included fact that during the DMLS process all layers are not sintered homogeneously but in predefined laser beam pattern. To get exact parameters for heat analysis will be important to place of thermocamera in to the process chamber to get to full process thermography record. For next study the multi-layer building process will be considered where conduction of previous and next layer and influence of Ti64 powder bed will be included in calculations.

REFERENCES

1. **Baojun ZHAO, Fazhong Shi,** (2002), Modeling of Selective Laser Sintering for PC Powder, *Journal of Beijing University of Aeronautics and Astronautics*, Vol.28, No. 6, 660-663.
2. **Contuzzi,N.,Campanelli,S.L., et al.** (2011), 3D Finite element analysis in the selective laser melting process, *Int j simul model*, Vol. 10, No. 3, 113-121.
3. **Jiang Wei, Dalgarno K.W., et al.** (2002), *Finite Element Analysis of Residual Stresses and Deformations in Direct Metal SLS Process*, [cited on 2012-10-18] ,available at: http://edge.rit.edu/content/P10551/public/SFF/SFF%202002%20Proceedings/2002%20SFF%20Papers/38-Jiang.pdf
4. **Jiangui Li, Yusheng Shi, et al.** (2008), Numerical Simulation of Transient Temperature Field in Selective Laser Melting, *China Mechanical Engineering*, Vol 19, No. 20, 2492-2495.
5. **Kolossov S., Boillat E., et al.** (2004), 3D FE simulation for temperature evolution in the selective laser sintering process, *International Journal of Machine Tools and Manufacture*, Vol. 44, No. 2-3, 117-123.
6. **Kruth J.P., Wang X., et al.** (2003), Lasers and materials in selective laser sintering, *Assembly Automation*, Vol. 23, No. 4, 357 – 371.
7. **Kulesza E., Dabrowski J.R., Sidun J., Neyman A., Mizera J.** (2012) Fretting wear of materials – Methodological aspects of research, *Acta Mechanica et Automatica*, Vol. 6, No. 3, 58-61.
8. **Lewis R. W., et al.** (2004), *Fundamentals of the Finite Element Method for Heat and Fluid Flow*, Wiley, 356.
9. **Lienhard IV, H. J., Lienhard V, H. J.,** (2012), *A Heat Transfer Textbook, Fourth Edition*, Phlogiston PressCambridge, Massachusetts, U.S.A.
10. **Praslička D., Blažek J., Šmelko M., Hudák J., Čverha A., Mikita I., Varga R., Zhukov A.,** (2013), Possibilities of measuring stress and health monitoring in materials using contact-less sensor based on magnetic microwires, *IEEE Transactions on Magnetics*, 49 (1), art. no. 6392407, 128-131.
11. **RadTherm® Heat Transfer Analysis Software,** [cited on 2012-10-18], available at: http://www.thermoanalytics.com/products/radtherm
12. **Sidun J., Dąbrowski J.R.,** (2009), Bone ingrowth processes on porous metallic implants, Diffusion and Defect Data Pt.B: *Solid State Phenomena*, Volume 147-149, 776-781.
13. **Simchi A.** (2006), Direct laser sintering of metal powders: Mechanism, kinetics and microstructural features, *Materials Science and Engineering*: A 428, Vol. 1, No. 2, 148-158.
14. **SINTERING OF METALS.** [cited on 2012-10-18], available at: http://www.substech.com/dokuwiki/doku.php?id=sinteringofmetals
15. **Vozda M., Sekora M., Penhaker M.,** (2012), Precise Temperature Stabilizing System of Liquids for the Purpose Biomedical Alications, *Journal Electronics and Electrical Engineering*, Vol.18, No. 10, 29 – 32, Received 3rd MArch 2012, Accepted 12th May 2012; Published October 2012. ISSN 1392 – 1215 (print), ISSN 2029-5731.
16. **Wang X. C., Laoui T., et al.** (2002), Direct Selective Laser Sintering of Hard Metal Powders: Experimental Study and Simulation, *Int J Adv Manuf Technol*, Vol.19, 351–357.
17. **Zeng, K. Pal, D. Stucker, B.** (2012), *A review of thermal analysis methods in Laser Sintering and Selective Laser Melting*, [cited on 2012-10-18], available at: http://utwired.engr.utexas.edu/lff/symposium/proceedingsArchive/pubs/Manuscripts/2012/2012-60-Zeng.pdf
18. **Zhang D. Q., Cai Q. Z., et al.** (2010), Select laser melting of W–Ni–Fe powders: simulation and experimental study, The International Journal of Advanced Manufacturing Technology, Vol. 51, No. 5-8, 649-658.

THE EFFECT OF TEMPERATURE PYROLYSIS PROCESS OF USED TIRES ON THE QUALITY OF OUTPUT PRODUCTS

Natália JASMINSKÁ[*], Tomáš BRESTOVIČ[*], Mária ČARNOGURSKÁ[*]

[*]Faculty of Mechanical Engineering, Technical University in Kosice, Vysokoškolská 4, 042 00 Košice, Slovak Republik

natalia.jasminska@tuke.sk, tomas.brestovic@tuke.sk, maria.carnogurska@tuke.sk

Abstract: Pyrolysis together with gasification and combustion create a group of so called thermic processes. Unlike the combustion it is based on thermic decomposition of organic materials without any access of oxidative media. Within the pyrolytic process, three main fractions are created: solid residue, pyrolytic gas and organic liquid product – pyrolytic oil. The presented article examines the effects of pyrolysis operational conditions (above all, temperature) on gas products, solid residues and liquid fractions.

Key words: Pyrolysis, Pyrolysis, Used Tires, Temperature, Pyrolytic Gas, Pyrolytic Oil, Solid Residue

1. INTRODUCTION

Pyrolysis offers ecologically attractive method of decomposition and estimation of a wide scale of waste, including used tires. Processing of used tires by pyrolysis means their thermal degradation occurring without presence of oxygen. In the pyrolysis process organic volatiles from the tires (approximately 60 %) are decomposed into low molecular weight products, liquids or gases that could be subsequently used as fuels or chemicals (Wagnerová et al., 2003). Non-volatile soots and inorganic components (approximately 40 %) remain in the solid residue and can be recycled in different technological applications.

The benefit of this technology is a transformation of used tires to secondary raw materials such as olefins or active carbon. The biggest obstructions in wider usage of pyrolysis are high economical costs and technological demands of the process. The capital costs are too high in comparison with the value of pyrolysis output products. Development of less demanding technology or production of higher value products out of pyrolytic processes enable pyrolysis to become an equal alternative for recycling of used tires. The positives of this technology are low emission values in produced gas which means minimal negative effect on the environment (Aylón et al., 2007).

2. GENERAL CHARACTERISTICS OF THE PYROLYTIC PROCESS

Pyrolysis is a thermo-chemical distillation process within which heat is transported into a hermetically closed space filled with fuel. Here, hydrocarbons are fissured and formed to combustible gases, distillation products and carbonated residue (Cunliffe et al., 1998). Combustible gases and distillation products are subsequently used as, for example, fuel. The process is usually run in a so called pyrolytic furnace or also in a coking chamber. The process of pyrolysis is in progress at the temperature of 250 to 1 100 °C with prevention of air access. There is a gradual thermal decomposition where undesirable toxic matters are usually thermally decomposed into better modifiable matters or into harmless compounds. Frequently, compound of hydrocarbons and soots is gained. Within organic matters, it is mainly carbon dioxide (CO_2) and water. The liquid element of pyrolysis is called pyrolytic oil and the gas element is pyrolytic gas.

Recycling process by pyrolysis has two basic stages:

1. *Self pyrolysis*. It is a thermal decomposition of crushed input matters at high temperatures without air access.
2. *Pyrolytic product processing*. By pyrolytic oil separation it is possible to obtain secondary materials such as benzene, toluene, xylene and the like.

According to the temperature at which the pyrolytic process is run we distinguish:

− low-temperature pyrolysis (reaction temperature up to 500 °C),
− middle-temperature pyrolysis (reaction temperature in the range of 500 up to 800 °C),
− high-temperature pyrolysis (reaction temperature over 800 °C).

The own course of pyrolytic process lying in smaller molecules fission out of the original molecules with long chains depends on the type and characteristics of processed material (Muren et al., 1996).

Within the pyrolytic process there are, depending on temperature, different actions which can be, in a simplified way, divided into three thermal intervals.

1. Within temperatures up to 200 °C material is being dried and water steam is created – this is an endothermic process.
2. Within temperatures from 200 up to 500 °C there is a part of so called dry distillation. Here, side chains from the high-molecular organic matters are split off and macromolecular structures are transformed to gas and liquid organic products and to solid carbon.
3. In the phase of gas creation within temperatures from 500 up to 1 200 °C products that were created by a dry distillation are being fissioned and transformed. Pyrolytic gas, oils and charcoal are the primary products of this process (Tab. 1) (Rodriguez et al., 2001).

After pyrolysis, the solid residue contains soots and minerals. The liquid fraction is created by a very complicated composition of organic compounds.

Tab. 1. Products of pyrolysis process

Primary products	Weight %	Content	Secondary products
pyrolytic gas	10 – 30	H₂, CO₂, CO, methane, ethane, propane, propene, butane, other hydrocarbons, approximately 1 % of sulfur	-
pyrolytic oil	40 – 60	Low value of sulfur (0.3 – 0.1 %), aromatic hydrocarbons, alkanes, alkenes, ketones and aldehydes	soots (carbon slack)
charcoal	30 - 40	> 15 % of ash (containing ZnO), 3 – 5 % of sulfur.	active carbon

Oils and charcoal undergo other processes in order to gain more valuable products out of them. Improving qualities of charcoal is obtained by a multilevel activation with a final product of carbon with high active surface. Its other benefit is also elimination of undesirable side products and emissions. The oil with a low level of ash is transformed into high-quality soots or as an alternative, oil separation using distillation and their usage in chemical industry is an option. Gas product – pyrolytic gas is created by non-condensed organic elements and compounds H_2, H_2S, CO, CO_2, CH_4, C_2H_4, C_3H_6 and other light hydrocarbons. Subsequently, it is possible to use the pyrolytic gas as fuel in the process of pyrolysis. The volume and content of these three fractions depend on processing parameters (temperature, speed of heating, pressure, time, size and characteristics of the input material and so on), at volatile fraction, condensing temperature is a crucial parameter (Kizek et al., 1999).

Technologies that produce high-quality pyrolytic oil on the basis of fast pyrolysis have recently entered commercial levels. The main area of using the high-quality pyrolytic oil is biochemistry. Here, research of its usage is carried out – as an alternative fuel for slow-running ships and the like high-capacity diesel engines or combustion turbines.

2.1. Thermal decomposition of used tires

In order to study thermic degradation of tire rubber samples waste, standard methods are used:
– thermogravimetry (TG),
– derivative thermogravimetry (DTG).

Out of the thermogravimetric analysis listed according to different authors (e.g. Leung and Wang et al. 1998; Berrueco et al. 2005; Yang et al. 1995) it is clear that during pyrolysis there is more than one material decomposition influenced by temperature. It is confirmed also by experimental measurements that have been carried out (Fig. 1) (Koreňová et al., 2006; Haydara et al., 2012).

The result of decomposition influences mainly the composition of rubber compound. Measured thermogravimetric (TG) curves show two different weight losses in the temperature range from 250 to 550 °C. On the basis of the individual characteristics of tire rubber parts thermal decomposition in the temperature range of 250 up to 380 °C there is evaporation of additives, oil and softening agents. With the temperature interval of 400 up to 550 °C there is decomposition of natural rubber (NR), styrene-butadiene rubber (SBR) and polybutadiene rubber (BR).

A typical sample weight loss obtained within measurement is listed in the Fig. 2.
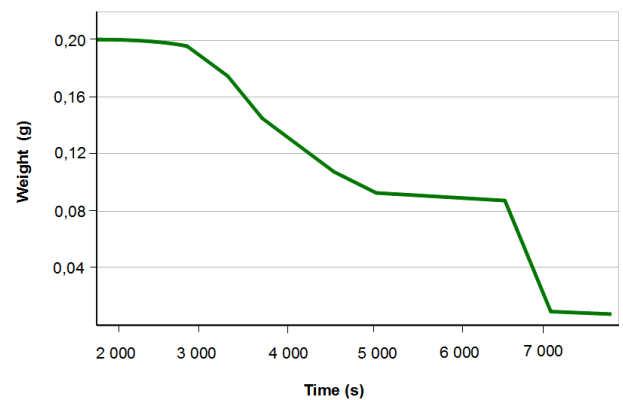

Fig. 1. Process of sample weight loss of the used tire depending on time
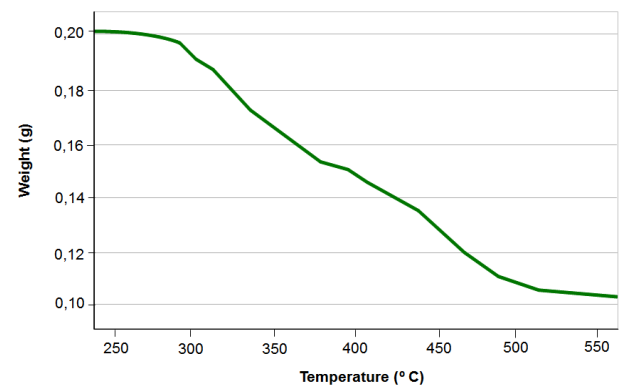

Fig. 2. Thermal degradation of the used tire residue

3. METHODOLOGY OF THE EXPERIMENT

Preparation of the sample lies in mechanical division of rubber, textile (polymer) and metal parts of the tire. The rubber part of the tire is inserted into a shredder where its size is reduced to approximately 15 cm big parts.

In the experimental research of pyrolytic process of used tires liquidation, rubber grit from used tires of cars and trucks was used (sample marked RR) as well as polymer fibers, gained at tire mechanical modification (sample marked PF).

At the thermic degradation of used tires, it is crucial to know the combustion heat of the particular material and its calorific value. Before the test of pyrolytic process of decomposition there were calorimetric measurements carried out in order to set combustion heat for each tire sample individually. The final value represents an average value out of the three calorimetric measurements. For the purpose of control of the laboratory results at the department, an elemental analysis in external laboratory was carried out. Elemental analysis of laboratory tests samples carried out at the department is listed in Tab. 2.

Tab. 2. Elemental analysis of used tires rubber grit

Sample	C^d	H^d	N^d	S^d	O^d	Ash^d	Q_s^*
	(% weight)						(MJ·kg⁻¹)
RR	87.6	7.6	0.3	2.01	3.1	9.3	36.75
PF	83.6	7.2	0.3	1.75	7.8	8.4	32.89

Values of the individual elements gained in the elemental analysis (Cd-carbon, Hd-hydrogen, Nd-nitrogen, Sd-sulfur, Od- oxygen), Q_s^* - combustion heat gained in calorimetric measurement

3.1. Experimental device

In order to propose the experimental device for monitoring the pyrolysis process it is necessary to consider operational conditions of the technological pyrolysis process and technical solution of the experimental device:

1. Conditions of pyrolysis process:
   – non-oxidative environment,
   – type of reaction chamber,
   – material heating up (speed of heating up).
2. Conditions of technical solution
   – material quantization,
   – collection of pyrolytic products (solid residues, liquid fraction, gas compound).

From the above mentioned conditions for the process of py-

rolysis it is necessary to provide that the experimental sample is in a non-oxidative atmosphere. For creating a non-oxidative atmosphere it is possible to use inert gas (nitrogen) with the purity of 99.9 % which is suitable to use due to its characteristics. The choice of using nitrogen in order to create a non-oxidative atmosphere has already been confirmed in various works from the area of pyrolytic process laboratory research. Nitrogen is delivered into the reaction chamber from a pressure vessel. Thermal energy needed for a thermal decomposition is gained from electric resistance heating. At experimental conditions, a continuous operation is not considered and it is the reason for the construction of reactor with stationary horizontal bed containing SiC-rod with a diameter of 30 mm and length of 600 mm. The scheme of experimental pyrolytic device is shown in the Fig. 3. The device is located in the laboratory at the Department of Power Engineering.
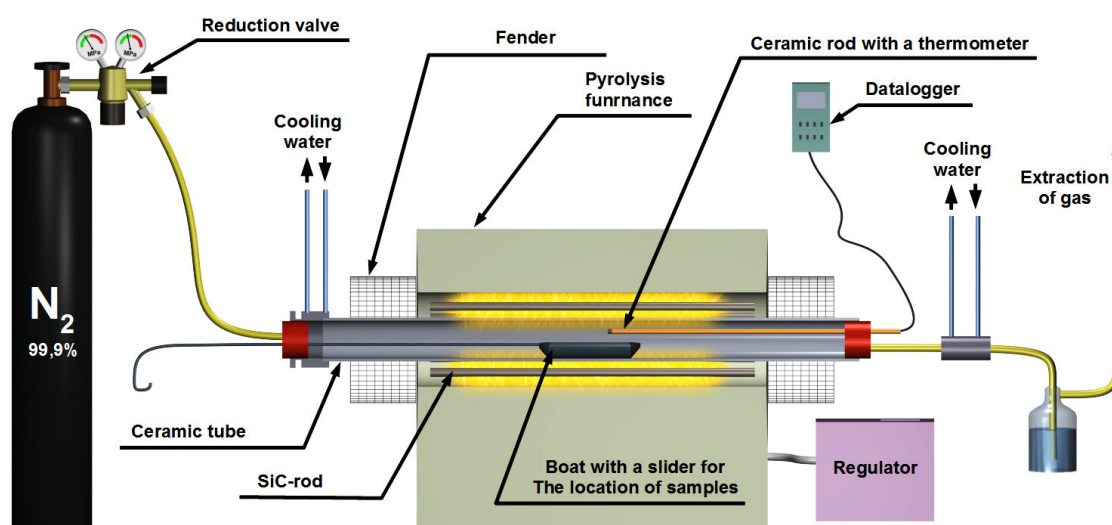

Fig. 3. The scheme of laboratory pyrolytic device

The procedure at the experiment is following:
– measured waste sample is inserted into a dosing device and it is placed into the entrance chamber of the device,
– cooling system of the entrance chamber is on and its sealing is determined,
– after controlling the sealing, all system is rinsed by nitrogen from a pressure device which enables to create working non-oxidative environment,
– it is necessary to carry out the rinsing for approximately 10 minutes which is a proper time for eliminating atmospheric air that entered the system after locating the sample into the entrance chamber,
– the flow of nitrogen is stopped by a closing valve,
– a three-way valve serves for connecting the U-tube with all system of the experimental device (U-tube serves for the sealing control of all system). Change in pressure means no sealing in the system,
– after setting the sealing, heating of reactor's reaction zone is turned on. It consists of inner part of silica tube. Heating is provided by a resistance furnace. The furnace heating is regulated by a TC-31 regulator and temperature in the reaction furnace zone is controlled by a thermocouple type S with an output for a digital thermometer Testo 945. Time interval of temperature registering is selectable. In case of this experi-

ment, it was 1 minute. Also temperature of furnace's surface is registered using contact thermometer with an output for AL-MEMO 2290.
– after heating the furnace and after temperatures' consolidation in the reaction zone, it is possible to start to monitor the pyrolysis process,
– before placing the sample into the reaction zone, the three-way valve was turned to a position of flow of created gas to graduated bottle, thus the U-tube was disconnected from all of the system.

Monitoring of the pyrolytic process was carried out by three different manners. The first manner represented so called "fast pyrolysis". Here, the sample was heated to the temperature of 600 °C at the heating speed of 10 °C·min^{-1}. In the second manner, sample heating was carried out by a so called "fast pyrolysis" to the temperature of 800 °C. In the third manner the sample was heated by a "fast pyrolysis" to 600 °C and then by a "slow pyrolysis" to 800 °C at heating speed of 2 °C·min^{-1}.

Out of the produced pyrolytic gas, a condensate is captured in the gas cooler and gas in the graduated bottle and also its volume is registered. Gas volume is registered at its production which starts at a temperature range of 200 up to 250 °C.

Time interval of volume registering was 1 minute – until the furnace was turned off. In order to avoid distortion of real pyrolytic

gas composition, all devices is rinsed by nitrogen in volume of 1.0 to 1.3 l after the process is finished. Nitrogen enables to capture the gas product that remained in the reaction zone. Rinsing is carried out until the furnace temperature in the reaction zone decreases below 200 °C. After opening the entrance chamber, a sample of solid residue is taken; it is measured on analytical scales and prepared for the analysis.

Results of the analysis are listed in Tab. 3. At the chromatographic analysis, there was a slight number of oxygen registered in gas products.

The oxygen must have entered the sample only at its removal from the device. If we consider the pyrolytic process, it is not possible that the created pyrolytic gas contained oxygen because oxygen in waste is used at reactions in the reaction zone for creating CO, CO_2 and liquid fractions of pyrolysis. This oxygen influences the real composition of pyrolytic gas therefore at processing the results it was deducted from the total volume. Also, it is necessary to deduct nitrogen out of the total volume because it formed a part of the absorbed air and it was creating inert atmosphere in the pyrolytic furnace.

Tab. 3. Chromatographic analysis of the pyrolytic process gas product for the RR and PF sample

Chromatographic analysis of the pyrolytic process gas product						
	RR sample			PF sample		
	temperature			temperature		
Content (%)	600 °C	600 – 800 °C	800 °C	600 °C	600 – 800 °C	800 °C
CH_4	7.12	8.63	9.40	6.12	7.52	8.69
H_2	6.95	12.31	18.1	5.41	8.65	11.41
O_2	0.14	0.11	0.09	0.38	0.035	0.34
N_2	79.1	75.2	65.8	73.4	71.2	69.3
CO_2	0.18	0.19	0.21	0.95	0.35	0.21
CO	0.38	0.65	0.82	0.01	0.20	0.63
C_2H_4	5.33	6.80	4.48	3.15	1.89	0.98
C_2H_6	0.20	0.48	0.56	0.15	0.056	0.027
C_2H_2	0.29	0.36	0.89	0.33	0.27	0.45
C_{5-8}	0.30	0.30	0.29	0.087	0.04	0.055
C_4	0.59	0.62	0.39	0.044	0.39	0.017
C_3	0.71	0.97	0.52	0.065	0.293	0.016
Q_i (MJ·Nm^{-3})	37.14	38.15	39.60	33.26	35.41	36.15

4. DISCUSSION

In the article, only influence of temperature on the process of pyrolysis for used tires liquidation is analyzed.

The loss in weight of the original sample as opposed to the weight of the original sample that represents weight conversion to liquid and gas products is shown in the Fig. 4.
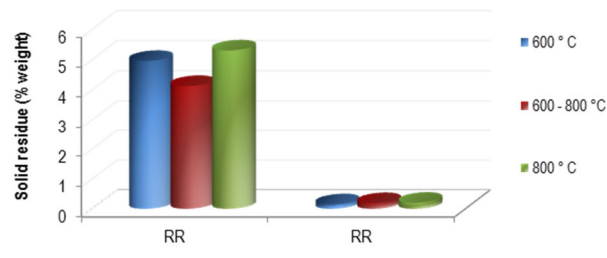

Fig. 4. Original sample conversion

The biggest conversion of weight into liquid and gas products is at 800 °C. The conversion is mainly influenced by the manner of pyrolysis, i.e. if it is a slow or fast pyrolysis. In case of the carried out research it is monitoring of the heating speed influence. The next factor influencing conversion is chemical purity of the material being liquidated by pyrolysis. High value of conversion is important at waste removal because the effort is to significantly

reduce the weight of waste. Weight division into the individual products in % as opposed to the original sample weight is shown in Fig. 5.
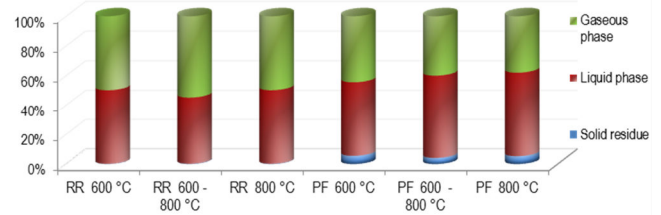
Fig. 5. Tire sample division to individual products

From the graphic scheme it is clear that at fast pyrolysis (at thermal interval of 600 up to 800 °C) the share of gas product is in average 55 %. Within combined pyrolysis it is clearly confirmed that there is the biggest share of gas product as towards the pyrolysis at constant temperature.

Considering the results of pyrolytic process and creation of pyrolytic products it is possible to state that using this technology there is a precondition of continuous energetic usage of mainly gas products – products with the biggest weight share. Volume of the created gas product, registered at the end of the measurement and counted considering 1 g of sample weight is shown in Fig. 6. Volume of the created pyrolytic gas increases with increased temperature in the interval of 600 to 800 °C. There is a precondition that the volume of created gas product depends on the volume of volatile combustible. However, clear confirmation of this hypothesis is not possible due to the fact that the volume of volatile combustible was not examined before the laboratory test.
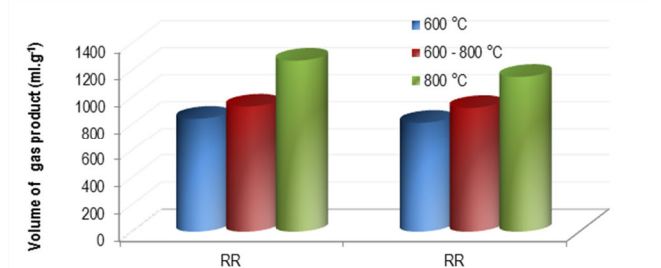
Fig. 6. Volume of created gas product
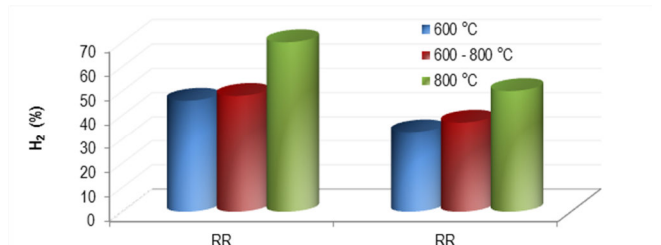
Fig. 7. Creation of hydrogen under the influence of temperature

In response to the creation of gas product it is important to monitor the share of combustible and non-combustible elements of pyrolytic gas. Out of their quantitative share at concrete temperatures of the pyrolytic process it is possible to set the

temperature influence to their creation. Content of the individual elements (H_2, CO, CO_2, CH_4, C_2H_4) depending on temperature is shown in Figs. 7 to 11. It is clear from the Fig. 8 that with increased temperature also volume of H_2 increases and volume of carbohydrates CH_4 decreases.
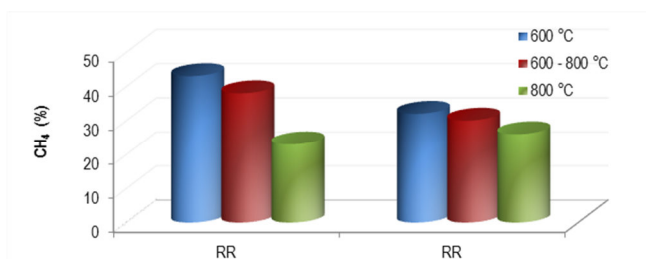

Fig. 8. Creation of methane influenced by temperature

Due to the fact that methane has higher thermal capacity than hydrogen, it is necessary to consider it for usage of the gas product. In case the gas product is to be used from the point of view of its heating characteristics, it is more convenient to use the pyrolytic gas product being created at 600 °C which is richer in methane, but at creation of less volume of this gas. In case the highest volume possible is to be obtained at the lowest solid residue, it is necessary to apply pyrolysis at 800 °C.
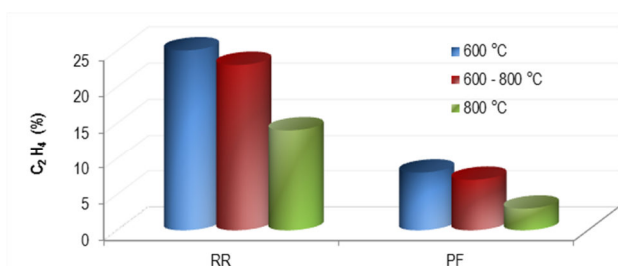

Fig. 9. Creation of ethylene influenced by temperature

The influence of temperature for ethylene creation has the same effect as within methane. That means higher volume share of ethylene is registered at temperature of 600 °C. The value of CO does not significantly changes with temperature (Fig. 10). Influence of increasing temperature to creation of CO is not as significant as within hydrogen or methane. The value of CO as well as CO_2 (Fig. 11) depends on the volume of oxygen in the original sample.
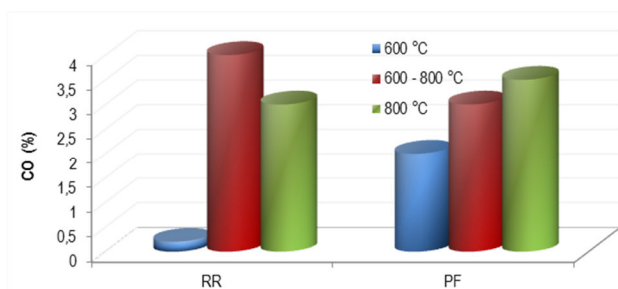

Fig. 10. Creation of carbon monoxide influenced by temperature

Used tires do not have clear chemical structure and they contain some volume of oxygen in various additives.
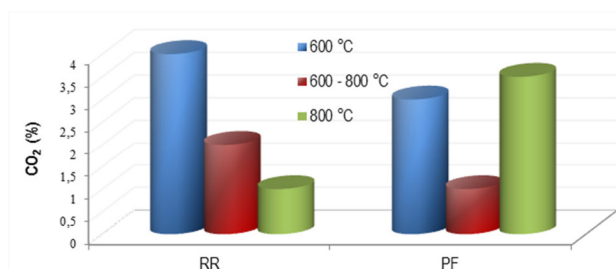

Fig. 11. Creation of carbon dioxide influenced by temperature

5. CONCLUSION

At present, many methods of pyrolytic processes are known and they significantly differ from each other in period of time of keeping the material in pyrolytic reactor, in temperature at which there is combustion created, in volume of created heat and also in created products of pyrolysis.

Current manners of used tires liquidation are not suitable mainly from the point of view of environment protection. Pyrolysis seems to be one of the possible solutions of minimizing the permanently increasing waste; within this technology also with a significant economic effect.

Using pyrolysis as a method of energetic recovery of used tires depends on sales of the pyrolytic products. Therefore, characteristics of the pyrolytic products and possibilities of their further application in technological processes are important. Currently, mainly solid products of pyrolysis are used, such as active carbon or solid residues are used in reinforcements in rubber industry. Liquid pyrolytic products are used as fuel or source of chemical matters and pyrolytic gas is re-used for pyrolytic process. temperature (above all, chosen thermal interval of pyrolytic process duration) and heating speed of the liquidated sample.

The aim of this work was to draw attention to the influence of operational parameters on final products of the pyrolytic process. As it results from the experiment, the most significant parameter that influences the final products of pyrolysis is temperature (above all, chosen thermal interval of pyrolytic process duration) and heating speed of the liquidated sample.

REFERENCES

1. **Aylón E. et al.** (2007), Emissions from the combustion of gas-phase products at tyre pyrolysis, *Journal of Analytical and Applied Pyrolysis*, 79, 210-214.
2. **Berrueco C., Esperanza E., Mastral F. J. et al.** (2005), Pyrolysis of waste tyres in an atmospheric static-bed batch reactor, Analysis of the gases obtained, *Journal of Analytical and Applied Pyrolysis*, 74, 245-253.
3. **Cunliffe A. M., Williams P. T.** (1998), Composition of oils derived from the batch pyrolysis of tyres, *Journal of Analytical and Applied Pyrolysis*, 44, 131-152.
4. **Haydary J. et al.** (2012), Influence of particle size and kinetic parameters on tire pyrolysis, *Journal of Analytical and Applied Pyrolysis*, 97, 73-79.
5. **Kizek J., Zsigraiová Z.** (1999), Experimental study of combustion parameters of low-heat gaseous fuels, *Metallurgičeskaja*

Teplotechnika, Gosudarstvennaja Metalurgičeskaja Akademija Ukrajiny, 17-19.

6. **Koreňová Z. et al.** (2006), Kinetics of Pyrolysis and properties of Carbon Black from a Scrap Tire, *Chemical Paper*, 60, 422-426.

7. **Leung D. Y. C., Wang C. L.** (1998), Kinetic study of scrap tyre pyrolysis and combustion, *Journal of Analytical and Applied Pyrolysis*, 45, 153-169.

8. **Murena F., Garufi E., Smith R.B., Gioia F.** (1996), Hydrogenative pyrolysis of waste tires, *Journal of Hazardous Materials*, 50, 79-98.

9. **Rodriguez I. M., et al.** (2001), Pyrolysis of scrap tyres, *Fuel Processing Technology*, 72, 9-22.

10. **Wágnerová E., Uríček D.** (2003), Theoretical analysis of thermal methods of disposal of municipal waste, *Acta Mechanica Slovaca*, 7, 337-342.

11. **Yang J., Tanguy P. A., Roy C.** (1995), Heat transfer, mass transfer and kinetics study of the vacuum pyrolysis of a large used tire particle, *Chemical Engineering Science*, 50, 1909-1922.

SINGULAR FRACTIONAL CONTINUOUS-TIME AND DISCRETE-TIME LINEAR SYSTEMS

Tadeusz KACZOREK*

*Faculty of Electrical Engineering, Białystok University of Technology, ul. Wiejska 45D, 15-351 Białystok, Poland

kaczorek@isep.pw.edu.pl

Abstract: New classes of singular fractional continuous-time and discrete-time linear systems are introduced. Electrical circuits are example of singular fractional continuous-time systems. Using the Caputo definition of the fractional derivative, the Weierstrass regular pencil decomposition and Laplace transformation the solution to the state equation of singular fractional linear systems is derived. It is shown that every electrical circuit is a singular fractional systems if it contains at least one mesh consisting of branches with only ideal supercondensators and voltage sources or at least one node with branches with supercoils. Using the Weierstrass regular pencil decomposition the solution to the state equation of singular fractional discrete-time linear systems is derived. The considerations are illustrated by numerical examples.

Keywords: Fractional, Singular, Linear Circuit, Regular Pencil, Solution, Supercondensator, Supercoil

1. INTRODUCTION

Singular (descriptor) linear systems have been addressed in many papers and books (Benvenuti and Farina, 2004; Dodog and Stosic, 2009; Dail, 1989; Kaczorek, 1992, 2004, 2008, 2010, 2011; Podlubny, 1999). The eigenvalues and invariants assignment by state and output feedbacks have been investigated in Benvenuti and Farina (2004), Dodog and Stosic (2009), Dail, (1989), Kaczorek (2004, 2008) and the realization problem for singular positive continuous-time systems with delays in Kaczorek (2010). The computation of Kronecker's canonical form of a singular pencil has been analyzed in Podlubny (1999).

Fractional positive continuous-time linear systems have been addressed in Kaczorek (2010) and positive linear systems with different fractional orders in Kaczorek (2007). An analysis of fractional linear electrical circuits has been presented in Gantmacher (1960) and some selected problems in theory of fractional linear systems in the monograph Kaczorek (2007).

In this paper a new class of singular fractional linear systems and electrical circuits will be introduced and their solution of state equations will be derived.

The paper is organized as follows. In section 2 the Caputo definition of the fractional derivative and the solution to the state equation of the fractional linear system are recalled. The solution of the state equation of singular fractional linear system is derived using the Weierstrass pencil decomposition and the Laplace transform in Section 3. Singular fractional linear electrical circuits are introduced in Section 4. In section 5 the fractional singular discrete-time linear systems are introduced and Weierstrass regular pencil decomposition is recalled. The solution of the state equation of singular fractional linear discrete-time system is derived using the Weierstrass pencil decomposition in Section 6. Illustrating numerical examples are given in Section 7. Concluding remarks are given in Section 8.

To the best of the author's knowledge singular fractional linear systems and electrical circuits have not been considered yet.

The following notation will be used in the paper.

The set of $n \times m$ real matrices will be denoted by $\Re^{n \times m}$ and $\Re^n := \Re^{n \times 1}$. The set of $m \times n$ real matrices with nonnegative entries will be denoted by $\Re_+^{m \times n}$ and $\Re_+^n := \Re_+^{n \times 1}$. The set of nonnegative integers will be denoted by Z_+ and the $n \times n$ identity matrix by I_n.

2. FRACTIONAL CONTINUOUS-TIME LINEAR SYSTEMS

The following Caputo definition of the fractional derivative will be used (Kaczorek, 2007; Kucera and Zagalak, 1988):

$$\frac{d^\alpha}{dt^\alpha} f(t) = \frac{1}{\Gamma(n-\alpha)} \int_0^t \frac{f^{(n)}}{(t-\tau)^{\alpha+1-n}} d\tau, \tag{2.1}$$

$$n-1 < \alpha \le n \in N = \{1,2,...\}$$

where $\alpha \in \Re$ is the order of fractional derivative, $f^n(\tau) = \frac{d^n f(\tau)}{d\tau^n}$ and $\Gamma(x) = \int_0^\infty e^{-t} t^{x-1} dt$ is the gamma function.

Consider the continuous-time fractional linear system described by the state equation:

$$\frac{d^\alpha}{dt^\alpha} x(t) = Ax(t) + Bu(t), \;\; 0 < \alpha \le 1 \tag{2.2}$$

where $x(t) \in \Re^n$, $u(t) \in \Re^m$ are the state and input vectors and $A \in \Re^{n \times n}, B \in \Re^{n \times m}$.

Theorem 2.1. The solution of equation (2.2) is given by:

$$x(t) = \Phi_0(t)x_0 + \int_0^t \Phi(t-\tau)Bu(\tau)d\tau, \;\; x(0) = x_0 \tag{2.3}$$

where:

$$\Phi_0(t) = \sum_{k=0}^{\infty} \frac{A^k t^{k\alpha}}{\Gamma(k\alpha+1)} \tag{2.4}$$

$$\Phi(t) = \sum_{k=0}^{\infty} \frac{A^k t^{(k+1)\alpha-1}}{\Gamma[(k+1)\alpha]} \tag{2.5}$$

Proof is given in Kaczorek (2010a, b).

Remark 2.1. From (2.4) and (2.5) for $\alpha = 1$ we have:

$$\Phi_0(t) = \Phi(t) = \sum_{k=0}^{\infty} \frac{(At)^k}{\Gamma(k+1)} = e^{At} .$$

3. SINGULAR FRACTIONAL CONTINUOUS-TIME LINEAR SYSTEMS

Consider singular fractional linear system described by the state equations:

$$E \frac{d^\alpha}{dt^\alpha} x(t) = Ax(t) + Bu(t) \tag{3.1a}$$

$$y(t) = Cx(t) + Du(t) \tag{3.1b}$$

where $x(t) \in \mathfrak{R}^n$, $u(t) \in \mathfrak{R}^m$, $y(t) \in \mathfrak{R}^p$ are the state, input and output vectors and $E, A \in \mathfrak{R}^{n\times n}$, $B \in \mathfrak{R}^{n\times m}$, $C \in \mathfrak{R}^{p\times n}$, $D \in \mathfrak{R}^{p\times m}$.

The initial condition for (3.1a) is given by:

$$x(0) = x_0 \tag{3.1c}$$

It is assumed that the pencil of the pair (*E*, *A*) is regular, i.e.

$$\det[Es - A] \neq 0 \tag{3.2}$$

for some $z \in C$ (the field of complex numbers). It is well-known (Fahmy and O'reill, 1989; Kaczorek, 1992)) that if the pencil is regular then there exists a pair of nonsingular matrices $P, Q \in \mathfrak{R}^{n\times n}$ such that:

$$P[Es - A]Q = \begin{bmatrix} I_{n_1} & 0 \\ 0 & N \end{bmatrix} s - \begin{bmatrix} A_1 & 0 \\ 0 & I_{n_2} \end{bmatrix} \tag{3.3}$$

where: n_1 is equal to degree of the polynomial $\det[Es - A]$, $A_1 \in \mathfrak{R}^{n_1 \times n_1}$, $N \in \mathfrak{R}^{n_2 \times n_2}$ is a nilpotent matrix with the index μ (i.e. $N^\mu = 0$ and $N^{\mu-1} \neq 0$ and $n_1 + n_2 = n$).

Applying to the equation (3.1a) with zero initial conditions $x_0 = 0$ the Laplace transform ($\mathcal{L}$) we obtain:

$$[Es^\alpha - A]X(s) = BU(s) \tag{3.4}$$

where $X(s) = \mathcal{L}[x(t)] = \int_0^\infty x(t)e^{-st}dt$ and $U(s) = \mathcal{L}[u(t)]$. By assumption (3.2) the pencil $[Es^\alpha - A]$ is regular and we may apply the decomposition (3.3) to equation (3.1a).

Premultiplying the equation (3.1a) by the matrix $P \in \mathfrak{R}^{n\times n}$ and introducing the new state vector:

$$\bar{x}(t) = Q^{-1}x(t) = \begin{bmatrix} x_1(t) \\ x_2(t) \end{bmatrix}, \ x_1(t) \in \mathfrak{R}^{n_1}, \ x_2(t) \in \mathfrak{R}^{n_2} \tag{3.5}$$

we obtain:

$$\frac{d^\alpha}{dt^\alpha} x_1(t) = A_1 x_1(t) + B_1 u(t) \tag{3.6a}$$

$$N \frac{d^\alpha}{dt^\alpha} x_2(t) = x_2(t) + B_2 u(t) \tag{3.6b}$$

where:

$$PB = \begin{bmatrix} B_1 \\ B_2 \end{bmatrix}, \ B_1 \in \mathfrak{R}^{n_1 \times m}, \ B_2 \in \mathfrak{R}^{n_2 \times m} \tag{3.6c}$$

Using (2.3) we obtain the solution to the equation (3.6a) in the form:

$$x_1(t) = \Phi_{10}(t)x_{10} + \int_0^t \Phi_{11}(t-\tau)B_1u(\tau)d\tau \tag{3.7a}$$

where:

$$\Phi_{10}(t) = \sum_{k=0}^{\infty} \frac{A_1^k t^{k\alpha}}{\Gamma(k\alpha+1)} \tag{3.7b}$$

$$\Phi_{11}(t) = \sum_{k=0}^{\infty} \frac{A_1^k t^{(k+1)\alpha-1}}{\Gamma[(k+1)\alpha]} \tag{3.7c}$$

and $x_{10} \in \mathfrak{R}^{n_1}$ is the initial condition for (3.6a) defined by:

$$\begin{bmatrix} x_{10} \\ x_{20} \end{bmatrix} = Q^{-1}x_0 , \ x_0 = x(0) \tag{3.7d}$$

To find the solution of the equation (3.6b) we apply to the equation the Laplace transform and we obtain:

$$Ns^\alpha X_2(s) - Ns^{\alpha-1}x_{20} = X_2(s) + B_2U(s) \tag{3.8a}$$

Since Kaczorek (2010a) and (Dodog and Stosic, 2009) for $0 < \alpha < 1$

$$\mathcal{L}\left[\frac{d^\alpha}{dt^\alpha} x_2(t)\right] = s^\alpha X_2(s) - s^{\alpha-1}x_{20} \tag{3.8b}$$

where $X_2(s) = \mathcal{L}[x_2(t)]$. From (3.8) we have:

$$X_2(s) = [Ns^\alpha - I_{n_2}]^{-1}(B_2U(s) + Ns^{\alpha-1}x_{20}) \tag{3.9}$$

It is easy to check that:

$$[Ns^\alpha - I_{n_2}]^{-1} = -\sum_{i=0}^{\mu-1} N^i s^{i\alpha} \tag{3.10}$$

since:

$$[Ns^\alpha - I_{n_2}]\left(-\sum_{i=0}^{\mu-1} N^i s^{i\alpha}\right) = I_{n_2} \tag{3.11}$$

and $N^i = 0$ for $i = \mu, \mu+1, \ldots$

Substitution of (3.10) into (3.9) yields:

$$X_2(s) = -B_2 U(s) - \frac{N x_{20}}{s^{1-\alpha}}$$

$$- \sum_{i=1}^{\mu-1} \left[N^i B_2 s^{i\alpha} U(s) + N^{i+1} s^{(i+1)\alpha-1} x_{20} \right] \quad (3.12)$$

Using inverse Laplace transform ($\mathcal{L}^{-1}$) to (3.12) and the convolution theorem we obtain for $1 - \alpha > 0$:

$$x_2(t) = \mathcal{L}^{-1}[X_2(s)] = -B_2 u(t) - N x_{20} \frac{t^{-\alpha}}{\Gamma(1-\alpha)}$$

$$- \sum_{i=1}^{\mu-1} \left[N^i B_2 \frac{d^{i\alpha}}{dt^{i\alpha}} u(t) + N^{i+1} \frac{d^{(i+1)\alpha-1}}{dt^{(i+1)\alpha-1}} x_{20} \right] \quad (3.13)$$

since $\mathcal{L}^{-1}\left[\dfrac{1}{s^{\alpha+1}} \right] = \dfrac{t^\alpha}{\Gamma(1+\alpha)}$ for $\alpha + 1 > 0$.

Therefore, The following theorem has been proved.

Theorem 3.1. The solution to the equation (3.1a) with the initial condition (3.1c) has the form

$$x(t) = Q \begin{bmatrix} x_1(t) \\ x_2(t) \end{bmatrix} \quad (3.14)$$

where $x_1(t)$ and $x_2(t)$ are given by (3.7) and (3.13) respectively. Knowing the solution (3.14) we can find the output $y(t)$ of the system using the formula

$$y(t) = CQ \begin{bmatrix} x_1(t) \\ x_2(t) \end{bmatrix} + Du(t) \quad (3.15)$$

4. SINGULAR FRACTIONAL ELECTRICAL CIRCUITS

Let the current $i_C(t)$ in the supercondensator with the capacity C be the α order derivative of its charge $q(t)$ (Gantmacher, 1960):

$$i_C(t) = \frac{d^\alpha q(t)}{dt^\alpha} \quad (4.1)$$

Taking into account that $q(t) = Cu_C(t)$ we obtain:

$$i_C(t) = C \frac{d^\alpha u_C(t)}{dt^\alpha} \quad (4.2)$$

where $u_C(t)$ is the voltage on the supercondensator.

Similarly, let the voltage $u_L(t)$ on the supercoil (inductor) with the inductance L be the β order derivative of its magnetic flux $\psi(t)$:

$$u_L(t) = \frac{d^\beta \Psi(t)}{dt^\beta} \quad (4.3)$$

Taking into account that $\psi(t) = Li_L(t)$ we obtain

$$u_L(t) = L \frac{d^\beta i_L(t)}{dt^\beta} \quad (4.4)$$

where $i_L(t)$ is the current in the supercoil.

Example 4.1. Consider electrical circuit shown in Fig. 1 with given resistance R, capacitances C_1, C_2, C_3 and source voltages e_1 and e_2.

Using the Kirchhoff's laws we can write for the electrical circuit the equations:

$$e_1 = RC_1 \frac{d^\alpha u_1}{dt^\alpha} + u_1 + u_3$$

$$C_1 \frac{d^\alpha u_1}{dt^\alpha} + C_2 \frac{d^\alpha u_2}{dt^\alpha} - C_3 \frac{d^\alpha u_3}{dt^\alpha} = 0 \quad (4.5)$$

$$e_2 = u_2 + u_3$$

The equations (4.5) can be written in the form:

$$\begin{bmatrix} RC_1 & 0 & 0 \\ C_1 & C_2 & -C_3 \\ 0 & 0 & 0 \end{bmatrix} \frac{d^\alpha}{dt^\alpha} \begin{bmatrix} u_1 \\ u_2 \\ u_3 \end{bmatrix} = \begin{bmatrix} -1 & 0 & -1 \\ 0 & 0 & 0 \\ 0 & -1 & -1 \end{bmatrix} \begin{bmatrix} u_1 \\ u_2 \\ u_3 \end{bmatrix}$$

$$+ \begin{bmatrix} 1 & 0 \\ 0 & 0 \\ 0 & 1 \end{bmatrix} \begin{bmatrix} e_1 \\ e_2 \end{bmatrix}$$

$$(4.6)$$

In this case we have:

$$E = \begin{bmatrix} RC_1 & 0 & 0 \\ C_1 & C_2 & -C_3 \\ 0 & 0 & 0 \end{bmatrix}, \quad A = \begin{bmatrix} -1 & 0 & -1 \\ 0 & 0 & 0 \\ 0 & -1 & -1 \end{bmatrix}, \quad B = \begin{bmatrix} 1 & 0 \\ 0 & 0 \\ 0 & 1 \end{bmatrix} \quad (4.7)$$

Note that the matrix E is singular ($\det E = 0$) but the pencil:

$$\det[Es^\alpha - A] = \begin{vmatrix} RC_1 s^\alpha + 1 & 0 & 1 \\ C_1 s^\alpha & C_2 s^\alpha & -C_3 s^\alpha \\ 0 & 1 & 1 \end{vmatrix} \quad (4.8)$$

$$= (RC_1 s^\alpha + 1)(C_2 + C_3) s^\alpha + C_1 s^\alpha$$

is regular. Therefore, the electrical circuit is a singular fractional linear system.
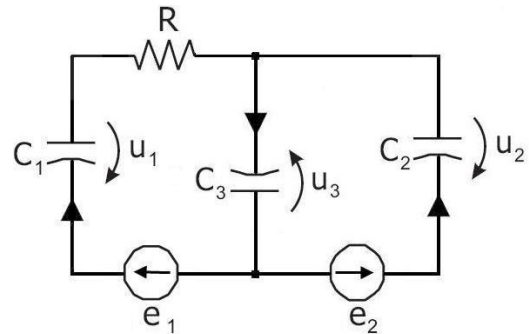
Fig.1. Electrical circuit

Remark 4.1. If the electrical circuit contains at least one mesh consisting of branches with only ideal supercondensators and voltage sources then its matrix E is singular since the row corresponding to this mesh is zero row. This follows from the fact that the equation written by the use of the voltage Kirchhoff's law is algebraic one.

Example 4.2. Consider electrical circuit shown in Fig. 2 with given resistances R_1, R_2, R_3 inductances L_1, L_2, L_3 and source voltages e_1 and e_2.

Using the Kirchhoff's laws we can write for the electrical circuit the equations:

$$e_1 = R_1 i_1 + L_1 \frac{d^\beta i_1}{dt^\beta} + R_3 i_3 + L_3 \frac{d^\beta i_3}{dt^\beta}$$

$$e_2 = R_2 i_2 + L_2 \frac{d^\beta i_2}{dt^\beta} + R_3 i_3 + L_3 \frac{d^\beta i_3}{dt^\beta} \qquad (4.9)$$

$$i_1 + i_2 - i_3 = 0$$

The equations (4.9) can be written in the form:

$$\begin{bmatrix} L_1 & 0 & L_3 \\ 0 & L_2 & L_3 \\ 0 & 0 & 0 \end{bmatrix} \frac{d^\beta}{dt^\beta} \begin{bmatrix} i_1 \\ i_2 \\ i_3 \end{bmatrix} = \begin{bmatrix} -R_1 & 0 & -R_3 \\ 0 & -R_2 & -R_3 \\ 1 & 1 & -1 \end{bmatrix} \begin{bmatrix} i_1 \\ i_2 \\ i_3 \end{bmatrix}$$

$$+ \begin{bmatrix} 1 & 0 \\ 0 & 1 \\ 0 & 0 \end{bmatrix} \begin{bmatrix} e_1 \\ e_2 \end{bmatrix} \qquad (4.10)$$

In this case we have:

$$E = \begin{bmatrix} L_1 & 0 & L_3 \\ 0 & L_2 & L_3 \\ 0 & 0 & 0 \end{bmatrix}, \quad A = \begin{bmatrix} -R_1 & 0 & -R_3 \\ 0 & -R_2 & -R_3 \\ 1 & 1 & -1 \end{bmatrix}, \quad B = \begin{bmatrix} 1 & 0 \\ 0 & 1 \\ 0 & 0 \end{bmatrix} \quad (4.11)$$

Note that the matrix E is singular but the pencil:

$$\det[Es^\beta - A] = \begin{vmatrix} L_1 s^\beta + R_1 & 0 & L_3 s^\beta + R_3 \\ 0 & L_2 s^\beta + R_2 & L_3 s^\beta + R_3 \\ -1 & -1 & 1 \end{vmatrix}$$

$$= [L_1(L_2 + L_3) + L_2 L_3]s^{2\beta} \qquad (4.12)$$

$$+ [(L_2 + L_3)R_1 + (L_1 + L_3)R_2 + (L_1 + L_2)R_3]s^\beta$$

$$+ R_1(R_2 + R_3) + R_2 R_3$$

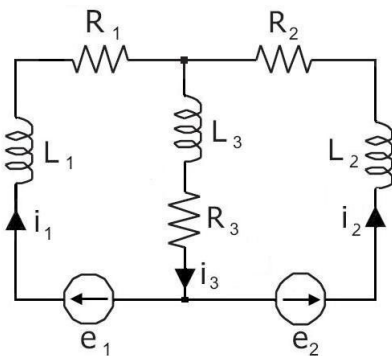is regular. Therefore, the electrical circuit is a singular fractional linear system.

Fig.2. Electrical circuit

Remark 4.2. If the electrical circuit contains at least one node with branches with supercoils then its matrix E is singular since it has

at least one zero row. This follows from the fact that the equation written using the current Kirchhoff's law for this node is algebraic one.

In general case we have the following theorem.
Theorem 4.1. Every electrical circuit is a singular fractional system if it contains at least one mesh consisting of branches with only ideal supercondensators and voltage source or at least one node with branches with supercoils.
Proof. By Remark 2.1 the matrix E of the system is singular if the electrical circuit contains at least one mesh consisting of branches with only ideal supercondensators and voltage source. Similarly by Remark 2.2 the matrix E is singular if the electrical circuit contains at least one node with branches with supercoils.

Using the solution (3.14) of the equation (3.1a) we may find the voltages on the supercondensators and currents in the supercoils in the transient states of the singular fractional linear electrical circuits. Knowing the voltages and currents and using (3.15) we may find also any currents and voltages in the singular fractional linear electrical circuits.

Example 4.3. (an continuation of Example 4.1)
Using one of the well-known methods (Podlubny, 1999; Dodig and Stosic, 2009; Kaczorek, 1992) we can find for the pencil (4.8) the matrices:

$$P = \begin{bmatrix} \dfrac{1}{RC_1} & 0 & -\dfrac{C_2}{RC_1(C_2 + C_3)} \\ -\dfrac{1}{R(C_2 + C_3)} & \dfrac{1}{C_2 + C_3} & \dfrac{C_2}{R(C_2 + C_3)^2} \\ 0 & 0 & -1 \end{bmatrix},$$

$$(4.13)$$

$$Q = \begin{bmatrix} 1 & 0 & 0 \\ 0 & 1 & \dfrac{C_3}{C_2 + C_3} \\ 0 & -1 & \dfrac{C_2}{C_2 + C_3} \end{bmatrix}$$

which transform it to the canonical form (3.3) with:

$$A_1 = \begin{bmatrix} -\dfrac{1}{RC_1} & \dfrac{1}{RC_1} \\ \dfrac{1}{R(C_2 + C_3)} & -\dfrac{1}{R(C_2 + C_3)} \end{bmatrix}, \qquad (4.14)$$

$$N = [0], \quad n_1 = 2, \quad n_2 = 1$$

Using the matrix B given by (4.7), (4.13) and (3.6c) we obtain:

$$\begin{bmatrix} B_1 \\ B_2 \end{bmatrix} = PB = \begin{bmatrix} \dfrac{1}{RC_1} & -\dfrac{C_2}{RC_1(C_2 + C_3)} \\ -\dfrac{1}{R(C_2 + C_3)} & \dfrac{C_2}{R(C_2 + C_3)^2} \\ 0 & -1 \end{bmatrix} \qquad (4.15)$$

from (3.7) we have:

$$x_1(t) = \Phi_{10}(t)x_{10} + \int_0^t \Phi_{11}(t-\tau)B_1 u(\tau) d\tau \qquad (4.16)$$

for any given initial condition $x_{10} \in \mathfrak{R}^{n_1}$ and input $u(t)$, where:

$$\Phi_{10}(t) = \sum_{k=0}^{\infty} \frac{A_1^k t^{k\alpha}}{\Gamma(k\alpha+1)}, \quad \Phi_{11}(t) = \sum_{k=0}^{\infty} \frac{A_1^k t^{(k+1)\alpha-1}}{\Gamma[(k+1)\alpha]},$$

$$0 < \alpha < 1$$

In this case using (3.13) we obtain:

$$x_2(t) = -B_2 u(t) \qquad (4.17)$$

since $N = [0]$.

In a similar way we may find currents in the supercoils of the singular fractional electrical circuit shown in Fig. 2.

5. FRACTIONAL DISCRETE-TIME LINEAR SYSTEMS

Consider the singular fractional discrete-time linear system described by the state equation:

$$E\Delta^\alpha x_{i+1} = Ax_i + Bu_i , \ i \in Z_+ = \{0,1,...\} \qquad (5.1)$$

where: $x_i \in \mathfrak{R}^n$, $u_i \in \mathfrak{R}^m$ are the state and input vectors, $A \in \mathfrak{R}^{n \times n}$, $E \in \mathfrak{R}^{n \times n}$, $B \in \mathfrak{R}^{n \times m}$ and the fractional difference of the order α is defined by:

$$\Delta^\alpha x_i = \sum_{k=0}^{i} (-1)^k \binom{\alpha}{k} x_{i-k} , \ 0 < \alpha < 1 \qquad (5.2)$$

$$\binom{\alpha}{k} = \begin{cases} 1 & \text{for } k = 0 \\ \dfrac{\alpha(\alpha-1)...(\alpha-k+1)}{k!} & \text{for } k = 1,2,... \end{cases} \qquad (5.3)$$

It is assumed that:

$$\det E = 0 \qquad (5.4a)$$

and:

$$\det[Ez - A] \neq 0 \qquad (5.4b)$$

for some $z \in C$ (the field of complex numbers).
Lemma 5.1. (Fahmy and O'Reill, 1989; Kaczorek, 1992) If (5.4) holds then there exist nonsingular matrices $P, Q \in \mathfrak{R}^{n \times n}$ such that:

$$PEQ = \begin{bmatrix} I_{n_1} & 0 \\ 0 & N \end{bmatrix}, \quad PAQ = \begin{bmatrix} A_1 & 0 \\ 0 & I_{n_2} \end{bmatrix} \qquad (5.5)$$

where: $N \in \mathfrak{R}^{n_2 \times n_2}$ is a nilpotent matrix with the index μ (i.e. $N^\mu = 0$ and $N^{\mu-1} \neq 0$), $A_1 \in \mathfrak{R}^{n_1 \times n_1}$, n_1 is equal to degree of the polynomial:

$$\det[Es - A] = a_{n_1} z^{n_1} + ... + a_1 z + a_0 \qquad (5.6)$$

and $n_1 + n_2 = n$.
A method for computation of the matrices P and Q has been given in Van Dooren (1979).

Using Lemma 5.1 we shall derive the solution x_i to the equation (5.1) for a given initial conditions x_0 and an input vector $u_i, \ i \in Z_+$.

6. SOLUTION OF THE SINGULAR FRACTIONAL DISCRETE-TIME LINEAR SYSTEMS

Premultiplying the equation (5.1) by the matrix $P \in \mathfrak{R}^{n \times n}$ and introducing the new state vector:

$$\bar{x}_i = \begin{bmatrix} \bar{x}_i^{(1)} \\ \bar{x}_i^{(2)} \end{bmatrix} = Q^{-1} x_i , \ \bar{x}_i^{(1)} \in \mathfrak{R}^{n_1} , \ \bar{x}_i^{(2)} \in \mathfrak{R}^{n_2} , \ i \in Z_+ \quad (6.1)$$

we obtain:

$$PEQQ^{-1}\Delta^\alpha x_{i+1} = PEQ\Delta^\alpha Q^{-1} x_{i+1} = PAQQ^{-1} x_i + PBu_i (6.2)$$

and after using (5.5) and (6.1):

$$\begin{bmatrix} I_{n_1} & 0 \\ 0 & N \end{bmatrix} \Delta^\alpha \begin{bmatrix} \bar{x}_{i+1}^{(1)} \\ \bar{x}_{i+1}^{(2)} \end{bmatrix} = \begin{bmatrix} A_1 & 0 \\ 0 & I_{n_2} \end{bmatrix} \begin{bmatrix} \bar{x}_i^{(1)} \\ \bar{x}_i^{(2)} \end{bmatrix} + \begin{bmatrix} B_1 \\ B_2 \end{bmatrix} u_i , \ i \in Z_+$$

$$(6.3)$$

where:

$$\begin{bmatrix} B_1 \\ B_2 \end{bmatrix} = PB , \ B_1 \in \mathfrak{R}^{n_1 \times m} , \ B_2 \in \mathfrak{R}^{n_2 \times m} \qquad (6.4)$$

Taking into account (5.2) from (6.3) we obtain:

$$\bar{x}_{i+1}^{(1)} = -\sum_{k=1}^{i+1} (-1)^k \binom{\alpha}{k} \bar{x}_{i-k+1}^{(1)} + A_1 \bar{x}_i^{(1)} + B_1 u_i$$

$$= A_{1\alpha} \bar{x}_i^{(1)} + \sum_{k=2}^{i+1} (-1)^{k-1} \binom{\alpha}{k} \bar{x}_{i-k+1}^{(1)} + B_1 u_i \qquad (6.5)$$

and:

$$N \left[\bar{x}_{i+1}^{(2)} + \sum_{k=1}^{i+1} (-1)^k \binom{\alpha}{k} \bar{x}_{i-k+1}^{(2)} \right] = \bar{x}_i^{(2)} + B_2 u_i \qquad (6.6)$$

where: $A_{1\alpha} = A_1 + I_{n_1}\alpha$.
The solution $\bar{x}_i^{(1)}$ to the equation (6.5) is well-known (Kaczorek, 2007b; 2010) and it is given by the theorem.
Theorem 6.1. The solution $\bar{x}_i^{(1)}$ of the equation (6.5) is given by the formula:

$$\bar{x}_i^{(1)} = \Phi_i \bar{x}_0^{(1)} + \sum_{k=0}^{i-1} \Phi_{i-k-1} B_1 u_k , \ i \in Z_+ \qquad (6.7)$$

where the matrices Φ_i are determined by the equation:

$$\Phi_{i+1} = \Phi_i A_{1\alpha} + \sum_{k=2}^{i+1} (-1)^{k-1} \binom{\alpha}{k} \Phi_{i-k+1} \quad \Phi_0 = I_{n_1} \qquad (6.8)$$

To find the solution $\bar{x}_i^{(2)}$ of the equation (6.6) for $N \neq 0$ it is assumed that:

$$N = \begin{bmatrix} 0 & 0 & ... & 0 & 0 \\ 1 & 0 & ... & 0 & 0 \\ 0 & 1 & ... & 0 & 0 \\ \vdots & \vdots & \ddots & \vdots & \vdots \\ 0 & 0 & ... & 1 & 0 \end{bmatrix} \in \Re^{n_2} \qquad (6.9)$$

For (6.9) the equation (6.6) can be written in the form:

$$\begin{bmatrix} 0 & 0 & ... & 0 & 0 \\ 1 & 0 & ... & 0 & 0 \\ 0 & 1 & ... & 0 & 0 \\ \vdots & \vdots & \ddots & \vdots & \vdots \\ 0 & 0 & ... & 1 & 0 \end{bmatrix} \left(\sum_{j=0}^{i+1}(-1)^j\binom{\alpha}{j}\begin{bmatrix} \bar{x}_{i-j+1}^{(21)} \\ \bar{x}_{i-j+1}^{(22)} \\ \vdots \\ \bar{x}_{i-j+1}^{(2,n_2)} \end{bmatrix} \right), \ i \in Z_+ \qquad (6.10)$$

$$= \begin{bmatrix} \bar{x}_i^{(21)} \\ \bar{x}_i^{(22)} \\ \vdots \\ \bar{x}_i^{(2,n_2)} \end{bmatrix} + \begin{bmatrix} B_{21} \\ B_{22} \\ \vdots \\ B_{2,n_2} \end{bmatrix} u_i$$

From (6.10) we have:

$$\bar{x}_i^{(21)} = -B_{21}u_i$$

$$\bar{x}_i^{(22)} = \sum_{j=0}^{i+1}(-1)^j\binom{\alpha}{j}\bar{x}_{i-j+1}^{(21)} - B_{22}u_i$$

$$= -\sum_{j=0}^{i+1}(-1)^j\binom{\alpha}{j}B_{21}u_{i-j+1} - B_{22}u_i$$

$$\bar{x}_i^{(23)} = \sum_{j=0}^{i+1}(-1)^j\binom{\alpha}{j}\bar{x}_{i-j+1}^{(22)} - B_{23}u_i \qquad (6.11)$$

$$= -\sum_{j=0}^{i+1}(-1)^j\binom{\alpha}{j}\sum_{k=0}^{i-j+2}(-1)^k\binom{\alpha}{k}B_{21}u_{i-j-k+2}$$

$$-\sum_{j=0}^{i+1}(-1)^j\binom{\alpha}{j}B_{22}u_{i-j+1} - B_{23}u_i$$

$$\vdots$$

$$\bar{x}_i^{(2,n_2)} = \sum_{j=0}^{i+1}(-1)^j\binom{\alpha}{j}\bar{x}_{i-j+1}^{(2,n_2-1)} - B_{2,n_2}u_i$$

If $N = 0$ then from (6.6) we have:

$$\bar{x}_i^{(2)} = -B_2u_i, \ i \in Z_+ \qquad (6.12)$$

This approach can be easily extended for :

$$N = blockdiag \ [N_1 \quad N_2 \quad ... \quad N_h] \qquad (6.13)$$

where: $N_k \in \Re^{n_k}$ has the form (6.9) and $\sum_{i=1}^{h} n_k = n_2$.

If the matrix N has the form:

$$N = \begin{bmatrix} 0 & 1 & 0 & ... & 0 \\ 0 & 0 & 1 & ... & 0 \\ \vdots & \vdots & \vdots & \ddots & \vdots \\ 0 & 0 & 0 & ... & 1 \\ 0 & 0 & 0 & ... & 0 \end{bmatrix} \in \Re^{n_2} \qquad (6.9')$$

the considerations are similar (dual).

Note that the matrices (6.9) and (6.9') are related by:

$$N = S\bar{N}S \quad \text{where} \quad S = \begin{bmatrix} 0 & 0 & ... & 0 & 1 \\ 0 & 0 & ... & 1 & 0 \\ \vdots & \vdots & ... & \vdots & \vdots \\ 1 & 0 & ... & 0 & 0 \end{bmatrix}.$$

Knowing $\bar{x}_i^{(1)}$ and $\bar{x}_i^{(2)}$ we can find the desired solution of the equation (5.1) from (6.1):

$$x_i = Q\begin{bmatrix} \bar{x}_i^{(1)} \\ \bar{x}_i^{(2)} \end{bmatrix}, \ i \in Z_+ \qquad (6.14)$$

7. EXAMPLES OF SINGULAR FRACTIONAL DISCRETE-TIME SYSTEMS

Example 7.1. Find the solution x_i of the singular fractional linear system (5.1) with the matrices:

$$E = \begin{bmatrix} -1 & -1 & -1 \\ 2 & 4 & 2 \\ 1 & 4 & 1 \end{bmatrix}, \ A = \begin{bmatrix} 0.8 & 1.7 & 2.8 \\ 0.4 & 0.8 & 1.4 \\ 2.2 & 4.6 & 2.2 \end{bmatrix}, \ B = \begin{bmatrix} 1 \\ 0 \\ -1 \end{bmatrix} \qquad (7.1)$$

for $\alpha = 0.5$, $u_i = u$, $i \in Z_+$ and $x_0 = [1 \ \ 2 \ \ -1]^T$ (T denotes the transpose).

It is easy to check that the matrices (7.1) satisfy the assumptions (5.4). In this case the matrices P and Q have the forms:

$$P = \frac{1}{11}\begin{bmatrix} 1 & -2 & 5 \\ -2 & 4 & 1 \\ 4 & 3 & -2 \end{bmatrix}, \ Q = \begin{bmatrix} -2 & 1 & -1 \\ 1 & 0 & 0 \\ 0 & 0 & 1 \end{bmatrix} \qquad (7.2)$$

and:

$$\begin{bmatrix} I_{n_1} & 0 \\ 0 & N \end{bmatrix} = PEQ = \begin{bmatrix} 1 & 0 & 0 \\ 0 & 1 & 0 \\ 0 & 0 & 0 \end{bmatrix},$$

$$\begin{bmatrix} A_1 & 0 \\ 0 & I_{n_2} \end{bmatrix} = PAQ = \begin{bmatrix} 0.1 & 1 & 0 \\ 0 & 0.2 & 0 \\ 0 & 0 & 1 \end{bmatrix}, \qquad (7.3)$$

$$PB = \begin{bmatrix} B_1 \\ B_2 \end{bmatrix} = \frac{1}{11}\begin{bmatrix} -4 \\ -3 \\ 6 \end{bmatrix}, \ A_{1\alpha} = A_1 + I_{n_1}\alpha = \begin{bmatrix} 0.6 & 1 \\ 0 & 0.7 \end{bmatrix},$$

$(n_1 = 2, n_2 = 1)$

The equations (6.5) and (6.6) have the forms:

$$\bar{x}_{i+1}^{(1)} = \begin{bmatrix} 0.6 & 1 \\ 0 & 0.7 \end{bmatrix}\bar{x}_i^{(1)} + \sum_{k=2}^{i+1}(-1)^{k-1}\binom{0.5}{k}\bar{x}_{i-k+1}^{(1)} - \frac{1}{11}\begin{bmatrix} 4 \\ 3 \end{bmatrix}u_i, \ i \in Z_+$$

$$(7.4)$$

and:

$$\bar{x}_i^{(2)} = -B_2 u_i = -\frac{6}{11} u_i , \ i \in Z_+ \tag{7.5}$$

The solution $\bar{x}_i^{(1)}$ of the equation (7.4) has the form:

$$\bar{x}_i^{(1)} = \Phi_i \bar{x}_0^{(1)} + \sum_{k=0}^{i-1} \Phi_{i-k-1} B_1 u_k , \ i \in Z_+ \tag{7.6}$$

where:

$$\Phi_0 = \begin{bmatrix} 1 & 0 \\ 0 & 1 \end{bmatrix}, \ \Phi_1 = A_{1\alpha} = \begin{bmatrix} 0.6 & 1 \\ 0 & 0.7 \end{bmatrix},$$

$$\Phi_2 = A_{1\alpha}^2 - I_{n_1} \frac{\alpha(\alpha-1)}{2!} = \begin{bmatrix} 0.485 & 1.300 \\ 0 & 0.615 \end{bmatrix}, ... \tag{7.7}$$

and:

$$\bar{x}_0 = Q^{-1} x_0 = \begin{bmatrix} 0 & 1 & 0 \\ 1 & 2 & 1 \\ 0 & 0 & 1 \end{bmatrix} \begin{bmatrix} 1 \\ 2 \\ -1 \end{bmatrix} = \begin{bmatrix} 2 \\ 4 \\ -1 \end{bmatrix},$$

$$\bar{x}_0^{(1)} = \begin{bmatrix} 2 \\ 4 \end{bmatrix}, \ \bar{x}_0^{(2)} = [-1] \tag{7.8}$$

The desired solution of the singular fractional system with (7.1) is given by:

$$x_i = Q\bar{x}_i = \begin{bmatrix} -2 & 1 & -1 \\ 1 & 0 & 0 \\ 0 & 0 & 1 \end{bmatrix} \begin{bmatrix} \bar{x}_i^{(1)} \\ \bar{x}_i^{(2)} \end{bmatrix} \tag{7.9}$$

where $\bar{x}_i^{(1)}$ and $\bar{x}_i^{(2)}$ are determined by (6.7) and (7.5), respectively.

Example 7.2. Find the solution x_i of the singular fractional linear system (5.1) with the matrices:

$$E = \begin{bmatrix} 1 & 0 & 0 \\ 0 & 1 & -1 \\ 1 & -1 & 1 \end{bmatrix}, \ A = \begin{bmatrix} 0.2 & 2 & -2 \\ 2 & 1 & 0 \\ -1.8 & 0 & -1 \end{bmatrix}, \ B = \begin{bmatrix} 1 & 2 \\ -1 & 2 \\ 2 & -1 \end{bmatrix} \tag{7.10}$$

for $\alpha = 0.8$, arbitrary $u_i, \ i \in Z_+$ and $x_0 = [1 \ 1 \ 1]^T$.

It is easy to check that the matrices (7.10) satisfy the assumptions (5.4). In this case the matrices P and Q have the forms:

$$P = \begin{bmatrix} -1 & 2 & 2 \\ 1 & -1 & -1 \\ -1 & 2 & 1 \end{bmatrix}, \ Q = \begin{bmatrix} 1 & 0 & 0 \\ -2 & 1 & 1 \\ -2 & 0 & 1 \end{bmatrix} \tag{7.11}$$

and:

$$\begin{bmatrix} I_{n_1} & 0 \\ 0 & N \end{bmatrix} = PEQ = \begin{bmatrix} 1 & 0 & 0 \\ 0 & 0 & 0 \\ 0 & 1 & 0 \end{bmatrix},$$

$$\begin{bmatrix} A_1 & 0 \\ 0 & I_{n_2} \end{bmatrix} = PAQ = \begin{bmatrix} 0.2 & 0 & 0 \\ 0 & 1 & 0 \\ 0 & 0 & 1 \end{bmatrix}, \tag{7.12}$$

$$PB = \begin{bmatrix} B_1 \\ B_2 \end{bmatrix} = \begin{bmatrix} 1 & 0 \\ 0 & 1 \\ -1 & 1 \end{bmatrix}, \ A_{1\alpha} = A_1 + I_{n_1}\alpha = [1],$$

$(n_1 = 1, n_2 = 2)$

In this case the equations (6.5) and (6.6) have the forms:

$$\bar{x}_{i+1}^{(1)} = \bar{x}_i^{(1)} + \sum_{k=2}^{i+1} (-1)^{k-1} \binom{0.8}{k} \bar{x}_{i-k+1}^{(1)} + [1 \ 0] u_i , i \in Z_+ \tag{7.13}$$

$$\begin{bmatrix} 0 & 0 \\ 1 & 0 \end{bmatrix} \left(\sum_{j=0}^{i+1} (-1)^j \binom{0.8}{j} \begin{bmatrix} \bar{x}_{i-j+1}^{(21)} \\ \bar{x}_{i-j+1}^{(22)} \end{bmatrix} \right) = \begin{bmatrix} \bar{x}_i^{(21)} \\ \bar{x}_i^{(22)} \end{bmatrix} + \begin{bmatrix} 0 & 1 \\ -1 & 1 \end{bmatrix} u_i , i \in Z_+ \tag{7.14}$$

and:

$$\bar{x}_0 = Q^{-1} x_0 = \begin{bmatrix} 1 & 0 & 0 \\ 0 & 1 & -1 \\ 2 & 0 & 1 \end{bmatrix} \begin{bmatrix} 1 \\ 1 \\ 1 \end{bmatrix} = \begin{bmatrix} 1 \\ 0 \\ 3 \end{bmatrix}, \ \bar{x}_0^{(1)} = [1], \ \bar{x}_0^{(2)} = \begin{bmatrix} 0 \\ 3 \end{bmatrix} \tag{7.15}$$

The solution $\bar{x}_i^{(1)}$ of the equation (7.13) with $\bar{x}_0^{(1)} = 1$ can be easily found using (6.7) and (6.8).
From (7.14) we have:

$$\bar{x}_i^{(21)} = [0 \ -1] u_i, \ i \in Z_+$$

$$\bar{x}_i^{(22)} = \sum_{j=0}^{i+1} (-1)^j \binom{0.8}{j} [0 \ -1] u_{i-j+1} + [1 \ -1] u_i, \ i \in Z_+ \tag{7.16}$$

The desired solution of the singular fractional system with (7.10) is given by:

$$x_i = Q\bar{x}_i = \begin{bmatrix} 1 & 0 & 0 \\ -2 & 1 & 1 \\ -2 & 0 & 1 \end{bmatrix} \begin{bmatrix} \bar{x}_i^{(1)} \\ \bar{x}_i^{(21)} \\ \bar{x}_i^{(22)} \end{bmatrix} \tag{7.17}$$

where: $\bar{x}_i^{(1)}, \bar{x}_i^{(21)}$ and $\bar{x}_i^{(22)}$ are determined by (7.13) and (7.16), respectively.

8. CONCLUDING REMARKS

The singular fractional linear systems and electrical circuits have been introduced. Using the Caputo definition of the fractional derivative, the Weierstrass regular pencil decomposition and the Laplace transform the solution to the state equation of singular fractional linear system has been derived (Theorem 3.1). Singular

fractional linear electrical circuits have been analyzed. It has been shown that every electrical circuit is a singular fractional system if it contains at least one mesh consisting of branches with only ideal supercondensators and voltage sources or at least one node with branches with supercoils (Theorem 4.1). The singular fractional linear discrete-time systems have been introduced. Using the Weierstrass regular pencil decomposition the solution to the state equation of singular fractional linear discrete-time system has been derived. The method of finding of the solution to the singular fractional systems has been illustrated by two examples. The considerations have been illustrated by singular linear electrical circuits. Those considerations can be extended for singular fractional linear systems with singular pencils. Open problem are extension of these considerations for positive singular fractional linear systems and for singular positive linear systems with different fractional order. The linear systems with different fractional orders are described by the equation (Kaczorek, 2007a).

$$\begin{bmatrix} \dfrac{d^\alpha x_1}{dt^\alpha} \\ \dfrac{d^\beta x_2}{dt^\beta} \end{bmatrix} = \begin{bmatrix} A_{11} & A_{12} \\ A_{21} & A_{22} \end{bmatrix}\begin{bmatrix} x_1 \\ x_2 \end{bmatrix} + \begin{bmatrix} B_1 \\ B_2 \end{bmatrix}u,$$

$$p-1 < \alpha < p; \quad q-1 < \beta < q; \quad p,q \in N$$

(8.1)

where: $x_1 \in \Re^{n_1}$, $x_2 \in \Re^{n_2}$ are the state vectors and $A_{ij} \in \Re^{n_i \times n_j}$, $B_i \in \Re^{n_i \times m}$, $i,j = 1,2$ and $u \in \Re^m$ is the input vector. Initial conditions for (8.1) have the form $x_1(0) = x_{10}$ and $x_2(0) = x_{20}$.

REFERENCES

1. **Benvenuti L., Farina L.** (2004), A tutorial on the positive realization problem, *IEEE Trans. Autom. Control*, Vol. 49, No. 5, 651-664.
2. **Dail L.** (1989), *Singular control systems, Lectures Notes in Control and Information Sciences*, Springer-Verlag, Berlin.
3. **Dodig M. Stosic M.** (2009), Singular systems state feedbacks problems, Linear Algebra and its Applications, Vol. 431, No. 8, 1267-1292.
4. **Fahmy M.H, O'Reill J.** (1989), Matrix pencil of closed-loop descriptor systems: infinite-eigenvalues assignment, Int. J. Control, Vol. 49, No. 4, 1421-1431.
5. **Gantmacher F. R.** (1960), *The theory of Matrices*, Chelsea Publishing Co., New York.
6. **Kaczorek T.** (1992), *Linear control systems*, Vol. 1, Research Studies Press J. Wiley, New York.
7. **Kaczorek T.** (2004), Infinite eigenvalue assignment by output-feedbacks for singular systems, Int. J. Appl. Math. Comput. Sci., Vol. 14, No. 1, 19-23.
8. **Kaczorek T.** (2007a), *Polynomial and rational matrices. Applications in dynamical systems theory*, Springer-Verlag, London.
9. **Kaczorek T.** (2007b), Realization problem for singular positive continuous-time systems with delays, *Control and Cybernetics*, Vol. 36, No. 1, 47-57.
10. **Kaczorek T.** (2008), Fractional positive continuous-time linear systems and their reachability, *Int. J. Appl. Math. Comput. Sci.*, Vol. 18, No. 2, 223-228.
11. **Kaczorek T.** (2010a), Analysis of fractional electrical circuits in transient states*, VII Konferencja Naukowo-Techniczna : Logistyka - systemy transportowe - bezpieczeństwo w transporcie*, Szczyrk.
12. **Kaczorek T.** (2010b), Positive linear systems with different fractional orders, *Bull. Pol. Ac. Sci. Techn.*, Vol. 58, No. 3, 453-458.
13. **Kaczorek T.** (2011) *Selected Problems in Fractional Systems Theory*, Springer-Verlag.
14. **Kucera V. Zagalak P.** (1988), Fundamental theorem of state feedback for singular systems, *Automatica*, Vol. 24, No. 5, 653-658.
15. **Podlubny I.** (1999), *Fractional differential equations, Academic Press*, New York.
16. **Van Dooren P.** (1979), The computation of Kronecker's canonical form of a singular pencil, *Linear Algebra and Its Applications*, Vol. 27, 103-140.

EXPERIMENT OF GASIFICATION OF THE SYNTHETICALLY MIXED SAMPLE OF WASTE IN NITROGEN ATMOSPHERE

Marián LÁZÁR*, Natália JASMINSKÁ*, Marta LENGYELOVÁ*

*Faculty of Mechanical Engineering, Technical University of Košice, ul. Vysokoškolská 4, 042 00 Košice, Slovak Republic

marian.lazar@tuke.sk, natalia.jasminska@tuke.sk, marta.lengyelova@tuke.sk

Abstract: The article presents results of gasification of the synthetically mixed sample of waste in a 30 kVA transferred DC plasma reactor with a hollow graphite electrode. The subject of the research is a sample of waste consisting of components normally found in a municipal waste. The experimental test of waste gasification with a high level of organic fraction was implemented due to the verification of previously mentioned technology application also in the area of waste disposal at the current construction design of the reactor. Gasification took place in the inert atmosphere at the average temperature of 1578 °C. The goal of the experiment was the verification of possible synthesis gas production applicable in the energetic applications and focus of the possible usage of the energetic potential of, up to now not often used, secondary energy sources such as wastes.

Key words: Plasma Reactor, Gasification, Organic Waste, Syngas

1. INTRODUCTION

One of the main problems of the countries in economical development is the processing and disposal of constantly growing amount of wastes. This problem is demonstrated especially in the countries where the population density reaches a high level (e.g. Japan) and spaces for the landfilling of waste are limited. Landfilling is currently the most known and at the same time the cheapest way in the area of mixed waste disposal. It plays a dominant role in the waste management in various countries all over the world. Disadvantages of this simple method of waste disposal lie in ground water and soil pollution, creation of malodor and nevertheless it destroys the country landscape. All the toxic matters contained in the waste remain in an unknown and uncontrolled form inside of the landfills. Realizing the environmental problems connected with the mixed waste landfilling, at present, the vast majority of states worldwide limit possibilities of waste landfilling through various laws and support the development of new technologies (Koukouzas et.al., 2008; Horbaj et.al., 2000).

The latter tendency in the area of thermal processing of various types of waste is their processing by a plasma technology. Waste disposal represents a complex process containing many physical and chemical interactions at the average temperature higher than 1 000 °C. The average operating temperature in the plasma reactor is affected by the characteristics of the processed waste, by the requirements for the output products from the process, by the type of the reactor used and so on (Arena, 2012). Gasification has several potential benefits over traditional combustion of solid waste, mainly related to the possibility of combining the operating conditions to obtain a syngas suitable for use in different applications (Arena, 2012).

Over the recent years several studies have been conducted to determine whether thermal plasma processes can be used for the gasification of waste with a high level of organic fraction. In many cases the results show a real possibility of using the plasma technology in the area of waste disposal (Gomez et.al., 2009; Shibaike et.al., 2005; Tanigaki et.al., 2012; Hrabovský, 2011; Consonni, et.al., 2012).

2. TECHNOLOGY DESCRIPTION

The experiment of gasification of the synthetically mixed sample of waste was carried out in a 30 kVA transferred DC plasma reactor with a hollow graphite electrode. The heat necessary for the destruction of waste is ensured by a plasma arch generated between the hollow graphite electrode (cathode) and furnace hearth (anode). In most of the cases nitrogen or the air is used as gas necessary to create the plasma arch, which is transformed into the plasma state under the influence of electric field at high intensity. The simplified 3D model of plasma gasification technology is shown in the Fig. 1.
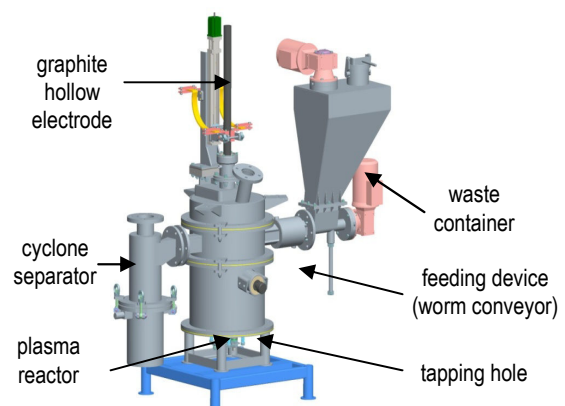

Fig. 1. 3D scheme of 30 kVA plasma reactor

The graphite furnace hearth (anode) placed on the bottom of the reactor is protected by a layer of pure copper within every

gasification experiment. Reactor shell is cooled down by the surrounding air. The synthetically mixed sample of waste entering the reactor is modified to granularity lower than 5 mm due to constructional reasons as well as better effectivity of the gasification process (Imriš, 2006).

3. THE EXPERIMENT OF GASIFICATION

In the experimental test a possibility of synthetically mixed sample of waste gasification was examined. The sample of waste consisted of five components, i.e. paper, plastics, biological waste, textile and glass. The percentage of the individual compound components in the mixture of waste sample is shown in Fig. 2. The basic physical characteristics, elemental analysis and the number of moles contained in the individual compound components, for 100 g of synthetically mixed sample of waste is shown in the Tab. 1.
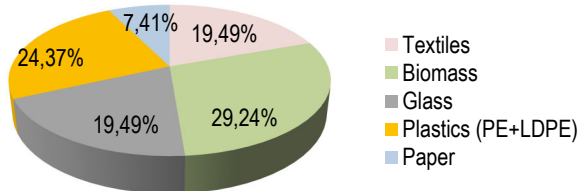

Fig. 2. The percentage of the individual compound components in the charge

Feeding of the charge of waste to the plasma reactor reaction chamber was provided by a tangential feeding device (worm conveyor) with a possibility of continuous waste feeding with granularity < 5 mm. The continuous feeding was in progress in a two-second interval followed by a 28-second pause. This process was cyclically repeated until the moment of total emptying of the waste container.

The gasification process was realized in a reduction atmosphere at nitrogen flowing via cathode 0,00981 m3·min-1. The total nitrogen capacity used for sealing the filling around the cathode and for avoiding the breakaway of the syngas via the waste container was at the level of 0,00669 m3·min-1. Plasma arch generated between a hollow graphite electrodes (cathode), placed in a centrical way in the plasma reactor and a graphite furnace hearth which creates the bottom of the reactor (anode), maintain the temperature in the reactor chamber on the required level. The syngas produced is taken away using an aperture for a syngas exiting from the top of the reactor, directed to a cyclone separator which creates the first level of the syngas cleaning circuit. The operating parameters of gasification characterizing the gasification process of the synthetically mixed sample of waste are

listed in the Tab. 2.

Tab. 2. Operating parameters of the synthetically mixed sample of waste gasification

Operating parameters	Unit	Measurement results	
		Calculation based on the parameters of worm conveyor	Experimental measurement
Average temperature	°C	1 578	1 578
Total feeding time	min.	21,6	20
Charge weight	kg	5,130	5,130
Feeding speed	kg·min-1	0,2375	0,257
Nitrogen flow	m3·min-1	0,0165	0,0165
Total energy expenditure	kWh	16,4	15,2
Specific energy expenditure	kWh·kg-1	3,197	2,963
Syngas production	m3·kg-1	1,069	1,018

Total feeding time in case of the experimental measurement was estimated on the basis of a visual control of the waste container filling level and on the basis of calculation which was based on the waste container constructional dimensions, number of revolutions and a set feeding interval.

In the course of the experiment there were 3 syngas sample takings carried out, in the 6th, 17th and 29th minute from the beginning of the charge (waste) feeding. The third syngas sample was taken right after the end of the feeding process. The analyzed syngas results are shown in the Table 3.

While taking the individual syngas samples there was a high concentration of non-reacted carbon particulates contained in the gas. The total volume impurities in the syngas, captured in a cyclonic separator was at the level of 1,1 kg which represents approximately 21,5 wt. % of the charge weight. Vitrificated slag tapping was not carried out after the experiment due to a low volume of charge.

The theoretical value of the emerging syngas volume in the gasification process was set on the basis of carbon balance. At the calculations, the basis was the elemental analysis of charge (synthetically mixed waste) considering oxidation of the total carbon content in the waste.

Assumed syngas production (based on the C balance), being created by oxidation of 100 % carbon containing in the charge and considering percentage proportion of the individual syngas components corresponding to the taken samples, was set to the interval 1,66 to 1,87 m3·kg-1(Tanigaki et.al., 2012; Lázár, 2012).

Tab. 1. Elemental analysis of charge

Sample Type	Physical characteristics				Elemental analysis (in a dry residue)					
	W (%)	A (%)	H* (%)	Qs MJ·kg-1	C (%)	H (%)	N (%)	O (%)	S (%)	Cl (%)
Sample of waste	8,51	27,70	63,79	20,063	45,20	5,97	3,67	20,62	4,44E-03	--
Mole number [mol·(100 g)-1]	0,47	--	--	--	3,76	5,92	0,26	1,29	1,39E-04	--

Tab. 3. Results of the chromatographic analysis of syngas obtained by gasification of the synthetically mixed sample of waste

Analysis type	Chromatographic analysis		
	sample 1 (vol. %)	sample 2 (vol. %)	sample 3 (vol. %)
Methane (CH_4)	8,59	4,77	2,54
Hydrogen (H_2)	44,5	48,9	30,3
Oxygen (O_2)	0,16	0,11	0,74
Nitrogen (N_2)	6,03	6,61	15,9
Carbon dioxide(CO_2)	6,60	1,66	2,42
Carbon monoxide (CO)	32,5	37,1	47,3
Ethene (C_2H_4)	0,97	0,49	0,52
Ethane (C_2H_6)	0,055	0,031	0,023
Ethine (C_2H_2)	0,42	0,24	0,15
sum C_3 of hydrocarbons	0,011	0,004	0,004
sum C_4 of hydrocarbons	0,0099	0,004	0,005
sum C_{5-8} of hydrocarbons	0,17	0,12	0,09
Heat value	13,12 $MJ \cdot m^{-3}$	12,31 $MJ \cdot m^{-3}$	10,71 $MJ \cdot m^{-3}$

4. MODELING THE COMPOSITION OF THE SYNGAS BEING CREATED USING BOUNDARY EXPERIMENTAL CONDITIONS

Experimentally obtained results were verified in the simulating program HSC Chemistry. Syngas values, generated by the program and based on the heat dependence are shown in the Fig. 3.

As apparent from the Fig. 3 at temperatures over 1 000 °C, the main syngas parts are hydrogen and carbon monoxide. Percentage representation of these elements, considering the temperature of approximately 1 600 °C, ideal gasification conditions and thermodynamic balance, are within hydrogen 61,89 vol. % and carbon monoxide 31,84 vol. %. However, the above mentioned values of a percentage proportion of H2 and CO do not contain nitrogen volume transported to the reaction chamber. Considering the inserted nitrogen to the reaction chamber with a volume of 16,5 l·min-1, there will be a decrease in the volume proportion of hydrogen and carbon monoxide in the generated syngas (H2 around 58,18 vol. %, CO around 29,93 vol. %).

The oxygen deficiency in the reaction chamber of the plasma reactor causes the evasion of carbon particulates from reactor reaction chamber. The formation of the unreacted carbon is shown in the Fig. 3 by the blue chart curve. According to a software generated data, the assumption of carbon particulates formation in the quantity of 23,9 kg to 100 kg of charge. This value represents approximately 24 wt. % of the charge weight and it confirms the production of a high amount of carbon particulates, as observed during the experiment.
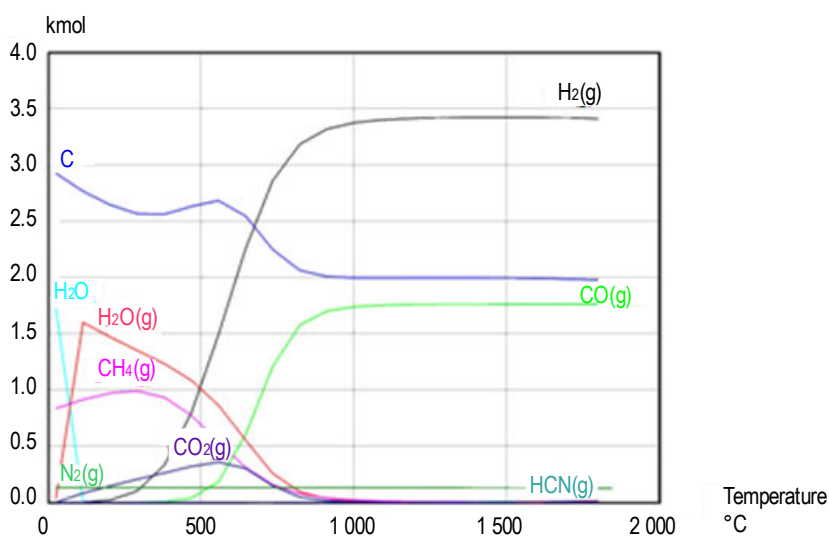
Fig. 3. Assumed syngas composition (generated by HSC Chemistry software)

5. THE EXPERIMENT OF GASIFICATION

Gasification of synthetically mixed sample of waste with a significant share of organic fraction was carried out in order to verify the plasma technology efficiency in the area of waste disposal and syngas production usable in energetic applications. Solid products of the plasma gasification, being created within the waste gasification experiment in the form of slag, non-reacted carbon particulates and fly ashes were only partially analyzed. At the suggested combustion temperature (1 600 °C) it is assumed that the complex waste molecules are decomposed to simple molecules and the organic share of charge is transformed to gas components.

Observing the results of the first two syngas analyses (sample taking in the course of feeding) it is possible to record an increase of percentage volume values of H2 a CO in the second sample and decrease of shares of methane, carbon dioxide and higher hydrocarbons. This phenomenon may be caused by slower charge decomposition in the gasification chamber of the plasma reactor (compared to the starting part of gasification), while methane is generated in the process is partially decomposed into carbon and hydrogen. Out of the third sample analysis there is an increase in the percentage of nitrogen in the syngas seen as well

as decrease in volume of many other compounds creating the gas mixture. The results of the third analysis confirm the presence of a higher charge content in the reaction chamber also after the end of the feeding process.

The volume of the syngas being produced (during the feeding) represents value around $1\ m^3{\cdot}kg^{-1}$ of the charge. Syngas production at the volume of $1\ m^3{\cdot}kg^{-1}$ of the charge considering the volume of non-reacted carbon in the form of fine particulates and syngas production also after the feeding process confirm applicability of the plasma technology also in the area of waste treating with a high share of organic fraction (from the technological point of view). The total volume of the two most important syngas components is at a remarkable level. The percentage share of hydrogen in syngas is between the intervals of 44 – 49 vol. % during feeding process. Carbon monoxide is represented in the interval of 32 – 37 vol. %.

In the overall assessment of the experiment of waste gasification with a significant share of organic fraction, it is possible to add that in the gasification of waste in a reducing condition, formation of non-reacted carbon particulates is notable due to high disproportion in carbon and oxide atoms present in the waste. Non-reacted carbon particulates formation was confirmed by the results from simulation of the synthetically mixed waste sample gasification as well as by the experiment.

Principally, it is possible to make use of the total volume of carbon and hydrogen atoms present in waste for syngas production at a sufficiently high temperature and sufficient number of oxidizer added into the reaction chamber of the plasma reactor. Maximum conversion of the organic part of the waste to syngas is obtained by a total carbon oxidation to carbon monoxide. Due to deficiency of oxygen atoms in the reaction chamber, compared to carbon atoms present in the majority of the materials of organic origin, there is an oxidizer added into the gasification process in a gas or liquid phase (Hrabovský, 2011). Based on the foreign literature, within biomass gasification in the air atmosphere, the ideal ratio between the oxygen volume in the oxidation process of thermal waste disposal and the oxygen volume necessary for a complex stoichiometric oxidation lies in the interval of 0,25 – 0,35. The presented ratio is very likely to be applicable also in waste gasification with a high share of organic fraction.

6. CONCLUSION

Gasification of municipal solid waste (MSW) and biomass as an energy recovery method has been widely researched all over the world (Tanigaki et.al., 2012, Blejchař et. al., 2007). There was confirmed the substantiality of plasma waste gasification with a high percentage of organic fraction in a 30 kVA plasma reactor. The chromatographic analysis results of the taken syngas samples show high level of the two most important combustible syngas parts, i.e. CO a H_2, which are applicable in energetic production systems. The representation of the CO and H2 elements in the syngas is at the level of 76 - 86 vol. %. The heat value in the gasification process of the generated gas is in the interval of 10,7 - 13,12 $MJ{\cdot}m^{-3}$.

Taking into consideration the results of the implemented experiment, focused on the syngas production applicable in energetic applications, plasma gasification represents a possible alternative also in the area of a common municipal waste disposal. Possibility to destroy organic and toxic matters contained in the municipal waste as well as the usage the chemical energy storage in the waste raise a question of starting a serious broad research in the particular area of waste disposal. However, optimization of the boundary gasification conditions and the construction adjustments of the reactor from the point of view of more effective syngas production are necessary. Higher gasification process effectivity lies, first of all, in solving the transportation of the oxidizer between the elements of the treated charge with a significant percentage of the organic fraction and in decreasing the energy consumption related to a kg of charge.

REFERENCES

1. **Arena U.** (2012), Process and technological aspects of municipal solid waste gasification. A review, *Waste Management*, Vol. 32, 625-639.
2. **Blejchař T., Čech B., Malý R., Kolat P., Dluhoš M.** (2007), Plazmové systémy v energetice *In: Environmental Protection into the Future*, Czenstochowa University of Technology, 30-42., ISBN 978-83-7193-340-0.
3. **Consonni S., Vigano F.** (2012), Waste gasification vs. conventional Waste-To-Energy: A comparative evaluation of two commercial Technologies, *Waste Management*,Vol. 32, 653-666.
4. **Gomez E., Rani A. D., Cheeseman R. C., Deegan D., Wise M., Boccaccini R. A.** (2009), Thermal plasma technology for the treatment of wastes, *Journal of Hazardous Materials*, Vol. 161, 614-626.
5. **Horbaj P., Imriš I.** (2000), Some possibilities of municipal waste treating (Niektoré možnosti využívania komunálneho odpadu), *International Conference TOP 2000*, Častá Papiernička 15–16 jún 2000, 233-243.
6. **Hrabovský M.** (2011), Thermal Plasma Gasification of Biomass, *Biomass and Bioenergy*, 39-62, ISBN 978-953-307-491-7.
7. **Imriš I.** (2006), Plasma reactor for waste treatment, *Heat transfer and renewable sources of energy* Szczecin, Wydawnictwo Uczelniane Politechniki Szczecinskiej, 301-308.
8. Internal Material of company „Silvergas s.r.o."
9. **Koukouzas N., Katsiadakis A., Karlopoulos E., Kakaras E.** (2008), Co-gasification of solid waste and lignite – A case study for Western Macedonia, *Waste Management*, Vol. 28, 1263-2675.
10. **Lázár M.** (2012), *Research of municipal waste utilization possibilities in the plasma reactor*, Doktorant thesis, Technical University of Košice.
11. **Shibaike, H.,** et. al. (2005), *Development of high-performance direct melting process for municipal solid waste*, Nippon Steel Technical Report [online].
12. **Tanigaki N., Manako K., Osada M.** (2012), Co-gasification of municipal solid waste and material recovery in a large-scale gasification and melting system, *Waste Management*, Vol. 32, 667-675.

CORROSION RESISTANCE OF MECHANICALLY ALLOYED 14%Cr ODS FERRITIC STEEL

Zbigniew OKSIUTA[*], Ewa OCH[*]

[*]Faculty of Mechanical Engineering, Bialystok University of Technology, ul. Wiejska 45c, 15-351 Białystok, Poland

z.oksiuta@pb.edu.pl, e.och@pb.edu.pl

Abstract: The paper presents results of the corrosion resistance of mechanically alloyed oxide dispersion strengthened 14% Cr ferritic stainless. The oxide dispersion strengthened steel was prepared by means of the powder metallurgy route that consists of mechanical alloying of a pre-alloyed argon atomized steel powder (Fe-14Cr-2W-0.3Ti) with 0.3 Y2O3 (wt%), followed by HIPping at 1150°C and annealing at 850°C for 1 h. The density of ODS ferritic steel after consolidation was about 99.0% of theoretical alloy density. The potentiodynamic corrosion tests were performed for 1h and 24 h of material exposure in a physiological saline solution. For comparison the 316 LV austenitic stainless steel was also examined. The obtained results revealed that both materials were in a passive stage, however the lower current corrosion density was measured for 316 LV steel. On the contrary, the austenitic stainless steel exhibited unstable chemical processes at the passive region. On the surface of both materials localized pitting corrosion was observed with different morphology of the cavities. A broken oxide scale with poor adhesion to the ferritic steel matrix with large number of density of localized corrosion attack was observed on the surface of the ODS steel.

Key words: ODS Ferritic Steel, 316 LV Austenitic Stainless Steel, Potentiodynamic Corrosion Tests, Pitting Corrosion Resistance

1. INTRODUCTION

Oxide dispersion strengthened (ODS) ferritic steels belongs to the group of stainless steels with very good creep properties and oxidation resistance (Hoelzer et al., 2000). This is due to addition of Y_2O_3 nanoparticles which stabilize the grain size and dislocation motion at elevated temperature. These materials are envisage to be used as claddings for a water-cooling fast breeder nuclear reactor and in a light water reactor as a cross-cutting material for different nuclear systems or as a tubular heat exchanger. Despite numerous attempts, the powder metallurgy (PM) route is the remains the only method of producing the ODS ferritic alloys. Residual porosity always presented in such kind of materials as well as excess oxygen content may have an influence of their corrosion properties.

It is well known that the corrosion resistance in aquatic environment depends on the chromium concentration in steels (Cho et al., 2004; Ukai et al., 1998), due to the formation of Cr_2O_3 passive layer that suppress and slows the corrosion rate, as well as that the austenitic stainless steels exhibit better corrosion resistance in comparison with the ferritic stainless steels. This is due to the higher Cr, Ni and Mo content commonly used in austenitic steels production that stabilize the face-centered cubic (fcc) structure and reduces the risk of crevice and pitting corrosion (Ollivier-Leduc et al., 2011). Nickel and molybdenum addition for the ODS ferritic steels is forbidden when applying this material in new generation of fusion and fission power plant reactors. The molybdenum increases corrosion resistant properties of the stainless steels, particularly pitting and crevice corrosion in chloride environments. Absence of Ni, may influence the corrosion resistance of the ODS ferritic steel by accelerating localized corrosion. Also, very important issue is carbon, oxygen and nitrogen content in the stainless steels since these elements create the chromium-rich precipitations which noticeably diminish the steels ability to passivation.

The advantage of using the ODS ferritic steels in the nuclear reactor application, instead of the austenitic stainless steels, is their superior thermal stability (a lower thermal expansion coefficient), significant irradiation resistance and comparable thermal conductivity. On the contrary, the 316 stainless steels have superior welding characteristics and fracture toughness at cryogenic temperatures.

Since, the literature data about corrosion resistance of the ODS ferritic steels in aquatic environment is very limited, the potentiodynamic corrosion tests of these grade of materials were performed here. The obtained results were compared with the conventional austenitic stainless steel 316 LV.

2. EXPERIMENTAL PROCEDURE

The ODS ferritic steel was prepared by mechanical alloying (MA) in a planetary ball mill from a pre-alloyed, argon atomised Fe-14Cr-2W-0.3Ti (in wt.%) powder with 0.3% Y_2O_3 nanoparticles under hydrogen atmosphere (Oksiuta 2011). Further consolidation consisted of hot isostatic pressing (HIP) followed by an annealing at 850°C for 1h in argon, and cooling slowly with furnace up to ambient temperature. The density of ODS ferritic steel after HIPping was about 99.0% of theoretical density (ρ_t = 7830 kg/m³) and residual pores were observed. The austenitic stainless steel, AISI 316 LV grade (ASTM F899-12b Standard Specification) was in as-received state. The chemical composition of both materials is summarised in Tab. 1. Three specimens for each material, with a size of 10 mm in diameter and 5 mm thickness were surface grounded using abrasive paper #2400 and mechanically polished with an alumina suspension and ultrasonically cleaned in acetone then ethanol and dried.

The corrosion behaviour of tested materials was determined

by potentiodynamic polarization method by means of the VoltaLab 21 set equipped with Volta Master 4 software. Using the software the value of the corrosion potential (E_{cor}), the current corrosion density (I_{cor}, Tafel method according to the first Stern equation), the corrosion resistance (Rp), the breakdown (pitting) potential (E_b) and the corrosion rate (C_R) were determined. For this purpose, a three-electrode electro-chemical cell was used with the saturated calomel reference electrode (SCE) and comparative platinum counter electrode with an area of contact equal to 128 mm². The contact area of the material exhibited to the test was 28.3 mm². The samples were polarized in the potential range of about -1 V to 4 V with set rise of potential rate of 1 mV/s. An open circuit potential of steels was studied after one hour of exposure, but due to the unstable potential, the time of the study was extended up to 24 hours. Corrosion tests were performed in a physiological saline solution at the temperature of 37±1°C.

Tab. 1. Chemical composition of the ODS ferritic steel (wt.%)

Steel	Cr	W	Mo	Ti	Mn	Ni	O	C	Si
ODS	13.5	1.9	0.02	0.32	0.38	0.13	0.2	0.043	0.35
316L	16.5	-	2.25	0.01	1.87	10.6	0.01	0.030	0.5

3. RESULTS AND DISCUSSION

General microstructure of the ODS ferritic steel is presented in Fig. 1a and 1b. The ODS steel has a ferritic (bcc) structure with precipitations, mainly chromium oxides as well as the larger pores. From OM image the prior particle grains (PPG) with the size of about 45 μm were observed, what correspond well with an average powder particle size measured after mechanical alloying of the ODS steel powder (Oksiuta et al., 2011). The oxide precipitations were also clearly observed on a cross section of the ODS steel, mainly decorated grain boundaries (see Fig. 1c).
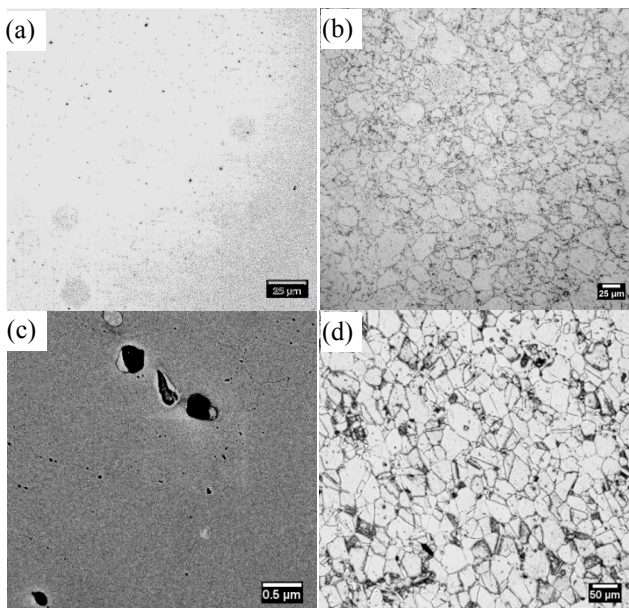

Fig. 1. Microstructure of the tested steels; a) porosity on the polished surface of the ODS ferritic steel, b) OM image of the ODS ferritic steel after etching, c) SEM image of oxide precipitations and d) OM image of the 316 LV steel

The austenitic stainless steel in as-received state has a typical fcc-phase structure with an average grain size of ~35 μm and twins as well as chromium carbide precipitations (see Fig. 1d).

Typical potentiodynamic polarization curves of both steels are shown in Fig. 2, and the mean values of the polarization data are summarized in Table 2 (average of the three specimens).

The results of polarization tests of both materials show a large active peak consisting of a low current passive region for the scan performed towards the higher potential direction. The corrosion potential at active area is slightly noble for the ODS ferritic steel in comparison with the 316 LV counterpart. The anodic peak at approximately -420 mV can be attributed to the oxidation of Cr to the thermodynamically more stable form of Cr^{3+} (Carmezim et al., 2005).

Tab. 2. Electrochemical parameters calculated from the polarization tests of the ODS ferritic and 316 LV steels

Steel	E_{corr} [V]	R_P [kΩcm²]	i_{corr} [μA/cm²]	C_R [μm/Y]	E_P [V]
ODS	−0.375	6.54	4.115	46.885	1.107
316 L	−0.427	47.95	0.711	8.319	0.504
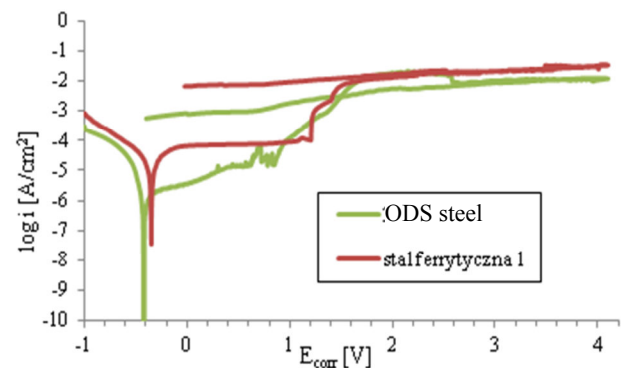
Fig. 2. Typical example of the potentiodynamic polarization curves measured on the ODS and 316 LV steels

On the contrary, the current density in the passive region is significantly higher for the ODS ferritic alloy, however this material exhibits better the breakdown potential value ~1.107 V. A flat shape of the curve running in the passive area, contrary to the 316 LV steel (see Fig. 2), revealed that an oxide film in the ferritic steel is more protective than in the austenitic one, where a continuous chromium oxidation process takes place. For 316 LV a typical potential value for the austenitic stainless steels of about 0.5 V was measured. Interestingly, above these breakdown potentials both materials show fast increase in the current density which is characteristic to the transpassive oxidation of chromium from Cr^{3+} to CrO_4^{2-} (Tyurin, 2003). When the corrosion potential reaches a value of ~1.6 V, the passive state with a current plateau of both materials was achieved up to ~4 V where the test was interrupted and the reverse scan was begun. It is worth to note that no repassivation potential for both tested alloys was observed.

The 316 LV steel has more than seven times higher corrosion resistance (R_P) and six times reduced the mean corrosion rate value (C_R), in comparison with the ODS alloy tested at the same conditions, (see Table 2). This is probably due to different chemi-

cal composition (Cr, Ni, Mo and O content) and the presence of the large chromium oxides observed at the grain boundaries of the ODS steel.

The surface morphology of the tested samples exposed in the saline solution for 24 h is shown in Fig. 3.
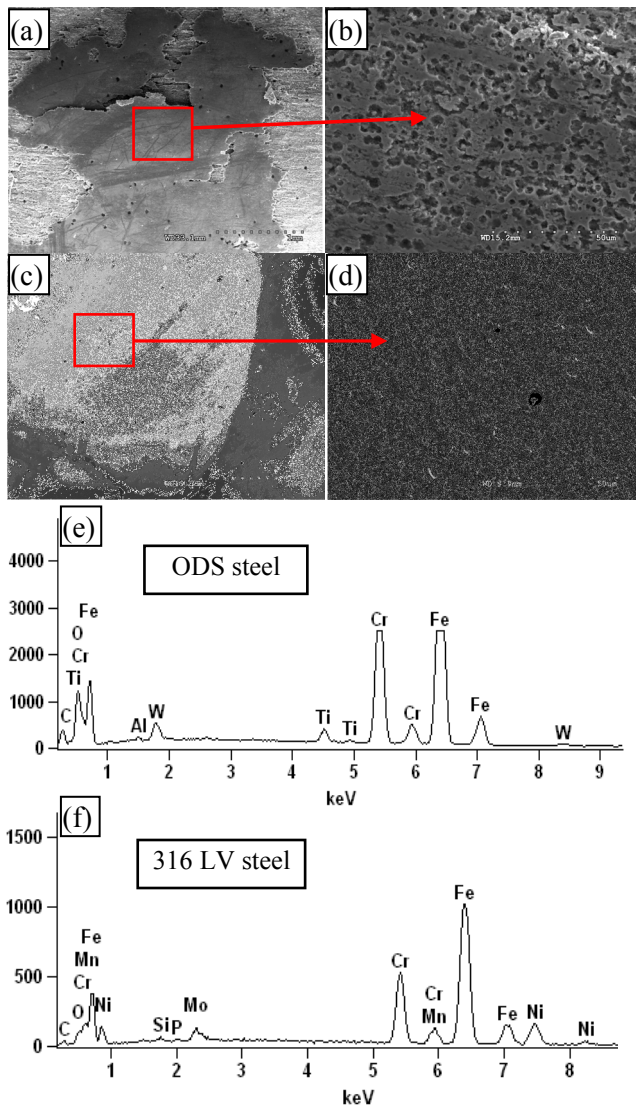
Fig. 3. SEM images of the surface of both materials after corrosion tests:
a) and b) the ODS ferritic steel after 24 h of exposure time,
c) and d) the 316LV stainless steel exposure for 24 h
and e) and f) the SEM-EDS analysis of the ODS
and 316 LV steels, respectively

Short time of exposure (for 1 h) in the physiological saline solution did not cause any changes on the surface of the ODS steel (results not presented here). SEM images, completed by EDS analysis revealed, that after exposures for 1 h singular pits covered the surface of the ODS steel. In contrast, a fast corrosion rate was developed for 24 h of exposure. After a prolonged exposing time, a broken oxide scale on the surface of the ODS specimen was clearly visible (see Fig. 3b), and a large number density of small localized corrosion cavities (up to 5 μm in diameter), penetrating grain boundaries, which were the most active corrosion areas, were observed. The SEM-EDS analysis also revealed that the scale consisted of complex Cr-Ti-rich oxide layer and did not show significant variation in the chemical composition. Also,

it should be emphasize that the oxide layer on the ODS steel was fragile and had poor adhesion to the ferritic steel substrate what was also confirmed by the observations of the corrosion products found in the saline solution.

There is a distinct contrast between the surface morphology formed on the 316 LV and ODS ferritic steel tested at similar corrosion conditions. For the 316 LV steel two kinds of corrosion pits can be distinguished. Low magnification SEM images in Fig. 3c revealed larger pits with an average size of ~25 μm in diameter and with low number density of ~2.0×10^4/m^2. The second type of pits, observed at higher magnification in Fig. 3d, has shallow and more uniform morphology, which looks like a general corrosion, equally covering the entire area of the specimen. This may lead to the assumption that austenitic steel has not uniform distribution of the main alloying elements and their segregation can locally cause severe oxidation and pitting corrosion attack. This is in a good accordance with observations of a steady increase in the current density in the passive region of the 316 LV steel.

Nevertheless, it seems that from the electrochemical point of view, comparative analysis shown that better corrosion resistance has the 316 LV steel than the ODS ferritic alloy since the former material exhibits lower current density and the corrosion rate values. This is mainly due to the higher amount of corrosion protective elements, such as Cr, Ni and Mo used for production the austenitic steel and lower oxygen content.

The results presented here also shown that the main type of damage observed on the surface of both materials after corrosion testing is pitting. Resistance of the steels to this kind of corrosion can be predicted from the chemical composition of tested materials by means of the pitting resistance equivalent (PRE) parameter expressed as (Kim et al., 2002):

$$PRE = \%Cr + 3.3\%(Mo + 0.5W) + 16\%N \qquad (1)$$

The higher the PRE parameter the better pitting corrosion resistance of the steels. Calculated from Eq. (1) the PRE parameter exhibited ~42% higher value for the 316 LV steel in comparison with the ODS alloy, 24.4% and 16.8%, respectively. This confirms why the 316 LV steel demonstrate better pitting corrosion resistance than the ODS ferritic steel.

4. SUMMARY

The potentiodynamic corrosion resistance of the ODS ferritic steel and 316 LV austenitic stainless steels was studied. As expected, the results presented in this work shown that better corrosion resistance has austenitic stainless steel, due to larger content of the pitting protective alloying elements. However, the 316 LV steel has the lower breakdown potential than the ODS ferritic steel and the unstable shape of the curve running in the passive region, which means that the surface of the former alloy is undergoing a slow oxidation process.

The microstructural characterization of the surface layer after corrosion tests revealed that there is a distinct difference between the surface morphology of both alloys. A broken oxide scale with poor adhesion to the ferritic steel matrix and with a large number density of localized corrosion attack was observed on the surface of the ODS ferritic steel. Shallow and more uniform pits with a surface looking more like a general corrosion were observed on

the surface of the 316 LV austenitic steel. However, in this material singular, deeper pits were also detected.

Despite the higher current density as well as the higher corrosion rate measured for the ODS ferritic steel this alloy manufactured by means of PM route exhibited a quite good corrosion resistance. To improve pitting corrosion resistance in this alloy the oxygen content should be reduced, what can decrease the number density of the oxide precipitations located at the grain boundaries.

REFERENCES

1. **ASTM F899-12b** Standard Specification for Wrought Stainless Steels for Surgical Instruments.
2. **Carmezim M. J.** (2005), Capacitance behaviour of passive films on ferritic and austenitic stainless steel, *Corrosion Science*, No. 47, 581–591.
3. **Cho H. S. et al.** (2004), Corrosion properties of oxide dispersion strengthened steels in super-critical water environment, *Journal of Nuclear Material*s, No. 329–333, 387–391.
4. **Hoelzer D. T et al.** (2000), A microstructural study of the oxide scale formation on ODS Fe13Cr steel, *Journal of Nuclear Materials*, No. 283–287, 1306–1310.
5. **Kim J. S.** (2002), Effect of alloying elements on the contact resistance and the passivation behaviour of stainless steels, *Corrosion Science*, No. 44, 635–655.
6. **Oksiuta Z.** (2011), Microstructural changes of ODS ferritic steel powder during mechanical alloying, *Acta Mechanica et Automatica*, Vol. 5, No. 2, 74–78.
7. **Oksiuta Z. et al.** (2011), Influence of Y_2O_3 and Fe_2Y additions on the formation of nano-scale oxide particles and the mechanical properties of an ODS RAF steel, *Fusion Engineering and Design*, No. 86, 2417–2420.
8. **Ollivier-Leduc A.** (2011), Study of selective oxidation by means of glow discharge optical emission spectroscopy, *Corrosion Science*, 53 (2011) 1375÷1382.
9. **Tyurin A. G.** (2003), Thermodynamic Assessment of the Effect of Chromium and Molybdenum on the Passivability of Nickel-Base Alloys, *Protection of Metals*, Vol. 39, No. 6, 568–574.
10. **Ukai S. et al.** (1998), R&D of oxide dispersion strengthened ferritic martensitic steels for FBR, *Journal of Nuclear Materials,* No. 258–263, 1745–1749.

POSITIVE MINIMAL REALIZATION OF CONTINUOUS-DISCRETE LINEAR SYSTEMS WITH ALL-POLE AND ALL-ZERO TRANSFER FUNCTION

Łukasz SAJEWSKI*

*Faculty of Electrical Engineering, Białystok University of Technology, ul. Wiejska 45D, 15-351 Białystok, Poland

l.sajewski@pb.edu.pl

Abstract: The positive and minimal realization problem for continuous-discrete linear single-input and single-outputs (SISO) systems is formulated. Two special case of the continuous-discrete systems are given. Method based on the state variable diagram for finding a positive and minimal realization of a given proper transfer function is proposed. Sufficient conditions for the existence of a positive minimal realization of a given proper transfer function of all-pole and all-zero systems are established. Two procedures for computation of a positive minimal realization are proposed and illustrated by a numerical examples.

Keywords: Continuous-Discrete, 2D, Minimal, Positive, Realization, Existence, Computation

1. INTRODUCTION

In positive systems inputs, state variables and outputs take only non-negative values. Examples of positive systems are industrial processes involving chemical reactors, heat exchangers and distillation columns, storage systems, compartmental systems, water and atmospheric pollution models. A variety of models having positive linear systems behavior can be found in engineering, management science, economics, social sciences, biology and medicine, etc. Positive linear systems are defined on cones and not on linear spaces. Therefore, the theory of positive systems is more complicated and less advanced. An overview of state of art in positive systems theory is given in the monographs: Farina and Rinaldi (2000), Kaczorek (2002). The realization problem for positive discrete-time and continuous-time systems without and with delays was considered in Kaczorek and Busłowicz (2004), Kaczorek (2004, 2005, 2006a, 2006b).

Continuous-discrete 2D linear system is a dynamic system that incorporate both continuous-time and discrete-time dynamics. It means that state vector of 2D system contain continuous-time state variables and discrete-time state variables, input and output vectors depends on continuous time t and discrete steps i. Examples of continuous-discrete systems include systems with relays, switches, and hysteresis, transmissions, and other motion controllers, constrained robotic systems, automated highway systems, flight control and management systems, analog/digital circuit. The positive continuous-discrete 2D linear systems have been introduced in Kaczorek (2002), positive hybrid linear systems in Kaczorek (2007) and the positive fractional 2D hybrid systems in Kaczorek (2008a). Different methods of solvability of 2D hybrid linear systems have been discussed in Kaczorek et al. (2008) and the solution to singular 2D hybrids linear systems has been derived in Sajewski (2009). The realization problem for positive 2D hybrid systems have been addressed in Kaczorek (2002, 2008b), Sajewski and Kaczorek (2009, 2010) and the minimal realization problem for all-pole (the transfer function with only poles) and all-zero (the transfer function with all zero

poles) 2D systems has been addressed in Antoniou (2002) and Varoufakis et al. (1987).

The main purpose of this paper is to present a method for computation of a positive and minimal realization of a given proper transfer function of all-pole and all-zero continuous-discrete linear system. Proposed method is based on the state variable diagram method. Sufficient conditions for the existence of a positive minimal realization of a given proper transfer function of all-pole and all-zero system will be established and a procedures for computation of a positive minimal realization for two cases of transfer functions will be proposed. The paper is organized as follows. In section 2 some preliminaries concerning the positive continuous-discrete 2D linear systems and minimal realization are recalled and the positive minimal realization is formulated. Two special cases of continuous-discrete systems are recalled in section 3. In the same section the solution to the positive minimal realization problem for two cases of transfer function are presented and the sufficient conditions for existence of positive minimal realization are derived. Concluding remarks are given in section 4.

To the best author knowledge the positive minimal realization problem for continuous-discrete 2D linear systems have not been considered yet.

In the paper the following notation will be used. The set of $n \times m$ real matrices will be denoted by $\Re^{n \times m}$ and $\Re^n = \Re^{n \times 1}$. The set of $n \times m$ real matrices with nonnegative entries will be denoted by $\Re_+^{n \times m}$ and $\Re_+^n = \Re_+^{n \times 1}$. M_n be the set of $n \times m$ Metzler matrices (real matrices with nonnegative off-diagonal entries). The $n \times n$ identity matrix will be denoted by I_n and the transpose will be denoted by T.

2. PRELIMINARIES AND PROBLEM FORMULATION

Consider a continuous-discrete linear system described by the equations (Kaczorek, 2002):

$$\dot{x}_1(t,i) = A_{11}x_1(t,i) + A_{12}x_2(t,i) + B_1u(t,i) \qquad (1a)$$

$$t \in \Re_+ = [0, +\infty]$$

$$x_2(t, i+1) = A_{21} x_1(t, i) + A_{22} x_2(t, i) + B_2 u(t, i) \tag{1b}$$

$$i \in Z_+$$

$$y(t, i) = C_1 x_1(t, i) + C_2 x_2(t, i) + Du(t, i) \tag{1c}$$

where: $\dot{x}_1(t, i) = \frac{\partial x_1(t, i)}{\partial t}$, $x_1(t, i) \in \Re^{n_1}$, $x_2(t, i) \in \Re^{n_2}$, $u(t, i) \in \Re^m$, $y(t, i) \in \Re^p$ and $A_{11} \in M_{n_1}$, $A_{12} \in \Re^{n_1 \times n_2}$, $A_{21} \in \Re^{n_2 \times n_1}$, $A_{22} \in \Re^{n_2 \times n_2}$, $B_1 \in \Re^{n_1 \times m}$, $B_2 \in \Re^{n_2 \times m}$, $C_1 \in \Re^{p \times n_1}$, $C_2 \in \Re^{p \times n_2}$, $D \in \Re^{p \times m}$ are real matrices.

Boundary conditions for (1a) and (1b) have the form:

$$x_1(0, i) = x_1(i), \ i \in Z_+ \ \text{and} \ x_2(t, 0) = x_2(t), \ t \in \Re_+ \tag{2}$$

Note that the continuous-discrete linear system (1) has a similar structure as the Roesser model (Kaczorek, 2007; Roesser, 1975).

Definition 2.1. The continuous-discrete linear system (1) is called internally positive if $x_1(t, i) \in \Re_+^{n_1}$, $x_2(t, i) \in \Re_+^{n_2}$ and $y(t, i) \in \Re_+^p$, $t \in \Re_+$, $i \in Z_+$ for all arbitrary boundary conditions $x_1(i) \in \Re_+^{n_1}$, $i \in Z_+$, $x_2(t) \in \Re_+^{n_2}$, $t \in \Re_+$ and all inputs $u(t, i) \in \Re_+^m$, $t \in \Re_+$, $i \in Z_+$.

Theorem 2.1. (Kaczorek, 2002; 2007) The continuous-discrete linear system (1) is internally positive if and only if:

$$A_{11} \in M_{n_1}, \ A_{12} \in \Re_+^{n_1 \times n_2}, \ A_{21} \in \Re_+^{n_2 \times n_1}, \ A_{22} \in \Re_+^{n_2 \times n_2},$$

$$B_1 \in \Re_+^{n_1 \times m}, \ B_2 \in \Re_+^{n_2 \times m}, \ C_1 \in \Re_+^{p \times n_1}, \ C_2 \in \Re_+^{p \times n_2}, \tag{3}$$

$$D \in \Re_+^{p \times m}.$$

The transfer matrix of the system (1) is given by the formula:

$$T(s, z) = \begin{bmatrix} C_1 & C_2 \end{bmatrix} \begin{bmatrix} I_{n_1} s - A_{11} & -A_{12} \\ -A_{21} & I_{n_2} z - A_{22} \end{bmatrix}^{-1} \begin{bmatrix} \overline{B}_1 \\ \overline{B}_2 \end{bmatrix}$$
$$+ D \in \Re^{p \times m}(s, z) \tag{4}$$

where $\Re^{p \times m}(s, z)$ is the set of $p \times m$ real matrices in s and z with real coefficient. Considering the m-inputs and p-outputs continuous-discrete linear system (1), the proper transfer matrix will be having the following form:

$$T(s, z) = \begin{bmatrix} T_{11}(s, z) & \dots & T_{1m}(s, z) \\ \vdots & \vdots & \vdots \\ T_{p1}(s, z) & \dots & T_{pm}(s, z) \end{bmatrix} \in \Re^{p \times m}(s, z) \tag{5a}$$

where:

$$T_{kl}(s, z) = \frac{Y_{kl}(s, z)}{U_{kl}(s, z)} = \frac{\sum\limits_{i=0}^{n_{kl}} \sum\limits_{j=0}^{m_{kl}} b_{i,j}^{kl} s^i z^j}{s^{n_{kl}} z^{m_{kl}} - \left(\sum\limits_{\substack{i=0 \\ i+j \neq n_{kl}+m_{kl}}}^{n_{kl}} \sum\limits_{j=0}^{m_{kl}} a_{i,j}^{kl} s^i z^j \right)} \tag{5b}$$

For $k = 1, 2, \dots, p$; $l = 1, 2, \dots, m$ where $U(s, z) = Z\{L[u(t, i)]\}$, $y(s, z) = Z\{L[y(t, i)]\}$ and Z and L are the zet and Laplace operators.

Multiplying the numerator and denominator of transfer matrix (5b) by $s^{-n_{1,kl}} z^{-n_{2,kl}}$ we obtain the transfer matrix in the state space form eg. form which is needed to draw the state space diagram (Kaczorek, 1992; Roesser, 1975; Sajewski and Kaczorek, 2010):

$$T_{kl}(s^{-1}, z^{-1}) = \frac{\sum\limits_{i=0}^{n_{1,kl}} \sum\limits_{j=0}^{n_{2,kl}} b_{i,j}^{kl} s^{-i} z^{-j}}{s^{-n_{1,kl}} z^{-n_{2,kl}} - \left(\sum\limits_{\substack{i=0 \\ i+j \neq n_{1,kl}+n_{2,kl}}}^{n_{1,kl}} \sum\limits_{j=0}^{n_{2,kl}} a_{i,j}^{kl} s^{-i} z^{-j} \right)} \tag{6}$$

for $k = 1, 2, \dots, p$; $l = 1, 2, \dots, m$.

Definition 2.2. The matrices (3) are called the positive realization of the transfer matrix $T(s, z)$ if they satisfy the equality (4). The realization is minimal if the matrix A have lowest possible dimension among all realizations. For given transfer matrix there exist many sets of matrices A, B C, D but for given matrices A, B C, D there exist only one transfer function.

The positive minimal realization problem can be stated as follow.

Given a proper rational matrix $T(s, z) \in \Re^{p \times m}(s, z)$, find its positive and minimal realization (3).

Taking under considerations Definition 2.2 and e.g. similarity transformation [8, 9] the solution to the realization problem given in Section 3 is not unique.

Remark 2.1. For 1D systems the minimal realization is the one with the matrix A of dimension $n \times n$ where n is the degree of the characteristic polynomial of the system (Kaczorek, 1992). This was implicated by controllability and observability of the 1D system. For 2D system in general case this relationship is not true (Sun-Yuan et al., 1977) and observability connected with controllability of the 2D system does not implicate the minimality of its realization.

Remark 2.2. The minimal realization for 2D system is the one with the matrix A of dimension $(n_1 + n_2) \times (n_1 + n_2)$ where n_1 and n_2 are the degrees of the characteristic polynomial in s and z of the system (Sun-Yuan et al., 1977).

3. PROBLEM SOLUTION FOR SISO SYSTEMS

The solution to the minimal positive realization problem will be presented on two special cases of the 2D transfer functions ($m = p = 1$). Proposed method will be based on state variable diagram (Kaczorek, 2002; Sajewski and Kaczorek, 2010). Lets consider the following two cases of the transfer functions of continuous-discrete linear system.

Case 1. The transfer function of all-pole system (which is the transfer function with only poles):

$$T(s^{-1}, z^{-1}) = \frac{b}{1 - \sum\limits_{\substack{i=0 \\ i+j \neq 0}}^{n_1} \sum\limits_{j=0}^{n_2} a_{i,j} s^{-i} z^{-j}} = \frac{Y}{U} \tag{7}$$

where b is the real coefficient.

Case 2. The transfer function of all-zero system (which is the transfer function with all zero poles):

$$T(s^{-1}, z^{-1}) = \frac{\sum\limits_{i=0}^{n_1} \sum\limits_{j=0}^{n_2} b_{i,j} s^{-i} z^{-j}}{1} = \frac{Y}{U} \tag{8}$$

3.1. Case 1

Defining:

$$E = \frac{U}{1 - a_{n_1,n_2-1}z^{-1} - a_{n_1-1,n_2}s^{-1} - ... - a_{00}s^{-n_1}z^{-n_2}} \quad (9)$$

from (7) we obtain:

$$E = U + (a_{n_1,n_2-1}z^{-1} + a_{n_1-1,n_2}s^{-1} + ... + a_{00}s^{-n_1}z^{-n_2})E, \quad (10)$$
$$Y = bE.$$

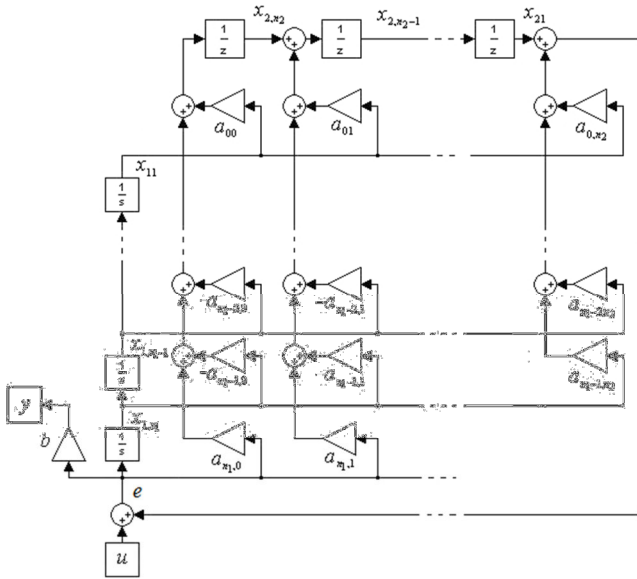Using (10) we may draw the state variable diagram shown on Fig. 1.

Fig. 1. State variable diagram for transfer function (7) of all-pole system

As a state variable we choose the outputs of integrators $(x_{1,1}(t,i),\ x_{1,2}(t,i),...,x_{1,n_1}(t,i))$ and of delay elements $((x_{2,1}(t,i),\ x_{2,2}(t,i),...,x_{2,n_2}(t,i))$. Using state variable diagram (Fig. 1) we can write the following differential and difference equations:

$$\dot{x}_{1,1}(t,i) = x_{1,2}(t,i),$$
$$\dot{x}_{1,2}(t,i) = x_{1,3}(t,i),$$
$$\vdots$$
$$\dot{x}_{1,n_1-1}(t,i) = x_{1,n_1}(t,i),$$
$$\dot{x}_{1,n_1}(t,i) = e(t,i),$$
$$x_{2,1}(t,i+1) = a_{0,n_2-1}x_{1,1}(t,i) + a_{1,n_2-1}x_{1,2}(t,i) + ...$$
$$+ a_{n_1-1,n_2-1}x_{1,n_1}(t,i) + x_{2,2}(t,i) + a_{n_1,n_2-1}e(t,i),$$
$$x_{2,2}(t,i+1) = a_{0,n_2-2}x_{1,1}(t,i) + a_{1,n_2-2}x_{1,2}(t,i) + ...$$
$$+ a_{n_1-1,n_2-2}x_{1,n_1}(t,i) + x_{2,3}(t,i) + a_{n_1,n_2-2}e(t,i),$$
$$\vdots$$
$$x_{2,n_2-1}(t,i+1) = a_{0,1}x_{1,1}(t,i) + a_{1,1}x_{1,2}(t,i) + ...$$
$$+ a_{n_1-1,1}x_{1,n_1}(t,i) + x_{2,n_2}(t,i) + a_{n_1,1}e(t,i),$$

(11a)

$$x_{2,n_2}(t,i+1) = a_{0,0}x_{1,1}(t,i) + a_{1,0}x_{1,2}(t,i) + ...$$
$$+ a_{n_1-1,0}x_{1,n_1}(t,i) + a_{n_1,0}e(t,i), \quad (11b)$$
$$y(t,i) = be(t,i),$$

where:

$$e(t,i) = a_{0,n_2}x_{1,1}(t,i) + a_{1,n_2}x_{1,2}(t,i) + ...$$
$$+ a_{n_1-1,n_2}x_{1,n_1}(t,i) + x_{2,1}(t,i) + u(t,i). \quad (11c)$$

Substituting (11b) into (11a) we obtain:

$$\dot{x}_{1,1}(t,i) = x_{1,2}(t,i),$$
$$\dot{x}_{1,2}(t,i) = x_{1,3}(t,i),$$
$$\vdots$$
$$\dot{x}_{1,n_1-1}(t,i) = x_{1,n_1}(t,i),$$
$$\dot{x}_{1,n_1}(t,i) = a_{0,n_2}x_{1,1}(t,i) + a_{1,n_2}x_{1,2}(t,i) + ...$$
$$+ a_{n_1-1,n_2}x_{1,n_1}(t,i) + x_{2,1}(t,i) + u(t,i),$$
$$x_{2,1}(t,i+1) = \bar{a}_{0,n_2-1}x_{1,1}(t,i) + \bar{a}_{1,n_2-1}x_{1,2}(t,i)$$
$$+ a_{n_1,n_2-1}u(t,i) + ... + \bar{a}_{n_1-1,n_2-1}x_{1,n_1}(t,i)$$
$$+ a_{n_1,n_2-1}x_{2,1}(t,i) + x_{2,2}(t,i),$$

(12a)

$$\vdots$$
$$x_{2,m-1}(t,i+1) = \bar{a}_{0,1}x_{1,1}(t,i) + \bar{a}_{1,1}x_{1,2}(t,i) + ...$$
$$+ \bar{a}_{n_1-1,1}x_{1,n_1}(t,i) + a_{n_1,1}x_{2,1}(t,i) + x_{2,m}(t,i) + a_{n_1,1}u(t,i),$$
$$x_{2,m}(t,i+1) = \bar{a}_{0,0}x_{1,1}(t,i) + \bar{a}_{1,0}x_{1,2}(t,i) + ...$$
$$+ \bar{a}_{n_1-1,0}x_{1,n_1}(t,i) + a_{n_1,0}x_{2,1}(t,i) + a_{n_1,0}u(t,i),$$
$$y(t,i) = ba_{0,n_2}x_{1,1}(t,i) + ba_{1,n_2}x_{1,2}(t,i) + ...$$
$$+ ba_{n_1-1,n_2}x_{1,n_1}(t,i) + bx_{2,1}(t,i) + bu(t,i),$$

where:

$$\bar{a}_{i,j} = a_{i,j} + a_{i,n_2}a_{n_1,j}$$
for $i = 0,1,...,n_1-1,\ j = 0,1,...,n_2-1$ (12b)

Defining state vectors in the form:

$$x_1(t,i) = \begin{bmatrix} x_{1,1}(t,i) \\ \vdots \\ x_{1,n_1}(t,i) \end{bmatrix}, \quad x_2(t,i) = \begin{bmatrix} x_{2,1}(t,i) \\ \vdots \\ x_{2,n_2}(t,i) \end{bmatrix} \quad (13)$$

we can write the equations (12) in the form:

$$\begin{bmatrix} \dot{x}_1(t,i) \\ x_2(t,i+1) \end{bmatrix} = \begin{bmatrix} A_{11} & A_{12} \\ A_{21} & A_{22} \end{bmatrix} \begin{bmatrix} x_1(t,i) \\ x_2(t,i) \end{bmatrix} + \begin{bmatrix} B_1 \\ B_2 \end{bmatrix} u(t,i),$$
$$y(t,i) = \begin{bmatrix} C_1 & C_2 \end{bmatrix} \begin{bmatrix} x_1(t,i) \\ x_2(t,i) \end{bmatrix} + Du(t,i), \quad (14)$$

where:

$$A_{11} = \begin{bmatrix} 0 & 1 & 0 & ... & 0 \\ 0 & 0 & 1 & ... & 0 \\ \vdots & \vdots & \vdots & \ddots & \vdots \\ 0 & 0 & 0 & ... & 1 \\ a_{0,n_2} & a_{1,n_2} & a_{2,n_2} & ... & a_{n_1-1,n_2} \end{bmatrix} \in \Re^{n_1 \times n_1}, \quad (15)$$

$$A_{12} = \begin{bmatrix} 0 & 0 & ... & 0 \\ \vdots & \vdots & ... & \vdots \\ 0 & 0 & ... & 0 \\ 1 & 0 & ... & 0 \end{bmatrix} \in \Re^{n_1 \times n_2},$$

$$A_{21} = \begin{bmatrix} \overline{a}_{0,n_2-1} & ... & \overline{a}_{n_1-1,n_2-1} \\ \vdots & ... & \vdots \\ \overline{a}_{0,0} & ... & \overline{a}_{n_1-1,0} \end{bmatrix} \in \Re^{n_2 \times n_1},$$

$$A_{22} = \begin{bmatrix} a_{n_1,n_2-1} & 1 & 0 & ... & 0 \\ a_{n_1,n_2-2} & 0 & 1 & ... & 0 \\ \vdots & \vdots & \vdots & \ddots & \vdots \\ a_{n_1,1} & 0 & 0 & ... & 1 \\ a_{n_1,0} & 0 & 0 & ... & 0 \end{bmatrix} \in \Re^{n_2 \times n_2}$$

$$B_1 = \begin{bmatrix} 0 \\ \vdots \\ 0 \\ 1 \end{bmatrix} \in \Re^{n_1 \times 1}, \quad B_2 = \begin{bmatrix} a_{n_1,n_2-1} \\ a_{n_1,n_2-2} \\ \vdots \\ a_{n_1,0} \end{bmatrix} \in \Re^{n_2 \times 1},$$

$$C_1 = [ba_{0,n_2} \quad ... \quad ba_{n_1-1,n_2}] \in \Re^{1 \times n_1},$$

$$C_2 = [b \quad 0 \quad ... \quad 0] \in \Re^{1 \times n_2}, \quad D = [b] \in \Re^{1 \times 1}. \tag{15}$$

Therefore, the following theorem has been proved.

Theorem 3.1. There exists a positive realization of dimension $(n_1 + n_2) \times (n_1 + n_2)$ if the system is all-pole and all coefficients of the nominator and denominator of the transfer function (7) are nonnegative.

If the assumptions of Theorem 3.1 are satisfied then a positive realization (3) of (7) can be found by the use of the following procedure.

Procedure 3.1.
Step 1. Write the transfer function (7) in the form (10).
Step 2. Using (10) draw the state variable diagram shown in Fig. 1.
Step 3. Choose the state variables and write equations (12).
Step 4. Using (12) find the desired realization (15) of transfer function (7).

Example 3.1. Find a positive realization (3) of the all-pole continuous-discrete system with proper transfer function:

$$T(s^{-1}, z^{-1}) = \frac{2}{1 - 0.5z^{-1} - 0.4s^{-1} - 0.3s^{-1}z^{-1} - 0.2s^{-2} - 0.1s^{-2}z^{-1}}. \tag{16}$$

In this case $n_1 = 2$ and $n_2 = 1$.

Using Procedure 3.1 we obtain the following.

Step 1. Transfer function (16) can be written as:

$$E = U + (0.5z^{-1} + 0.4s^{-1} + 0.3s^{-1}z^{-1} + 0.2s^{-2} + 0.1s^{-2}z^{-1})E,$$

$$Y = 2E. \tag{17}$$

Step 2. State variable diagram has the form shown on Fig. 2.

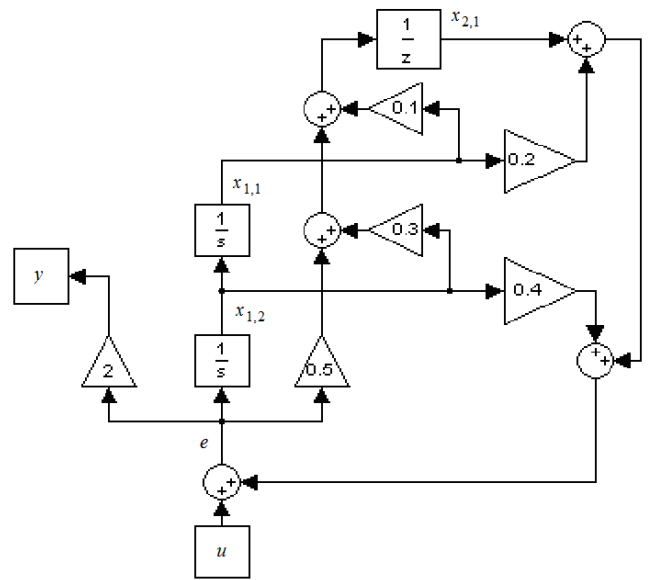**Fig. 2.** State space diagram for transfer function (16)

Step 3. Using state variable diagram we can write the following equations:

$$\dot{x}_{1,1}(t,i) = x_{1,2}(t,i),$$

$$\dot{x}_{1,2}(t,i) = 0.2x_{1,1}(t,i) + 0.4x_{1,2}(t,i) + x_{2,1}(t,i) + u(t,i),$$

$$x_{2,1}(t,i+1) = 0.2x_{1,1}(t,i) + 0.5x_{1,2}(t,i) \tag{18}$$
$$\qquad + 0.5x_{2,1}(t,i) + 0.5u(t,i),$$

$$y(t,i) = 0.4x_{1,1}(t,i) + 0.8x_{1,2}(t,i) + 2x_{2,1}(t,i) + 2u(t,i).$$

Step 4. The desired realization of (16) has the form:

$$A_{11} = \begin{bmatrix} 0 & 1 \\ 0.2 & 0.4 \end{bmatrix}, \quad A_{12} = \begin{bmatrix} 0 \\ 1 \end{bmatrix},$$

$$A_{21} = [0.2 \quad 0.5], \quad A_{22} = [0.5],$$

$$B_1 = \begin{bmatrix} 0 \\ 1 \end{bmatrix}, \quad B_2 = [0.5], \quad C_1 = [0.4 \quad 0.8], \tag{19}$$

$$C_2 = [2], \quad D = [2].$$

Obtained realization have only nonnegative entries and its of minimal dimension.

3.2. Case 2

Defining:

$$Y = (b_{n_1,n_2} + b_{n_1,n_2-1}z^{-1} + b_{n_1-1,n_2}s^{-1}$$
$$+ ... + b_{00}s^{-n_1}z^{-n_2})U \tag{20}$$

we may draw the state variable diagram shown on Fig. 3.

Similarly as in section 3.1 as a state variable we choose the outputs of integrators $(x_{1,1}(t,i),\ x_{1,2}(t,i), ..., x_{1,n_1}(t,i))$ and of delay elements $(x_{2,1}(t,i),\ x_{2,2}(t,i), ..., x_{2,n_2}(t,i))$.
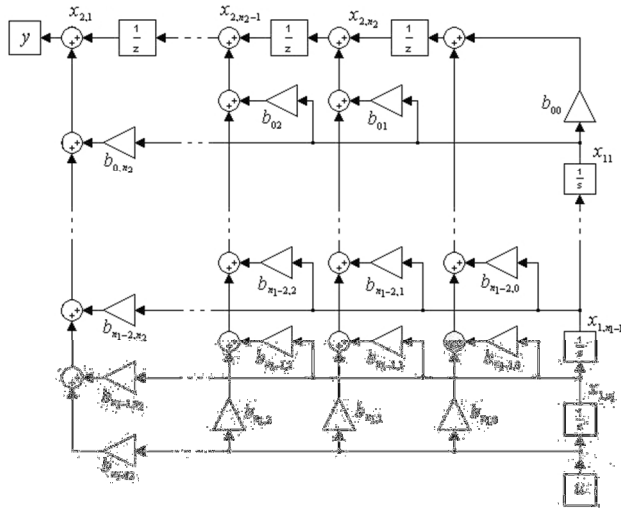
Fig. 3. State space diagram for transfer function (8) of all-zero system

Using state variable diagram (Fig. 3) we can write the following differential and difference equations:

$$\dot{x}_{1,1}(t,i) = x_{1,2}(t,i),$$
$$\dot{x}_{1,2}(t,i) = x_{1,3}(t,i),$$
$$\vdots$$
$$\dot{x}_{1,n_1-1}(t,i) = x_{1,n_1}(t,i),$$
$$\dot{x}_{1,n_1}(t,i) = u(t,i),$$
$$x_{2,1}(t,i+1) = b_{0,n_2-1}x_{1,1}(t,i) + b_{1,n_2-1}x_{1,2}(t,i) + \dots$$
$$\quad + b_{n_1-1,n_2-1}x_{1,n_1}(t,i) + x_{2,2}(t,i) + b_{n_1,n_2-1}u(t,i),$$
$$x_{2,2}(t,i+1) = b_{0,n_2-2}x_{1,1}(t,i) + b_{1,n_2-2}x_{1,2}(t,i) + \dots$$
$$\quad + b_{n_1-1,n_2-2}x_{1,n_1}(t,i) + x_{2,3}(t,i) + b_{n_1,n_2-2}u(t,i), \qquad (21)$$
$$\vdots$$
$$x_{2,n_2-1}(t,i+1) = b_{0,1}x_{1,1}(t,i) + b_{1,1}x_{1,2}(t,i) + \dots$$
$$\quad + b_{n_1-1,1}x_{1,n_1}(t,i) + x_{2,n_2}(t,i) + b_{n_1,1}u(t,i),$$
$$x_{2,n_2}(t,i+1) = b_{0,0}x_{1,1}(t,i) + b_{1,0}x_{1,2}(t,i) + \dots$$
$$\quad + b_{n_1-1,0}x_{1,n_1}(t,i) + b_{n_1,0}u(t,i),$$
$$y(t,i) = b_{0,n_2}x_{1,1}(t,i) + b_{1,n_2}x_{1,2}(t,i) + \dots$$
$$\quad + b_{n_1-1,n_2}x_{1,n_1}(t,i) + x_{2,1}(t,i) + b_{n_1,n_2}u(t,i).$$

Defining state vectors in the form:

$$x_1(t,i) = \begin{bmatrix} x_{1,1}(t,i) \\ \vdots \\ x_{1,n_1}(t,i) \end{bmatrix}, \quad x_2(t,i) = \begin{bmatrix} x_{2,1}(t,i) \\ \vdots \\ x_{2,n_2}(t,i) \end{bmatrix} \qquad (22)$$

we can write the equations (21) in the matrix form (14) where:

$$A_{11} = \begin{bmatrix} 0 & 1 & 0 & \dots & 0 \\ 0 & 0 & 1 & \dots & 0 \\ \vdots & \vdots & \vdots & \ddots & \vdots \\ 0 & 0 & 0 & \dots & 1 \\ 0 & 0 & 0 & \dots & 0 \end{bmatrix} \in \Re^{n_1 \times n_1}, \quad A_{12} = [0] \in \Re^{n_1 \times n_2}, \qquad (23)$$

$$A_{21} = \begin{bmatrix} b_{0,n_2-1} & \dots & b_{n_1-1,n_2-1} \\ \vdots & \dots & \vdots \\ b_{0,0} & \dots & b_{n_1-1,0} \end{bmatrix} \in \Re^{n_2 \times n_1},$$

$$A_{22} = \begin{bmatrix} 0 & 1 & 0 & \dots & 0 \\ 0 & 0 & 1 & \dots & 0 \\ \vdots & \vdots & \vdots & \ddots & \vdots \\ 0 & 0 & 0 & \dots & 1 \\ 0 & 0 & 0 & \dots & 0 \end{bmatrix} \in \Re^{n_2 \times n_2}, \qquad (23)$$

$$B_1 = \begin{bmatrix} 0 \\ \vdots \\ 0 \\ 1 \end{bmatrix} \in \Re^{n_1 \times 1}, \quad B_2 = \begin{bmatrix} b_{n_1,n_2-1} \\ b_{n_1,n_2-2} \\ \vdots \\ b_{n_1,0} \end{bmatrix} \in \Re^{n_2 \times 1},$$

$$C_1 = [b_{0,n_2} \quad \dots \quad b_{n_1-1,n_2}] \in \Re^{1 \times n_1},$$
$$C_2 = [1 \quad 0 \quad \dots \quad 0] \in \Re^{1 \times n_2}, \quad D = [b_{n_1,n_2}] \in \Re^{1 \times 1}.$$

Therefore, the following theorem has been proved.

Theorem 3.2. There exists a positive realization of dimension $(n_1 + n_2) \times (n_1 + n_2)$ if the system is all-zero and all coefficients of the nominator of transfer function (8) are nonnegative. If the assumptions of Theorem 3.2 are satisfied then a positive realization (3) of (8) can be found by the use of the following procedure.

Procedure 3.2.
Step 1. Write the transfer function (8) in the form (20).
Step 2. Using (20) draw the state variable diagram shown in Fig. 3.
Step 3. Choose the state variables and write equations (21).
Step 4. Using (21) find the desired realization (23) of transfer function (8).

Example 3.2. Find a positive realization (3) of the all-zero continuous-discrete system with proper transfer function:

$$T(s,z) = 6s^2z + 5s^2 + 4sz + 3s + 2z + 1 \qquad (24)$$

In this case $n_1 = 2$ and $n_2 = 1$.

Using Procedure 3.2 we obtain the following.
Step 1. Transfer function (24) can by written as:

$$Y = (6 + 5z^{-1} + 4s^{-1} + 3s^{-1}z^{-1} + 2s^{-2} + s^{-2}z^{-1})U \qquad (25)$$

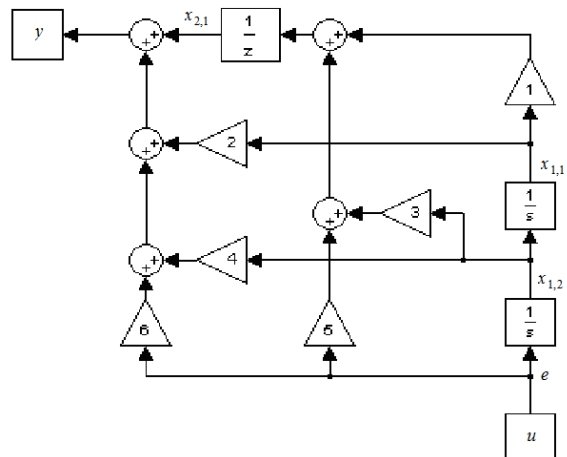Step 2. State variable diagram has the form shown in Fig. 4.

Fig. 4. State space diagram for transfer function (24)

Step 3. Using state variable diagram we can write the following equations:

$$\dot{x}_{1,1}(t,i) = x_{1,2}(t,i),$$
$$\dot{x}_{1,2}(t,i) = u(t,i),$$
$$x_{2,1}(t,i+1) = x_{1,1}(t,i) + 3x_{1,2}(t,i) + 5u(t,i), \qquad (26)$$
$$y(t,i) = 2x_{1,1}(t,i) + 4x_{1,2}(t,i) + x_{2,1}(t,i) + 6u(t,i).$$

Step 4. The desired realization of (17) has the form:

$$A_{11} = \begin{bmatrix} 0 & 1 \\ 0 & 0 \end{bmatrix}, \quad A_{12} = \begin{bmatrix} 0 \\ 0 \end{bmatrix},$$
$$A_{21} = \begin{bmatrix} 1 & 3 \end{bmatrix}, \quad A_{22} = [0],$$
$$B_1 = \begin{bmatrix} 0 \\ 1 \end{bmatrix}, \quad B_2 = [5], \quad C_1 = \begin{bmatrix} 2 & 4 \end{bmatrix}, \qquad (27)$$
$$C_2 = [1], \quad D = [6]$$

Obtained realization have only nonnegative entries and its of minimal dimension.

4. CONCLUDING REMARKS

A method for computation of a positive minimal realization of a given proper transfer function of all-pole and all-zero continuous-discrete linear systems has been proposed. Sufficient conditions for the existence of a positive and minimal realization of a given proper transfer function have been established. Two procedures for computation of a positive minimal realizations have been proposed. The effectiveness of the procedures have been illustrated by a numerical examples. Extension of those considerations for 2D continuous-discrete linear systems described by second Fornasini-Marchesini model (Sajewski and Kaczorek, 2010) is possible.

An open problem is formulation of the necessary and sufficient conditions for the existence of solution of the positive and minimal realization problem for 2D continuous-discrete linear systems in the general form (Kurek, 1985).

REFERENCES

1. **Antoniou G. E.** (2002), Minimal state space realization for all-pole and all-zero lattice discrete 2D filters, *International Journal of Systems Science*, Vol. 33, No. 10, 799-803.
2. **Benvenuti L., Farina L.** (2004), A tutorial on the positive realization problem, *IEEE Trans. on Autom. Control*, Vol. 49, No. 5, 651-664.
3. **Dymkov M., Gaishun I., Rogers E., Gałkowski K., Owens D. H.** (2004), Control theory for a class of 2D continuous-discrete linear systems, *Int. J. Control* Vol. 77, No. 9, 847-860.
4. **Farina L., Rinaldi S.** (2000), *Positive Linear Systems; Theory and Applications*, J. Wiley, New York.
5. **Kaczorek T.** (1992), *Linear control systems, Vol. 1*, Research Studies Press J. Wiley, New York.
6. **Kaczorek T.** (2002), *Positive 1D and 2D Systems*, Springer-Verlag, London.
7. **Kaczorek T.** (2004), Realization problem for positive discrete-time systems with delay, *System Science*, Vol. 30, No. 4, 117-130.
8. **Kaczorek T.** (2005), Positive minimal realizations for singular discrete-time systems with delays in state and delays in control, *Bull. Pol. Acad. Sci. Tech.*, Vol. 53, No. 3, 293-298.
9. **Kaczorek T.** (2006a), A realization problem for positive continuous-time linear systems with reduced numbers of delay, *Int. J. Appl. Math. Comp. Sci.*, Vol. 16, No. 3, 325-331.
10. **Kaczorek T.** (2006b), Realization problem for positive multivariable discrete-time linear systems with delays in the state vector and inputs, *Int. J. Appl. Math. Comp. Sci.*, Vol. 16, No. 2, 101-106.
11. **Kaczorek T.** (2007), Positive 2D hybrid linear systems, *Bull. Pol. Acad. Sci. Tech.*, Vol. 55, No. 4,351-358.
12. **Kaczorek T.** (2008a), Positive fractional 2D hybrid linear systems, *Bull. Pol. Acad. Tech.*, Vol. 56, No. 3, 273-277.
13. **Kaczorek T.** (2008b), Realization problem for positive 2D hybrid systems, *COMPEL*, Vol. 27, No. 3, 613-623.
14. **Kaczorek T., Busłowicz M.** (2004), Minimal realization problem for positive multivariable linear systems with delay, *Int. J. Appl. Math. Comput. Sci.*, Vol. 14, No. 2, 181-187.
15. **Kaczorek T., Marchenko V., Sajewski Ł.** (2008), Solvability of 2D hybrid linear systems - comparison of the different methods, *Acta Mechanica et Automatica*, Vol. 2, No. 2, 59-66.
16. **Kurek J.** (1985), The general state-space model for a two-dimensional linear digital system, *IEEE Trans. on Austom. Contr.*, AC-30, 600-602.
17. **Roesser R. B.** (1975), A discrete state-space model for linear image processing, *IEEE Trans. on Autom. Contr.*, AC-20, 1-10.
18. **Sajewski Ł.** (2009), Solution of 2D singular hybrid linear systems, *Kybernetes*, Vol. 38, No. 7/8, 2009, 1079-1092.
19. **Sajewski Ł., Kaczorek T.** (2009), Computation of positive realizations of singular SISO hybrid linear systems, *JAMRIS*, Vol. 3, No. 4, 8-14.
20. **Sajewski Ł., Kaczorek T.** (2010), Computation of positive realizations of MIMO hybrid linear systems in the form of second Fornasini-Marchesini model, *Archives of Control Sciences*, Vol. 20, No. 3, 253-271.
21. **Sun-Yuan Kung, Levy B.C., Morf M., Kailath T.** (1977), New Results in 2-D Systems Theory, Part II: 2-D State-Space Models-Realization and the Notions of Controllability, Observability and Minimality, *Proc. of the IEEE*, Vol. 65, No. 6, 945-961.
22. **Varoufakis S. J., Paraskevopoulos P.N., Antoniou G. E.** (1987), On the minimal state-space realizations of all-pole and all-zero 2-D systems, *IEEE Trans. on Circ. and Sys.*, Vol. 34, No. 3, 289-292.

DOUBLY PERIODIC SETS OF THIN BRANCHED INCLUSIONS IN THE ELASTIC MEDIUM: STRESS CONCENTRATION AND EFFECTIVE PROPERTIES

Heorhiy SULYM[*], Iaroslav PASTERNAK[**], Serhiy KUTSYK[**], Wojciech GRODZKI[*]

[*] Bialystok Technical University, Wiejska Str. 45C, 15-351 Bialystok, Poland
[**] Lutsk National Technical University, Lvivska Str. 75, 43018 Lutsk, Ukraine

h.sulym@pb.edu.pl, pasternak@ukrpost.ua, sergosidpr@bigmir.net, wojtekgrr@interia.pl

Abstract: This paper considers the doubly periodic problem of elasticity for anisotropic solids containing regular sets of thin branched inclusions. A coupling principle for continua of different dimension is utilized for modeling of thin inhomogeneities and the boundary element technique is adopted for numerical solution of the problem. The branches of the inclusion can interact both inside the representative volume element and at the interface of neighbor representative elements. A particular example of the elastic medium reinforced by a doubly periodic set of I-beams is considered. Stress intensity and stress concentration inside and outside thin inclusions are determined. The dependence of the effective mechanical properties of the reinforced composite material on the volume fraction of the filament and its rigidity is obtained.

Key words: Anisotropic, Doubly Periodic, Thin Branched Inclusion, Reinforcement, Effective Modulus

1. INTRODUCTION

One of the important tasks of mechanics of inhomogeneous solids, in particular the theory of thin inclusions (Sulym, 2007), is the study of stress concentration at the reinforcements in the concrete and composite materials. The corresponding reinforcements are commonly produced using the standard shapes (a T-beam, an I-beam, a channel, and angle etc.), which have the shape of non-smooth thin branched inclusions. The solution of elasticity problems for solids containing doubly or triply periodic sets of thin inhomogeneities also allows estimating the effective mechanical properties of the corresponding composite materials. Moreover, it is possible to consider both cases of interaction of reinforcements: inside a representative volume element, and on its boundary. The latter allows modeling of novel continuously reinforced composite materials, which strength and rigidity should be very high due to their solidity and the absence of high stress concentration.

The analysis of elastic crooked or cross-like inclusions was mainly performed for the aperiodic problems of elasticity. In particular, the papers (Osiv and Sulym, 2001; 2002) considered the antiplane deformation of solids containing a set of arbitrarily oriented rectilinear joined ribbon-like elastic inclusions. Šackyj and Kundrat (2004) provided the analysis of the out-of-plane deformation of an isotropic medium containing a set of joined rigid line inclusions, in particular, those with the shape of and angle, a T-beam, an I-beam etc. The plane problem of elasticity was considered for an infinite medium containing a cross-like rigid line inclusion (Antipov et al., 1987; Popov, 1993) and a flexible cross-like elastic inclusion (Grigoryan et al., 2002). Pasternak and Sulym (2011) were the fist to propose the general boundary element approach for the solution of plane problems of elasticity for isotropic and anisotropic solids containing systems of joined multi-branched thin elastic inclusions.

The study of doubly periodic sets of thin inhomogeneities was held in Refs. (Kosmodamianskij, 1976; Dolgikh and Fil'shtinskii, 1979; Pasternak, 2012; Pasternak and Sulym 2013). However, to the best of authors' knowledge the doubly periodic problems for thin branched inclusions were not referenced in the scientific literature. Therefore, this paper considers the general approach for studying the doubly periodic problems for anisotropic elastic solids containing thin branched inclusions. This approach is based on the coupling principle for continua of different dimension and the boundary element method.

2. PROBLEM FORMULATION BASED ON THE COUPLING PRINCIPLE

Consider an infinite anisotropic elastic medium containing a doubly periodic set of thin elastic branched inclusions identical to each other, such that translation symmetry conditions are satisfied both for geometrical and physical properties of the solid. For modeling of the corresponding composite material the coupling principle for continua of different dimension (Sulym, 2007) is used. Thus, the inclusion is replaced with the line Γ_C of field discontinuities. One can assume that the line Γ_C coincides with a median line of the thin inhomogeneity. Thus, using this technique the problem is split into two sub-problems: an *external* one, which considers the stress-strain state of a solid and its effective mechanical properties due to a set of discontinuity lines, and an *internal* one, which is focused on the modeling of relations between displacements and tractions at the opposite sides of the thin inhomogeneity, and thus, at the opposite faces of the discontinuity line Γ_C.

According to Pasternak (2012), the external problem is reduced to the following system of dual integral equations:

$$\frac{1}{2}\Sigma\mathbf{u}^0(\mathbf{y}) = \text{RPV}\int_{\Gamma_0^+}\mathbf{U}^{\text{dp}}(\mathbf{x},\mathbf{y})\Sigma\mathbf{t}^0(\mathbf{x})d\Gamma(\mathbf{x})$$

$$- \text{CPV}\int_{\Gamma_0^+}\mathbf{T}^{\text{dp}}(\mathbf{x},\mathbf{y})\Delta\mathbf{u}^0(\mathbf{x})d\Gamma(\mathbf{x})+\mathbf{I}^\infty(\mathbf{y}),$$

$$\frac{1}{2}\Delta\mathbf{t}^0(\mathbf{y}) = n_j^+(\mathbf{y})\left[\text{CPV}\int_{\Gamma_0^+}\mathbf{D}_j^{\text{dp}}(\mathbf{x},\mathbf{y})\Sigma\mathbf{t}^0(\mathbf{x})d\Gamma(\mathbf{x})\right.$$

$$\left.-\text{HPV}\int_{\Gamma_0^+}\mathbf{S}_j^{\text{dp}}(\mathbf{x},\mathbf{y})\Delta\mathbf{u}^0(\mathbf{x})d\Gamma(\mathbf{x})+\Xi_j^\infty\right],$$

$$(1)$$

where $\mathbf{u}^0$ and $\mathbf{t}^0$ are displacement and traction vectors at the base contour $\Gamma_0\,\square\,\Gamma_C$ in the selected representative volume element; $\Delta(\square)=(\square)^+-(\square)^-$, $\Sigma(\square)=(\square)^++(\square)^-$; signs "+" and "−" denote variables concerned with faces Γ_C^+ and Γ_C^- of the mathematical cut Γ_C; symbols RPV stands for the Riemann Principal Value, CPV for the Cauchy Principal Value and HPV for the Hadamard Principal Value (finite part) of an integral. The functions $\mathbf{I}^\infty(\mathbf{y})$ and $\Xi_j^\infty(\mathbf{y})$ define the external load set by the components $\langle\sigma_{ij}\rangle$ of the average stress tensor and are given by special integral identities (Pasternak, 2012). Closed-form expressions for the kernels $\mathbf{K}^{\text{dp}}=\left[\mathbf{U}^{\text{dp}},\mathbf{T}^{\text{dp}},\mathbf{D}_j^{\text{dp}},\mathbf{S}_j^{\text{dp}}\right]$ are given in Ref. (Pasternak, 2012). These kernels are functions of coordinates of collocation point $\mathbf{y}$ and integration point $\mathbf{x}$, and also depend on the vectors $\boldsymbol{\omega}^{(1)}$ and $\boldsymbol{\omega}^{(2)}$ of the fundamental periods, which form the lattice (Fig. 1).
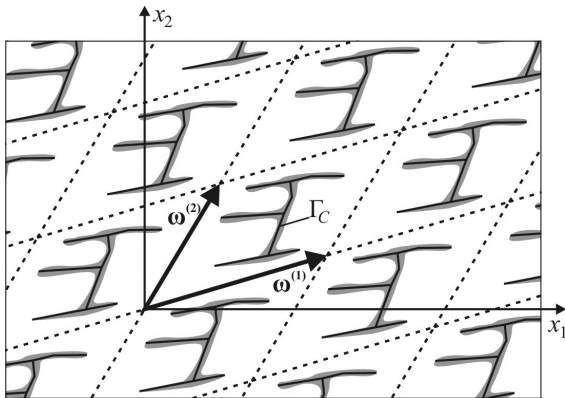

Fig. 1. The sketch of the problem

Pasternak and Sulym (2011), Pasternak (2011) provide the closed-form relations for the mathematical models of thin non-branched elastic and piezoelectric, isotropic and anisotropic inclusions, which can be generally presented with the following functional dependences:

$$\Sigma\mathbf{u}(\mathbf{y})=\mathbf{F}^u\left(\mathbf{y},\Sigma\mathbf{t},\Delta\mathbf{u},\mathbf{P}^0,\mathbf{P}^1,M^0,M^1\right)$$

$$\Delta\mathbf{t}(\mathbf{y})=\mathbf{F}^t\left(\mathbf{y},\Sigma\mathbf{t},\Delta\mathbf{u},\mathbf{P}^0,\mathbf{P}^1,M^0,M^1\right)$$

$$(2)$$

Here $\mathbf{P}^0$, M^0, $\mathbf{P}^1$ and M^1 are the resultant force and moment applied at the left and right ends of a thin inclusion, respectively. The inclusion model given by Eq. (2) is used as a basic one for description of the edges of the branched inhomogeneities.

According to Pasternak and Sulym (2011), to study a thin branched inclusion the latter is described by the undirected graph $G(V)$, which edges $E_{ji}=E_{ij}=(v_i,v_j)$, $v_i,v_j\in V$ correspond to the non-branched links of the inclusion. It is assumed that the graph $G(V)$ contains no loops ($E_{ii}=(v_i,v_i)\in 0$) and no iso-

lated vertices. Nevertheless, the absence of loops does not mean that one cannot model the stress state of solids with closed thin inclusions. The later can be described with a closed graph, which contain at least two vertices. Those vertices, which join two or more edges, are further called nodes, and the other are called the free ends of a branched inclusion. Each of the edges E_{ij} can be modeled using various variants of the generalized inclusion model given by Eq. (2).

While studying the doubly periodic problems one should consider two possible cases of interaction of the edges of the branched inclusion: 1) inside the representative volume element, and 2) between the inhomogeneities at the interface of two neighbor representative elements.

To study the first case one can directly use the algorithm developed by Pasternak and Sulym (2011). In particular, if a thin branched inclusion consists of n edges joined with $m\leq n$ nodes and the contact between inclusion's edges is perfect, then at the each of m nodes the following balance equations should be satisfied:

$$\sum_{k=1}^q\mathbf{P}^k=\mathbf{0}\,,\quad\sum_{k=1}^q M^k=0\,,\qquad(3)$$

where q is a number of edges of the inclusion, which are joined by the node; $\mathbf{P}^k$ and M^k are the force and the moment applied at the end of the k-th edge included by the vertex. Besides, the continuity conditions for displacements at the node can be satisfied by equating the average values of displacements $\mathbf{u}=\frac{1}{2}\sum\mathbf{u}$ and rotation angles ω of the edges united by the node:

$$\mathbf{u}^1=\mathbf{u}^2=...=\mathbf{u}^q\,,\quad\omega^1=\omega^2=...=\omega^q\,.\qquad(4)$$

The rotation angles (the slope) of the inclusion's lines can be determined, for example, using the Euler–Bernoulli beam equation.

Equations (1), (2) together with relations (3), (4), which produce $3q$ additional equations for determination of $3q$ unknown components of contact force ; $\mathbf{P}^k$ vectors and moments M^k at the nodes of the branched inclusion, can be used for studying doubly periodic problems for inhomogeneous solids, which representative volume elements contain internal thin inclusions.
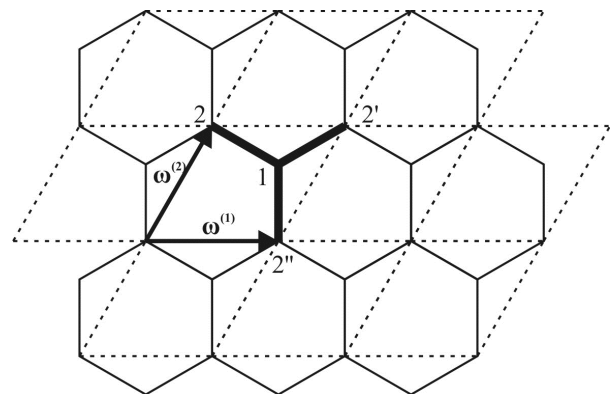

Fig. 2. Doubly periodic set of the thin inclusions joined the interface of neighbor representative volume elements

As for the case of thin branched inclusions, which are joined at the interface of neighbor representative volume elements, the displacement continuity conditions (4) are more complicated.

For example, consider honeycomb with hexagonal cells filled with honey (Fig. 2). The walls of the cells can be considered as thin inclusions and the honey represents the elastic medium. The geometry of this doubly periodic problem thus can be set by means of three rectilinear branches of inclusion of the length a each, which repeats with the fundamental periods $\boldsymbol{\omega}^{(1)} = \left[\sqrt{3a}, 0\right]^{\mathrm{T}}$, $\boldsymbol{\omega}^{(1)} = \frac{1}{2}\left[\sqrt{3a}, 3a\right]^{\mathrm{T}}$.

For the internal node 1 inside the representative volume element (Fig. 2) relations (3), (4) can be used without any cautions. As for the node 2 formed by the ends 2–2'–2" of the edges of the thin inclusion, the balance equations (3) for forces and moments are also satisfied. However, due to the quasi-periodicity of the displacements, the displacement continuity conditions for the joints at the interface of the neighbor representative elements should account for the cyclic constants. In particular, for the set of inclusions depicted in Fig. 2 the displacement continuity conditions write as:

$$\mathbf{u}^{2'} = \mathbf{u}^2 + \delta\mathbf{u}^{(1)} , \ \mathbf{u}^{2'} = \mathbf{u}^{2"} + \delta\mathbf{u}^{(2)}$$
$$\omega^2 = \omega^{2'}, \ \omega^2 = \omega^{2"} \tag{5}$$

Here $\delta\mathbf{u}^{(1)}$ and $\delta\mathbf{u}^{(2)}$ are the cyclic constants of the displacement vector along the corresponding fundamental periods. In case of a perfect contact between inclusions and the medium these constants can be determined through the external problem. According to Pasternak (2012), they are defined with the following integral identities:

$$\delta\mathbf{u}^{(k)} = \sum_j \frac{\partial}{\partial x_j} \mathbf{I}^{\infty}(\mathbf{x}) \omega_{x_j}^{(k)} + \delta\hat{\mathbf{u}}^{(k)},$$
$$\delta\hat{\mathbf{u}}^{(1)} = 0, \tag{6}$$
$$\delta\hat{\mathbf{u}}^{(2)} = \int_{\Gamma_0^+} \left[\mathbf{U}^*(\mathbf{x})\Sigma\mathbf{t}^0(\mathbf{x}) - \mathbf{T}^*(\mathbf{x})\Delta\mathbf{u}^0(\mathbf{x})\right] d\Gamma(\mathbf{x}).$$

The kernels $\mathbf{U}^*(\mathbf{x})$ and $\mathbf{T}^*(\mathbf{x})$ are regular.

The obtained system of the boundary integral equations (1)–(6) is suitable for the solution by the modified boundary element method (BEM) of Pasternak (2011). Besides, obtained equations allow determination of the effective mechanical properties of composite materials with the regular structure based on the BEM using the approach of Pasternak (2012).

The BEM numerical implementation should account for the stress square root singularity at the free ends of a thin inclusion. This singularity can be accounted for by utilizing special shape functions (Pasternak, 2011) for modeling of displacement and stress discontinuities at the ends of the discontinuity line Γ_C, which replaces the inhomogeneity. Moreover, according to Pasternak (2011), the strength of the fields' singularity at tips of a thin inhomogeneity is described by generalized stress intensity factors (SIF), which are determined through the discontinuity functions in the local rectangular coordinate system with the origin at the tip of an inhomogeneity by the following formulae:

$$\mathbf{k}^{(1)} = \lim_{s\to 0}\sqrt{\frac{\pi}{8s}}\mathbf{L}\cdot\Delta\mathbf{u}(s), \ \ \mathbf{k}^{(2)} = -\lim_{s\to 0}\sqrt{\frac{\pi s}{2}}\mathbf{S}^{\mathrm{T}}\cdot\Sigma\mathbf{t}(s), \tag{7}$$

where: $\mathbf{k}^{(i)} = [K_{2i}, \ K_{1i}]^T$, $\Delta\mathbf{u} = [\Delta u_1, \ \Delta u_2]^T$, $\sum\mathbf{t} = [\sum t_1, \ \sum t_2]^T$, K_{ij} the generalized SIF. For a crack $K_{11} = K_I$, $K_{21} = K_{II}$, $K_{12} = K_{22} = 0$, where K_I, K_{II}, are classical SIF of the cracks theory; $\mathbf{L}$ and $\mathbf{S}$ are real Barnett–Lothe tensors

(Ting, 1996), which depend only on the material properties of the medium in the local coordinate system.

The displacement vector and the stress function in the local coordinate system $Ox_1'x_2'$ with the origin O at the inclusion tip and Ox_1' axis directed along a median line are related to the generalized SIF by the following asymptotic formulae (Pasternak, 2011)

$$\mathbf{u} = \sqrt{\frac{2}{\pi}}\,\mathrm{Im}\left\{\mathbf{A}\left\langle\sqrt{Z_*}\right\rangle\left(\sqrt{-1}\mathbf{B}^{-1}\mathbf{k}^{(1)} - 2\mathbf{A}^{\mathrm{T}}\left(\mathbf{S}^{\mathrm{T}}\right)^{-1}\mathbf{k}^{(2)}\right)\right\},$$
$$\boldsymbol{\varphi} = \sqrt{\frac{2}{\pi}}\,\mathrm{Im}\left\{\mathbf{B}\left\langle\sqrt{Z_*}\right\rangle\left(\sqrt{-1}\mathbf{B}^{-1}\mathbf{k}^{(1)} - 2\mathbf{A}^{\mathrm{T}}\left(\mathbf{S}^{\mathrm{T}}\right)^{-1}\mathbf{k}^{(2)}\right)\right\}. \tag{8}$$

Here $\mathbf{A}$ and $\mathbf{B}$ are the Stroh matrices (Ting, 1996); $\left\langle\sqrt{Z_*}\right\rangle = \mathrm{diag}\left[\sqrt{x_1' + p_1 x_2'}; \ \sqrt{x_1' + p_2 x_2'}\right]$; p_1 and p_2 are the eigenvalues of the Stroh eigenvalue problem (Ting, 1996); $\boldsymbol{\varphi}$ is the stress function vector, which defines the components of the stress tensor at the arbitrary point by the following relations:

$$\boldsymbol{\sigma}_1 = \left[\sigma_{i1}\right] = -\boldsymbol{\varphi}_{,2}$$
$$= \frac{-1}{\sqrt{2\pi}}\,\mathrm{Im}\left\{\mathbf{B}\left\langle p_*\sqrt{Z_*}\right\rangle\left(\sqrt{-1}\mathbf{B}^{-1}\mathbf{k}^{(1)} - 2\mathbf{A}^{\mathrm{T}}\left(\mathbf{S}^{\mathrm{T}}\right)^{-1}\mathbf{k}^{(2)}\right)\right\},$$
$$\boldsymbol{\sigma}_2 = \left[\sigma_{i2}\right] = \boldsymbol{\varphi}_{,1}$$
$$= \frac{1}{\sqrt{2\pi}}\,\mathrm{Im}\left\{\mathbf{B}\left\langle\sqrt{Z_*}\right\rangle\left(\sqrt{-1}\mathbf{B}^{-1}\mathbf{k}^{(1)} - 2\mathbf{A}^{\mathrm{T}}\left(\mathbf{S}^{\mathrm{T}}\right)^{-1}\mathbf{k}^{(2)}\right)\right\}. \tag{9}$$

According to Sulym (2007), the order of stress singularity at the nodes of the branched inclusion is assumed to be weaker than a square root one (the same as and in the theory of branched cracks). Therefore, to model the ends of the edges joined in the node one can use quadratic discontinuous boundary elements. The same concerns nodes at the interface of the neighbor representative volume elements.

3. NUMERICAL ANALYSIS OF REGULAR SETS OF THIN BRANCHED INCLUSIONS

Consider plane strain of the isotropic elastic medium (the Poisson ratio equals 0.3) containing a doubly periodic set of thin branched inclusions. The inhomogeneities form the rectangular lattice with the fundamental periods $\boldsymbol{\omega}^{(1)} = [d, 0]^{\mathrm{T}}$ and $\boldsymbol{\omega}^{(2)} = [0, 2d]^{\mathrm{T}}$. Inclusions have the shape of the I-beam cross-section with the width of $2a$ and the height of $4a$ (Fig. 3). The thickness of inclusions' edges equals $2h$ ($h = 0.01a$). The medium is loaded at the infinity with the uniform bi-axial stress p.

Fig. 4 depicts the plots of the normalized generalized SIF $K_{ij}^* = \frac{K_{ij}}{p\sqrt{\pi a}}$ at the tips of the branched I-beam inclusion and the components $P_i^* = \frac{P_i}{pa}$ of the force vector, and the bending moment $M^* = \frac{M}{(pa)^2}$ at the point E of the edge AE of the inclusion depending on the relative rigidity $K = \frac{G^i}{G}$ of the latter (G is the shear modulus). The density of the filament of the medium is defined by the parameter $\lambda = \frac{2a}{d}$. Continuous curves corre-

spond to the density of $\lambda = 0.1$, dashed ones $-\lambda = 0.5$, and dash-dot $-\lambda = 0.8$. For $\lambda = 0.1$ the difference between the values of SIF from those obtained for the aperiodic problem for a single I-beam inclusion (Pasternak and Sulym, 2011) does not exceed 0.5 % that justifies the reliability of the developed algorithm and verifies the obtained results.

One can see in Fig. 4 that for soft ($k < 1$) inclusions their approaching essentially increases mode I SIF K_{11} (the normal opening mode). Instead of that, mode II SIF K_{21} does not show such obvious dependence: with the increase in the parameter λ SIF K_{21} first decreases, and then starts to increase.

For rigid ($k > 1$) elastic inclusions the generalized mode I SIF K_{12} increases with the growth of λ. Approaching of the inclusions also causes the growth of the longitudinal force P_1 in the flanges of the I-beam. Instead of that, limiting values of the mode II generalized SIF K_{22} decrease. Besides, at approaching of the inclusions the bending moment M and the shear force P_2 at the node E of the flange AE also decrease. These values are determinative for the assessment of the strength of the thin inhomogeneity. Thus, approaching of inclusions allows to reduce stresses both outside and inside the inclusion.
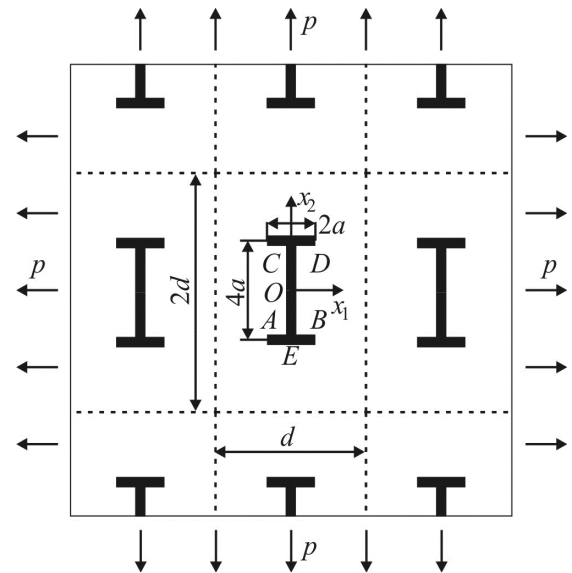

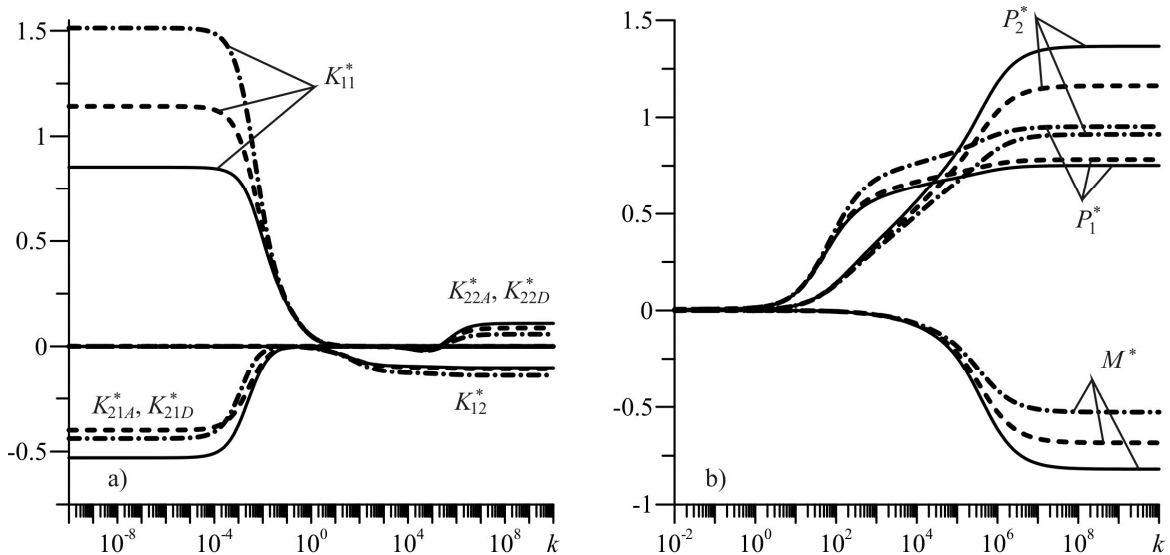**Fig. 3.** The elastic medium reinforced with a doubly periodic set of I-beams

Fig. 4. Stress intensity at the tips of inclusion and the force and bending moment inside it
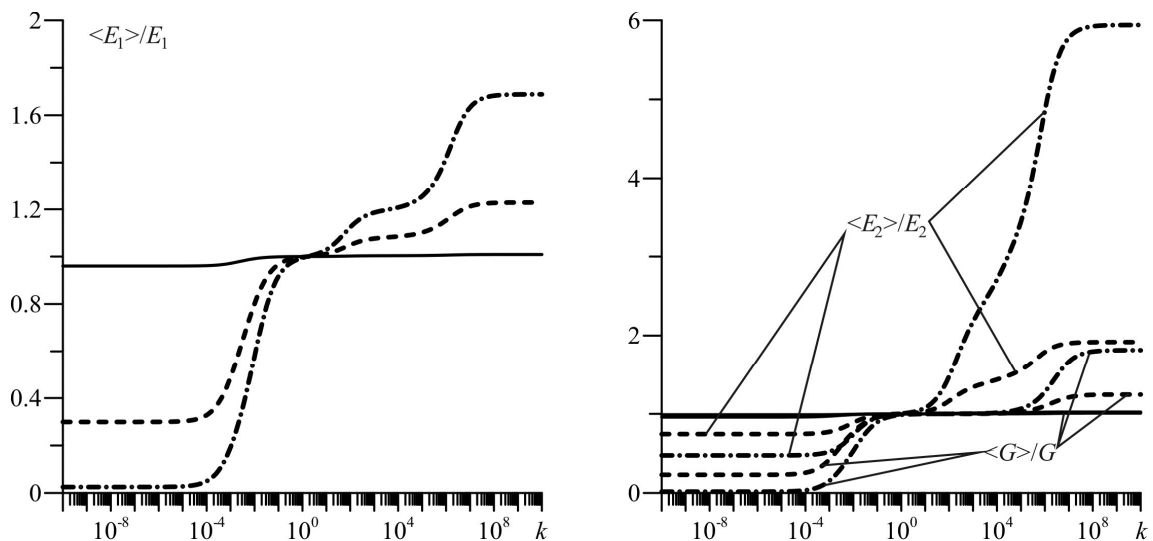

Fig. 5. Effective moduli of the medium reinforced with the I-beams

Besides stress intensity, developed numeric-analytic approach allows determining of the effective mechanical properties of the medium reinforced by the doubly periodic set of I-beams. For example, Fig. 5 depicts the effective moduli $\langle E_1 \rangle$ and $\langle E_2 \rangle$, and the effective shear modulus $\langle G \rangle$ for three selected values of the filament density λ depending on the relative rigidity k of inclusions.

One can see in Fig. 5 that the reinforced medium is essentially anisotropic. To increase the effective moduli one should reinforce the medium with essentially rigid fibers. It should be noted that the effective moduli $\langle E_1 \rangle$ and $\langle G \rangle$ increase with the growth of k in two stages, which is well observed in Fig. 5. Such step-like character of the plot can be related with the influence of bending of the flanges of I-beam. Comparing Fig. 4 and Fig. 5 one can see that the second stage of growth of elastic moduli is related with the increase in the bending moment at the flange.

The most essential increase in the effective modulus is observed for a composite along the vertical axis of the rigid reinforcement I-beam. Moreover, for $\lambda = 0.8$ it is possible to increase this modulus up to six times comparing to the unreinforced medium. Taking into account that according to Fig. 4 the generalized SIF K_{22}, shearing force and the bending moment at the flange decrease, such reinforcing can be considered as a favorable one.

4. CONCLUSIONS

The proposed approach for studying of doubly periodic sets of thin branched inclusions allows not only to determine stress concentration and intensity in composites with regular reinforcement, but also to assess the effective mechanical properties of such materials. Thus, the developed technique can be used as a tool for designing and optimization of the composite materials reinforced with thin filament, in particular, with a standard shapes. The considered example for a medium reinforced with the I-beams justified the efficiency of the proposed approach and allowed determining effective moduli of such composite. In particular, it is observed that approaching of such thin rigid reinforcements allows both to increase effective moduli and to decrease internal stress concentration and intensity.

REFERENCES

1. **Antipov Yu.A., Popov G.Ya., Yatsko S.I.** (1987), Solution of the problem of stress concentration around intersecting defects by using the riemann problem with an infinite index, *Journal of Applied Mathematics and Mechanics*, 51(3), 357–365.
2. **Dolgikh V.N., Fil'shtinskii L.A.** (1979), Model of an anisotropic medium reinforced by thin tapes, *Soviet Applied Mechanics*, 15(4) 292–296.
3. **Grigoryan E.H., Torosyan D.R., Shaghinyan S.S.** (2002), A problem for an elastic plane containing a cross-like inclusion, *Mechanics. Proceedings of National Academy of Sciences of Armenia*, 55 (1), 6–16.
4. **Kosmodamianskij A.S.** (1976), *Naprâžennoe sostoânie anizotropnyh sred s otverstiâmi ili polostâmi*, Vyšča škola, Kyiv.
5. **Osiv O.P, Sulym H.T.** (2002), Antyploska deformaciâ seredovyšča zi zlučenymy pružnymy vklûčennâmy, *Mehanika i fizyka rujnuvannâ budivelnuh materialiv i konstrukcij*, 5, 154–164.
6. **Osiv O., Sulym G.** (2001), Antiplane deformation of isotropic medium with connected elastic ribbon-like inclusions, *Abstracts of the Fourth Polish-Ukrainian Conference "Current Problems in Mechanics of Nonhomogeous Media" (Łódż, 4–8 Sept., 2001)*, Technol. Univ. of Łódż, Łódż.
7. **Pasternak Ia.** (2011), Coupled 2D electric and mechanical fields in piezoelectric solids containing cracks and thin inhomogeneities, *Engineering Analysis with Boundary Elements*, 35(4), 678–690.
8. **Pasternak Ia.** (2012), Doubly periodic arrays of cracks and thin inhomogeneities in an infinite magnetoelectroelastic medium, *Engineering Analysis with Boundary Elements*, 36(5), 799–811.
9. **Pasternak Ia., Sulym H.** (2011), Ploska zadača teorij pružnosti anizotropnogo tila z tonkymy gillâstymy pružnymy vklûčennâmy, *Visnyk Ternopilskogo NTU*, 16(4) 23–31.
10. **Pasternak Ia., Sulym H.** (2013), Stroh formalism based boundary integral equations for 2D magnetoelectroelasticity, *Engineering Analysis with Boundary Elements*, 37(1), 167–175.
11. **Popov V.G.** (1993), Dynamic problem of the theory of elasticity for a plane containing a rigid cruciform inclusion, *Journal of Applied Mathematics and Mechanics*, 57(1), 125–131.
12. **Šackyj I.P, Kundrat A.M.** (2004), Antyploska deformaciâ pružnogo prostoru zi zvâzanymy žorstkymy stričkovymy vklûčennâmy, *Dopovivdi NAN Ukrajiny*, 11, 55–60.
13. **Sulym H.T.** (2007), *Osnovy matematyčnoj teorij termopružnoj rivnovagy deformivnyh til z tonkymy vklûčennâmy*, Dosl.-vydav. centr NTŠ, L'viv.
14. **Ting T.C.T.** (1996), *Anisotropic elasticity: theory and applications*, Oxford University Press, New York.

THE DYNAMIC PERFORMANCE ANALYSIS OF THE FOIL BEARING STRUCTURE

Grzegorz ŻYWICA[*]

[*]Institute of Fluid-Flow Machinery, Polish Academy of Sciences, ul. Fiszera 14, 80-231 Gdańsk, Poland

gzywica@imp.gda.pl

Abstract: Foil bearings are a variety of slide bearings in which an additional set of foils is applied between journal and bush, in order to improve the selected static and dynamic properties. Engineers and researchers from all over the world investigate bearings of this type since many years – both from numerical as well as experimental point of view. Due to the complexity of construction, the reliable simulation models are all the time being searched for. This paper discusses the important stages of elaboration of the structural supporting layer numerical model of the foil bearing as well as results of verification tests. The main goal of the conducted study was assessment of reliability of the elaborated numerical model, in scope of dynamic properties. In the near future it will be used for elaboration of the numerical model of the entire foil bearing, which will take into account also phenomena in fluid-film layer. Those models will be used together to describe bearing system in operation.

**Key words:** Foil Bearings, Bearing Systems, Micro-Turbines, High-Speed Rotors

1. INTRODUCTION

Bearing systems based on foil bearings are the most used in lightly loaded, high-speed rotating systems. With the use of such bearings a number of benefits is associated with the operation of the machine. Comparing to conventional aerostatic bearings, foil bearings do not require a stream of compressed air supply, which is advantageous due to the energy balance of the machine. Another advantage is the large dynamic stability of rotors supported on foil bearings, which is achieved mainly thanks to the very good damping properties of the set of foils (bump foil and top foil). Increased stability of the rotor also allows the machine to operate at higher speed. In addition, bearings of this type can operate at very high temperatures reaching several hundred degrees Celsius. The advantages of foil bearings are that they are increasingly being used in machines such as: micro-turbines, turbochargers or expanders (Agrawal, 1997; Lee et al., 2012).

The main difference in the construction of conventional slide bearings and foil bearings concerns additional element of thin, contoured foils' set of high compliance (Fig. 1). This assembly is placed between the mating surfaces of the journal and bush. This allows improving the stiffness-damping properties of the support system, which has a beneficial effect on the dynamic properties of the rotor-bearing system. The use of this approach allows stable operation of the system even at very high speed, not accessible to other slide bearings. Unstable operation of a machine at high speed is often caused by the limited possibility of damping in the bearings (especially in gas bearings). In the foil bearings this issue is limited.

Discussing foil bearings we should also pay attention to their basic disadvantages that are not found in any other bearing systems. Foil bearings should be uniquely designed for each specific machine. Depending on the load, speed, lubricant, and temperature it is necessary to use a suitable materials and geometry of the compliant elements. For technological reasons, it is difficult to produce repeatable series of bearings. Bearings of this kind are installed with a small interference, well adapted for proper operation at higher speed. This results in two consecutive issues: the starting and stopping of the machine causes direct contact between the top foil and the journal, which leads to rapid wearing away the elements. The second problem is the relatively high starting torque, required to run the machine. Despite these disadvantages, in some of the aforementioned machines, foil bearings are the most suitable ones.
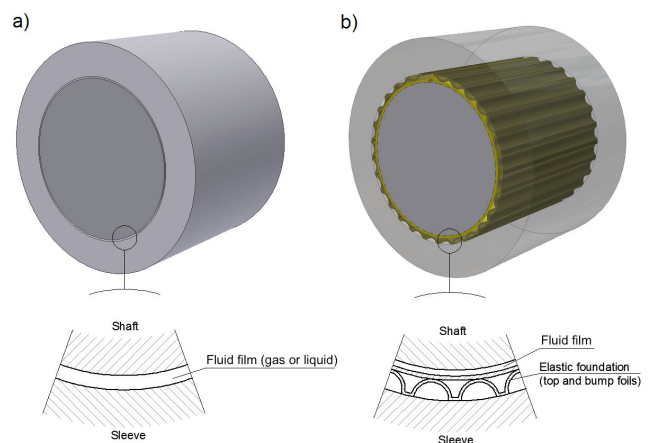
Fig. 1. The difference between a classical slide bearing (hydrodynamic or aerodynamic) (a) and a foil bearing (b).

In the world literature, in the recent years, more and more space is devoted to the research and modeling of foil bearings (DellaCorte, 1997; Lee et al., 2004; Rubio and San Andres, 2006; Kim and Park, 2009). A couple of research and industry centres have been involved in examining the subject, mainly in the United States of America. The theoretical description of the operation of foil bearings must take into consideration the many physical

phenomena occurring in parallel and requires the search for new, reliable models. Simple analytical models fail in this case, and it is necessary to use the latest software that supports engineering calculations and advanced computer techniques. The main problem relates to an adequate description of the phenomena occurring in the geometrically complex, flexible set of foils, as well as the integration of structural analysis with the flow analysis (description of the phenomena occurring in the lubricant wedge). The appropriate description of the processes occurring in these bearing nodes should take into account: the phenomena of contact, deformations of geometrically complex set of foils, thermal phenomena, the flow of a lubricant in deformed bearing interspace and fluid-structure interactions (Selehi and Heshmat, 2000; San Andres and Kim, 2009). This brings about a difficulties often associated with the limited applications and the need to carry out calculations in parallel with several applications.

The group of scientists at the Institute of Fluid-Flow Machinery Polish Academy of Sciences have been dealing with the problematics of application and analysis of foil bearings. The results of previous studies have been included in several earlier publications (Kicinski et al., 2008; Kozanecki et al., 2009; Kicinski and Zywica, 2010; Zywica, 2011). The ongoing work is aimed at creating a complete model of the foil bearing, taking into account both structural (without geometric simplification) and flow supporting layer. This article discusses the next phase of work on the foil bearing numerical model, which aims to study the properties of dynamically loaded bearing structural layers. This is a continuation of the work described in an earlier article (Zywica, 2011), which dealt with the analysis of the same system statically loaded. Since foil bearing elements during operation are imposed by variable dynamic forces, it should be included in a bearing model. In addition to the discussion of the numerical model and simulation studies, the article also presents the results of experimental verification of the model.

2. COMPUTATIONAL ANALYSIS

2.1. Numerical model of a foil bearing structure

The complex geometry of the foils and of the bearing was prepared in a parametric program suitable for creating complex geometry - Autodesk Inventor. The parameterization of the model allowed any change in the geometry and quick adaptation of dimensions to current needs. Due to the two-dimensional nature of structural deformation of the foil bearing support layer and low computing performance of 3D models it was decided to use a two-dimensional model. This model allows a very precise analysis of the phenomena occurring in the foil bearings (first and second generation), in which there is no variation of the bump foil geometry in the axial direction. The two-dimensional model is able to reproduce the full geometry of the test bearing in a plane perpendicular to the axis of rotation and the width of the bearing is taken into account by an additional parameter. The primary dimensions and parameters of the test bearing are given on Tab. 1. They were determined on the basis of (Rubio and San Andres, 2006; Kim et al., 2009), which allowed the comparison of results. Due to the need to preserve the uniqueness of the geometry description, not so much relevant differences occurred only in the case of the output, such as the bump pitch and bump length.

The bump foil of the tested bearing composed of five identical sectors, equally spaced around the circumference of a bush.

The total number of bumps was set to 25. The nominal clearance in the actual bearings is only approximate and, in practice, due to the pre-clamp of the bearing, it is usually determined experimentally on a special test rig (Howard and San Andres, 2010). However, it is given in the case of such bearing models, since it is necessary to draw an unambiguous geometry.

Tab. 1. Nominal dimensions, parameters and material specification of the foil bearing.

No	Dimension/Parameter	Value
1	Inner diameter	38,17 mm
2	Bearing length	38,10 mm
3	Nominal journal diameter	38,10 mm
4	Nominal radial clearance	0,035 mm
5	Number of bumps	25
6	Bump pitch	4,57 mm
7	Bump length	4,06 mm
8	Bump height	0,38 mm
9	Foil thickness (top and top foil)	0,1 mm
10	Young's modulus	$2,1 \cdot 10^{11}$ Pa
11	Poisson's ratio	0,29
12	Density of material	7860 kg/m³

FEA model of analyzed foil bearing was developed by ABAQUS software. Due to the relatively high compliance of the foils set consisting of thin steel plates, bush and journal were treated as rigid bodies in the analysis. Therefore, these elements were simplified and replaced by the rings of a thickness that allows to apply a regular mesh. Developed FEM model is shown in Fig. 2.
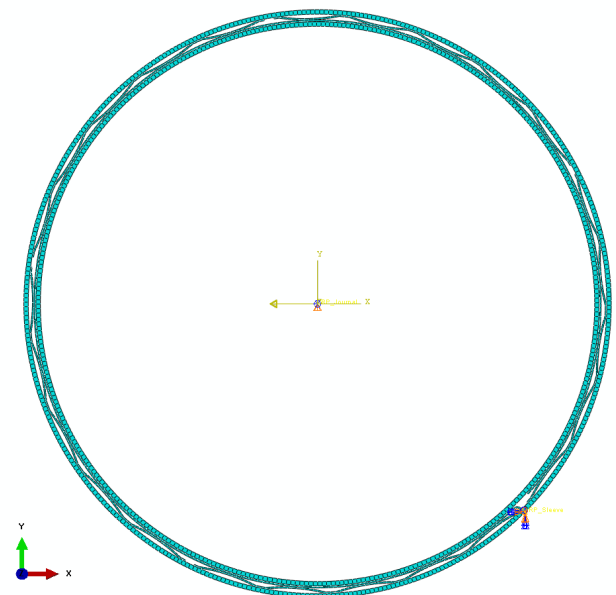
Fig. 2. FEM model of the foil bearing structure

The numerical model of the foil bearing structure presented above was composed of a total of 9778 degrees of freedom. The size and type of finite elements, FEM seeding of individual pieces of geometry, was selected by the numerical model optimization. Finally, for discretization CPE4RH type elements were

chosen which have four nodes and first order shape functions. These elements allowed to obtain the most reliable results. The top foil and each of the five sectors of the bump foil were one-sidedly restrained. The displacements of the rest of the foil were limited by journal and bushing surfaces and interactions. Between these elements contact was modelled where friction coefficient was set to 0.1.

2.2. FEM calculations

In order to determine the dynamic characteristics, based on the discussed numerical model, simulation calculations had been planned to be adapted for experimental tests conducted by Kim et al. (2009). These tests consisted of forcing vibrations of structural part of the foil bearing using electromagnetic exciter. During the experiment, the rotor was not rotating, and its function was done by the shaft rigidly mounted in the spindle lathe.The bearing sleeve was connected only with the tension member, through which harmonic excitation was transmitted from the exciter. The current value of the exciting force was measured using a force sensor that had been mounted between the tension member and the bearing sleeve. For displacement measurement the eddy current sensor was used. Schematic view of the test rig is shown in Fig. 3.
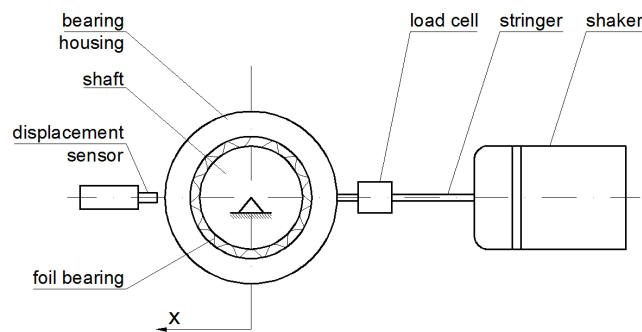

Fig. 3. Schematic view of test stand for dynamic excitation of the foil bearing
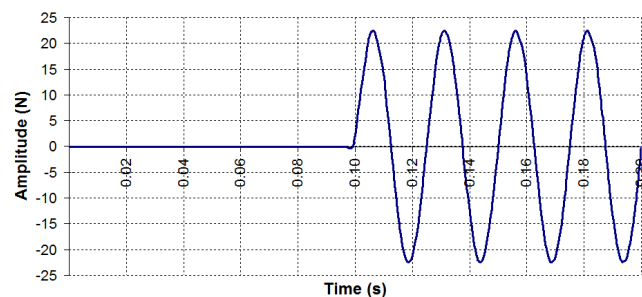

Fig. 4. The time course of the excitation force

The conditions of the experiment were reproduced during the simulations by appropriately set of boundary conditions and load. The essence of these researches relied on the determination of the relative displacements of journal and bush caused by the external load, which had been limited by the presence of foils' set and the inertia of bearing components. Therefore, in order to simplify the numerical model, external load during the analysis

was applied to the journal (as in real bearing) and not to the bearing bush. The bush was fixed and unable to move in any direction. Regarding the weight of bearing components, this approach allows to obtain results that can be compared to the results of the mentioned work (Kim et al., 2009).

ABAQUS calculations focused on the dynamic response of the system in the horizontal direction (in the direction of the excitation force). The procedure 'Dynamic, Implicit' was used along with active option 'Nonlinear geometry'. Excitation frequency was 40 Hz, and the amplitude of the exciting force 22.5 N (according to the experiment). The force was changing by the sine function. The total time of the dynamic analysis was 0.2 s, while the harmonic force was active only for 0.1 s (from 0.1 s to 0.2 s). Initial analysis time of 0-0.1 s was necessary to determine the contact conditions. The time course of force acting on the bearing is shown in Fig. 4.

The model of foil bearing structure with acting dynamic force was based on previously developed and successfully validated model presented in the previous article (Zywica, 2011). As preliminary calculations had shown, some of the parameters of the model required modifications and refinement. It was also necessary to insert additional parameters in the model, that in previous, static analysis were neglectable. The key parameter was the mass of the loaded and moving bearing component. Also important was the weight of additional components, such as the load cell, stringer, even thermocouples with cables (that were used to measure temperature). It was also found that the relatively stiff cables that were used to connect thermocouples and load cell also affected stiffness-damping properties of the system and it had to be taken into account in the model. The values of these additional parameters, which were not initially known, were chosen in the process of verification and model tuning.

3. COMPARISON OF PREDICTED AND EXPERIMENTAL RESPONSE

The basic criterion for assessing the usefulness of numerical models should be its reliability, which is easily determined by comparison with the real system. In the case of this model of foil bearing verification was carried out in two stages. The first stage of the verification concerned the characteristics of structural part of the bearing under static load (Zywica, 2011). In the research study (presented in this article) statically proven model was verified under a dynamic load operation.

The characteristics obtained initially in the form of displacements of the journal in the course of time and displacement versus the value of the load are shown in Fig. 5 and 6. From the characteristics shown in Fig. 5 we can observe that the journal after applying the force was bounced off the foils, and then, under the influence of the increasing force, was again pressed into foil set. To compare the characteristics obtained with the results of the experiment described in the article (Kim et al., 2009), it was necessary to draw the graph in the configuration: the dynamic load - displacement, which is shown in Figure 6. Results determined by simulation differed significantly from the experimental curves. At higher load (above 10 N) journal displacement depended only on the value of the load, regardless of whether the system was loading or unloading. In the real bearing a marked difference in displacement was observed depending on the load phase, which meant the capacity of the bearing structure to dissipate the

energy. This indicated the need to refine the numerical model so that its characteristics were similar to the real system.

Modification of pre-tested model was started from the identification of the most relevant differences between the model and the test rig. The first potential cause could be neglecting of weight of bearing's elements, what for the static analyses conducted earlier did not matter. Additional concentrated mass was added in the journal model to its centre of gravity, but according to the experiment it reflected on the weight of bush, sensors, stringer and thermocouples with the wires. Using the description of the test rig and a series of tests the value of the additional weight was set at 0.5 kg.
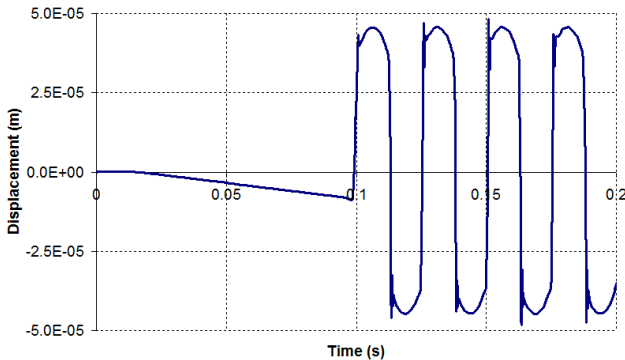

Fig. 5. Displacement of the shaft in the foil bearing at dynamic load (numerical model before validation)
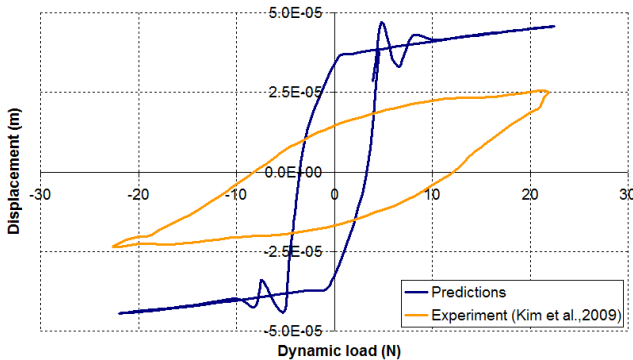

Fig. 6. Comparison of predicted and experimental displacement versus dynamic load for the foil bearing structure (predictions based on the numerical model before validation)

The described modified system still did not allow to obtain the similar characteristics to the experimental results. It was necessary to introduce the following modifications to the model involving the use of additional stiffness-damping elements that were connected to the center of journal. After many attempts optimal value of damping and stiffness was set at D = 1000 N·s/m and K = 4 · 10^5 N/m. Journal displacement values depending on time and the load after described modifications are shown in Fig. 7 and 8. With the implementation of an additional stiffness-damping element, a visible impact of external components attached to a vibrating bush was noticed. The pictures of the test rig indicated that the wires were of a fairly large diameter, and their stiffness in comparison to the compliant foil set could not be ignored. The bearing was therefore tested under the conditions much different from a operating conditions which are typical for rotating machnies.

Fig. 8 provides direct assessment of the reliability of developed numerical model. A direct comparison of the characteristics shows that by tuning the model, very similar waveforms were obtained. Displacements obtained by computer calculations achieved higher values for the same load but the shape of the loops obtained was very similar in the whole range of the bearing operation.
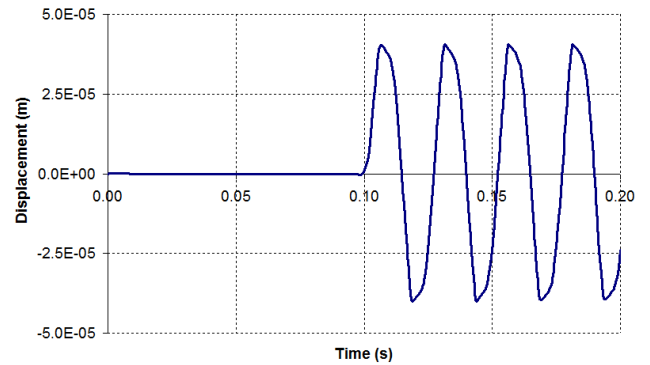

Fig. 7. Displacement of the shaft in the foil bearing at dynamic load (numerical model after validation)
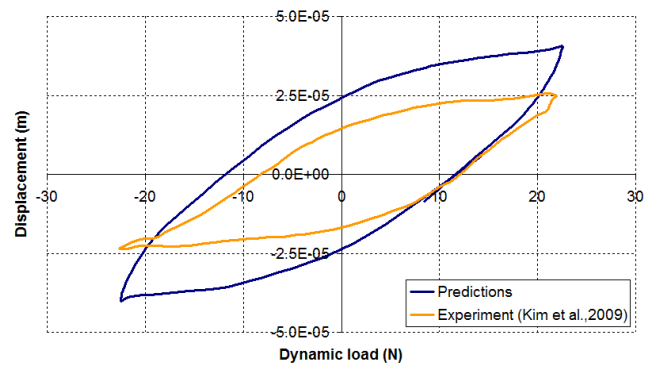

Fig. 8. Comparison of predicted and experimental displacement versus dynamic load for the foil bearing structure (predictions based on the numerical model after validation)

Due to the typical low productive precision of foil bearings and a small experimental repeatability, no further attempts were carried out in order to have even better fine-tune of the model. The discrepancies were probably caused by the way the radial clearance was included in the bearing, which does not exist in the actual design due to the initial clamp. Attempts to better tune the model can be taken after an own experimental research, in conditions more similar to those operating. As it turned out, the experimentally obtained performance was affected by several factors also not associated with the bearing, or rather with the test method used.

4. CONCLUSIONS

The article discusses a study to verify the foil bearing structure under dynamic loads. The following parts of this article expose the most important data for the numerical model, parameters for analysis and also the results of model verification. Modifications made during the tuning stage of the model allowed to obtain characteristics similar to the results of the experiment. Concluding

stage of the research on the numerical model of foil bearing the developed model successfully passed the verification and can be used for further research and analysis.

In the next stage of research, the model of the foil bearing structure will be integrated with the fluid-flow model. It should be noted that the developed structural model has a very high potential in the field of reproducing the properties of a flexible foil set, because in addition to complex, nonlinear geometry of thin foils it also takes into account the phenomenon of contact between all elements of the bearing. The concept of a complete model of bearing will be based on the consideration of the fluid-structure interactions. It will be the topic of the next publications.

REFERENCES

1. **Agrawal G.L.** (1997), Foil air/gas bearing technology - an overview, *International Gas Turbine & Aero Engine Congress & Exhibition*, Orlando (USA).
2. **DellaCorte C.** (1997), *A new foil air bearing test rig for use to 700 °C and 70,000 rpm,* NASA TM–107405.
3. **Howard S.A., San Andres L.** (2010), A new analysis tool assessment for rotordynamic modeling of gas foil bearings, *ASME Turbo Expo 2010: Power for Land, Sea and Air GT2010*, Glasgow, UK, (GT2010-22508).
4. **Kicinski J., Zywica G.** (2010), The numerical analysis of the steam microturbine rotor supported on foil bearing, *Advances in Vibration Engineering*, Vol. 11, No. 2, 113-119.
5. **Kicinski J., Zywica G., Rzadkowski R., Drewczynski M.** (2008), Numerical modeling of the structural layer of foil bearing, *Acta Mechanica et Automatica*, Vol. 2, No. 1, 45-50.
6. **Kim D., Park S.** (2009), Hydrostatic air foil bearings: analytical and experimental investigation, *Tribology International*, Vol. 42, 413–425.
7. **Kim T.H., Breedlove A.W., San Andres L.** (2009), Characterization of a foil bearing structure at increasing temperatures: static load and dynamic force performance, *Journal of Tribology*, Vol. 131.
8. **Kozanecki Z., Kicinski J., Zywica G.** (2009), Numerical model of the high speed rotors supported on variable geometry bearings, *IUTAM Symposium on Emerging Trends in Rotor Dynamics*, New Delhi, INDIA.
9. **Lee Y.B., Kim T.H., Kim C.H., Lee N.S., Choi D.H.** (2004), Unbalance response of a super-critical rotor supported by foil bearings - comparison with test results, *Tribology Transactions*, Vol. 47, No. 1, 54-60.
10. **Lee Y.B., Park D.J., Kim H.T., Sim K.** (2012), Development and performance measurement of oil-free turbocharger supported on gas foil bearings, *Journal of Engineering for Gas Turbines and Power*, Vol. 134, Issue 3, 54-60.
11. **Rubio D., San Andres L.** (2006), Bump-type foil bearing structural stiffness: experiments and predictions, *ASME Journal of Engineering for Gas Turbines and Power*, Vol. 128, 653-660.
12. **Salehi M., Heshmat H.** (2000), On the fluid flow and thermal analysis of a compliant surface foil bearing and seal, *Tribology Transactions*, Vol. 43, No. 2, 318 – 324.
13. **San Andres L., Kim T.H.** (2009), Analysis of gas foil bearings integrating FE top foil models, *Tribology International*, Vol. 42, 111–120.
14. **Zywica G.** (2011), The static performance analysis of the foil bearing structure, *Acta Mechanica et Automatica*, Vol. 5, No. 4, 119-122.